RANDOM LASER IN POLYMER OPTICAL FIBER AND OTHER DISORDER OPTICAL SYSTEMS

JIJUN HE

PhD

The Hong Kong Polytechnic University

2019

The Hong Kong Polytechnic University

Department of Electrical Engineering

Random Laser in Polymer Optical Fiber and Other Disorder Optical Systems

Jijun He

A thesis submitted in partial fulfilment of the requirements for the degree of Doctor of Philosophy

June 2019

CERTIFICATE OF ORIGINALITY

I hereby declare that this thesis is my own work and that, to the best of my knowledge and belief, it reproduces no material previously published or written, nor material that has been accepted for the award of any other degree or diploma, except where due acknowledgement has been made in the text.

____________________________________ (Signed)

Jijun He (Name of student)

Dedicated

To my Families and Friend

Abstract

Random lasers (RLs) are unconventional (mirror-less) lasers whose lasing feedbacks are synergistically achieved by multiple light scattering and optical gain amplification. Due to their easy fabrication, unique properties, and promising applications, much attention has been devoted to RLs over the past two decades. In this thesis, several different RLs are demonstrated in various optical systems. Their lasing dynamics are studied by means of experimental investigation and theoretical simulation. Utilizing these RLs, sensing and imaging applications are carried out, showing the potential of RLs in wide field of research and application.

In the first work, I demonstrated a one-dimensional random fiber laser based on the polymer optical fiber (POF). The core of the POF was doped with TiO_2 nanoparticles and Rh640 perchlorate dyes. A multimode and coherent random lasing was successfully obtained. The waveguide effect provided by the POF greatly increased the multi-scattering events for light propagation and resulted in laser cavity with much shorter length than the scattering mean free path. As an illustration of potential applications, a clear speckle-free imaging was demonstrated using the POFRL as the illumination source. Furthermore, a four-level Monte Carlo method-based numerical model is proposed to describe the lasing dynamic in the POFRL.

Second work presented a RL cytometer demonstrated in an optofluidic device filled with gain medium and human breast normal/cancerous cells. The multiple light scattering induced by the micro-scale human cells promoted the random lasing and influenced the lasing properties in terms of laser modes, spectral wavelengths, and lasing thresholds. A sensing strategy has been proposed based on analyzing the lasing properties. Based on this manner, the relationship between the lasing properties and both the whole-cell and the subcellular biophysical properties has been clarified. Furthermore, the malignant alterations of the cell suspensions are successfully detected.

In third work, I reported a hybrid two-photon RL device comprising double-resonant gold nanorods (GNRs) randomly embedded in an all-inorganic perovskite quantum dot (PQD) thin film. With increasing the GNR distribution density, the hybrid device exhibited an intriguing four-stage transition from amplified spontaneous emission (ASE), incoherent to coherent random lasing and back to ASE. By spectrally matching the longitudinal and transverse localized surface plasmon resonances of the GNRs with the two-photon absorption and emission wavelengths of the PQDs, the threshold power density monotonically decreased throughout the whole four-step evolution due to the double-plasmon-resonance-boosted population inversion in the PQDs. Using the hybrid laser device as the illumination source, the speckle-free two-photon imaging can be achieved.

In the fourth work, I reported the first experimental evidence of the glassy behavior in a RL with more complex energy level structures. This novel RL was demonstrated based on the electrospun polymer fibers with the assistant of Förster resonance energy resonance energy transfer (FRET). The electropun technology employed in the experiment promised high-volume production of RL devices with multiple types of the laser dyes, enabling the comprehensive investigation of lasing properties in multi-energy level RL system. Clear paramagnetic phase and spin-glass phase have been observed in the FRET-assisted RL under different pump energy. The replica symmetry breaking (RSB) phase transition was verified to be occurred at the laser threshold, which is robust among the RLs with different donor-acceptor ratio.

List of publications

Publications arising from the thesis

1. **Jijun He**, Wing-Kin Edward Chan, Xin Cheng, Ming-Leung Vincent Tse, Chao Lu, Ping-Kong Alexander Wai, Svetislav Savovic, Hwa-Yaw Tam, Experimental and theoretical investigation of the polymer optical fiber random laser with resonant feedback, Advanced Optical Materials, 2018, 6 (7), 1701187

2. **Jijun He**, Shuhuan Hu, Jifeng Ren, Xin Cheng, Zhijia Hu, Ning Wang, Huangui Zhang, Raymond H.W. Lam, Hwa-Yaw Tam, Biofluidic Random Laser Cytometer for Biophysical Phenotyping of Cell Suspensions, ACS sensors, 2019, 4(4), 832

3. Jiangying Xia#, **Jijun He#**, Kang Xie#, Xiaojuan Zhang, Lei Hu, Yaxin Li, Xianxian Chen, Jiajun Ma, Jianxiang Wen, Jingjing Chen, Junxi Zhang, Ilya D. Vatnik, Dmitry Churkin, Zhijia Hu, Replica Symmetry Breaking in FRET-assisted Random Laser Based on Electrospun Polymer Fiber, Annale der Physik, 2019, 1900066 (co-first author)

4. Siqi Li#, **Jijun He#**, Yunfeng Wang, Yubin Fan, Xin Hu, Qinghai Song, Hwa-Yaw Tam, Siu Fung Yu, Dangyuan Lei, Double-plasmon-resonance-reduced threshold of two-photon random lasing in all-inorganic perovskite quantum dots for speckle-free imaging, in preparation (co-first author)

Acknowledgements

The three-years journey of my PhD study is going to reach its end by this thesis. It is long and full of challenges. Fortunately, I have always been surrounding by warm-hearted and intelligent people. Without their help and support, the works involved in this thesis cannot be done.

First and foremost, I would like to express my deepest gratitude to my supervisor, Professor Hwa-Yaw Tam, for providing me this valuable opportunity to study in his group and work on the topics I interested in. Under his patient guidance and continuous support, I learned how to do research and gained extensive knowledge of optics, greatly benefiting my further career. Apart from been an extraordinary supervisor, he is a true gentleman making me fell warm and pleasure to study in his group. I also want to thank Professor Chao Lu for his kind help and introducing me to Professor Tam. They are my role models in research and life.

I would also like to thank all the colleagues in the Photonic Research Centre at PolyU, who help me and work with me during my PhD studies. I will never forget the happy time we spent together. Thanks to my colleagues and collaborators from Department of Applied Physics, CityU, and HFUT. They contributed a lot to my PhD studies. It is a great joy to work with them.

Additionally, I would to thank Professor Kippenberg Tobias at École polytechnique fédérale de Lausanne (EPFL). I really enjoyed the visiting study in his group (k-lab). It is an amazing experience, which will benefit me for a lifetime. I will never forget the support I got from the group members in k-lab (especially, the Si_3N_4 team members), as well as other colleagues at EPFL.

I would also like to thank my thesis committee Professor Wei Jin and external examiners for their time, support and helpful comments. My thanks are also extended to the staffs of the General Office and the Research Office. Thank anyone who is reading this thesis.

Most importantly, thanks to my parents. Thank you for sharing with me the faith so I do not feel weak, supporting me so I do not feel isolated, encouraging me so I can chase my dream. Making you proud is my lifelong motivation to pursue achievement and glory.

Table of contents

Chapter 1 Introduction

1.1 Background

1.1.1 Disordered optics

In the photonic theory, the order and periodicity of material structures in space domain are normally the two of the most important features, which are the prerequisites for many optical phenomena. By optimizing the regularity and eliminating the randomness of the optical systems, various applications can be realized, such as manipulating the atomic arrangement in the crystal lattice, optimizing the spatial arrangement of the photonic crystals and designing the distributed grating reflectors. In these applications, if the order and periodicity of material structures can be well modulated, the optical performances can be highly enhanced. Thus, the randomness and scattering have often been regarded as two unfavorable factors in optics. Many researchers tried to reduce or even avoid the present of randomness and scattering in ordered optical systems.

However, in the last decades, the disordered and complex optics became hot research topics. People spent lots of effort on the investigation of how to control the optical properties in the systems with strong random scatterings. The scattering and diffusion of light in random materials are the common physical phenomena. For example, the blue sky is caused by the light scattering from the suspended particles in the atmosphere. Recently, many interesting physical phenomena have been observed in disordered structure with the diffusion of light. In the case of elastic scattering, the information of light keeps the same during the diffusion. Based on the reversibility of light path, the original information can be restored based on the scattered light. These features enable the disordered optics great potential in many applications. For example, it has been demonstrated that the imaging can be realized based on the scattering and transmission light passing through biological tissue, which makes a great progress on the biomedical imaging and benefits other related fields like optogenetics and phototherapy.[1]

1.1.2 Localization of light in disordered system

When the system randomness increases, localized effect will appear. Figure 1.1 shows the Anderson localization phenomenon observed in a disordered photonic crystal. In a photonic crystal without disordered structure, a propagation light beam inside this system will diffuse due to the coupling effect of the nearby waveguides, as shown in Figure 1.1a. However, when the system randomness increases, the diffusion of the light beam will be compressed (Figure 1.1b) and the light beam profile in the transverse plane exhibits localized effect. Figure 1.1c shows the intensity profile obtained from the transverse plane in the case of system without randomness. Due to the elastic scattering, the size of the light beam increases as the propagation distance increases and the light pattern is triangular symmetry. When the periodic structure of the system is broken, the symmetry of the light pattern disappears and the light tunnels form randomly among the systems (Figure 1.1d). In this condition, the light intensity pattern shows a Gaussian profile, which means the transport is diffusive. If the randomness of the system continuously increases. The output light pattern become smaller and the intensity profile exhibits exponentially decaying tails (Figure 1.1e). This indicates the end of the light propagation along the transverse direction. The light reaches the localized regime and its diffraction broadening is limited. This is so-called Anderson localization.[2]

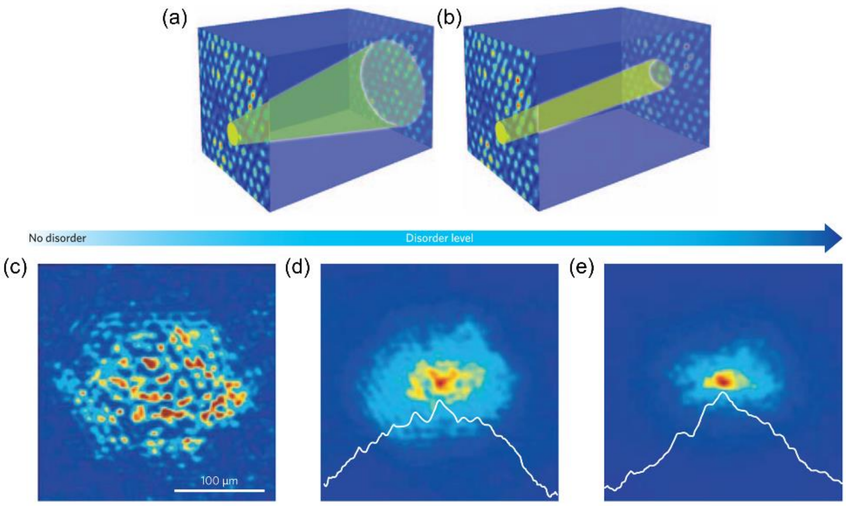

Figure 1.1 Anderson localization of light. As the disorder level increases, the light transport changes from ballistic regime to diffusive regime.[2]

1.1.3 Scattering of light in disordered system

During the propagation of light in disordered system, light scattering also occurs, which will make the light deviate from the original direction. The scattering strength is also related with the disorder level of the system. According to the inhomogeneous medium, the scattering can be classified as two types: (1) Scattering from particles, such as emulsion and colloid, (2) Scattering from molecules, arising from the local fluctuation of molecular density, such as critical opalescence. The light scattering also can be categorized based on the energy relationship: (1) Elastic scattering, including Rayleigh and Mie Scattering. (2) Inelastic scattering, including Raman and Brillouin scattering.

Rayleigh scattering is normally used to describe the scattering occurred in the systems with isotropy, non-conductive and sphere-shaped scattering particles. The incident light is far away the absorption of the scattering particles. The Rayleigh scattering strength is proportional to the $1/\lambda^4$, λ is the light wavelength. The condition of Rayleigh scattering is $2\pi r/\lambda \ll 1$, r is the radius of the scattering particle. When the size of the scattering particles is comparable with the light wavelength, the Mie scattering occurs. To analyze the Mie scattering, the charge distribution in the scattering particle need to be taken into account. In this case, the scattering particles are considered to be composed of a number of complex molecules, which form multipoles with collective oscillation under the incident electromagnetic field. The electromagnetic wave radiated from the multipoles are superimposed to form the light scattering. Raman scattering is the result of the interaction between the medium molecules and the incident light. Brillouin scattering is a phenomenon in which incident light waves interact with the acoustic phonons. This thesis mainly discusses the Rayleigh scattering provided by random nanoparticles.

1.1.4 Random laser

Another important application of the light scattering from disordered optical systems is to construct random lasers (RLs). Different from conventional lasers, RLs do not require a pair of paralleled mirrors to compose the resonant cavity. They only rely on the disordered scattering structure and gain medium to obtain lasing feedback and optical amplification to generate lasing. Figure 1.2 shows a schematic of a conventional laser and a RL. In a common RL system, the fluorescent molecules are gain media and the scattering particles provide multiple light scattering feedback. The RLs can be divided into two types based on the configurations: (1) the fluorescent materials themselves are the scattering structures, like quantum dots; (2) the fluorescent materials and the scattering structures are different, like scattering particles in dye solutions. Many RLs have been demonstrated in different disordered systems, such as randomly assembled semiconductor nanowires and dye powders. The lasing properties of RLs are different from the conventional lasers. A conventional laser with a well-defined cavity will produce a monochromatic, single-mode lasing, while a RL will produce lasing with multiple modes, multiple emission directions, and low spatial coherence. Although these random lasing features are normally considered to be unfavorable for laser application. Recently, it is found that RLs have great advantages in suppressing laser speckle and obtaining wide laser spectra.[3]

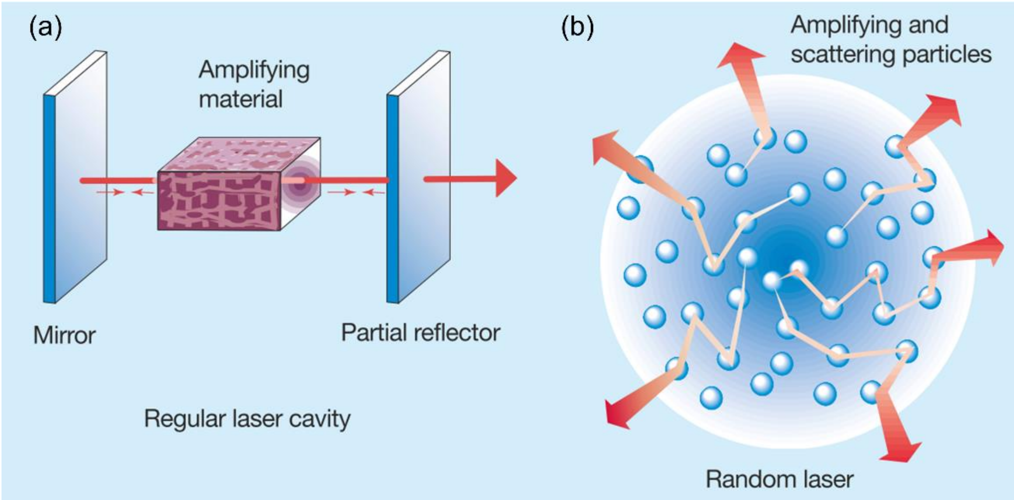

Figure 1.2 (a) Schematic of a traditional laser with a Fabry-Pérot cavity made of two mirrors with a gain medium between them. (b) Schematic of a random laser with gain medium doped with randomly distributed scattering particles.[4]

1.2 Research objective

The research objectives conducted in this thesis are to fabricate new types of RL systems, investigate their lasing properties, and find potential applications for RLs. More specifically, this thesis will focus on the following key research directions:

- Achieve RLs based on the disordered system with waveguide structure such as polymer optical fiber and microfluid. So that, the directional lasing can be achieved. Meanwhile, numerical model should be built to help the investigation of the random lasing properties modulated by the waveguide effect.
- Demonstrate applications based on the RLs. The RLs show low spatial coherence and can be used for the speckle free imaging. The imaging performance of the RLs

with different structure and configuration need to be investigated. Moreover, other RL applications such as sensing will be demonstrated.

- Carry out statistical analysis of the random lasing properties. Since the RLs exhibit intrinsic fluctuation of laser properties due to their randomness structures. The RLs systems are ideal research objects for the statistical investigation of the complex optics, which might share similar statistical properties with other disordered physical systems.

1.3 Thesis outline

This thesis is constructed by 7 chapters, presenting the research work during my PhD study. The arrangement details are shown as following.

Chapter 1 gives a brief introduction of disorder optics and RLs. The research objectives and the thesis structure are stated.

Chapter 2 provides a detailed review of the RLs containing the concepts, development, related work and literatures. The characteristics of the coherent and incoherent RLs are discussed. The theory studies with numerical models are presented, showing the connection between the experimental observation and theoretical analysis. The main methods of how to control the random lasing wavelength and direction are reviewed.

The last section of Chapter 2 will focuse on the applications of RLs including random number generation, speckle free imaging, and cancer diagnostic.

Chapter 3 presents a RL system based on polymer optical fiber. The fabrication process and experiment measurement are described. Its lasing properties and dynamics are investigated. A numerical model is built to explain the experimental observations. The imaging applications are carried out based on this one-dimensional RL. Its imaging performance is compared with a commercial laser regarding to the speckle contract.

In Chapter 4, I demonstrated a RL cytometer based on microfluidics. The random lasing properties change a lot when different types of cells were introduced into the devices. By analyzing the lasing properties, the biophysical properties of the health and cancer cells will be revealed in the cellular and sub-cellular level. As a result, the species of the cells can be successfully distinguished.

Chapter 5 presents a hybrid two-photon RL device comprising double-resonant gold nanorods (GNRs) randomly embedded in an all-inorganic perovskite quantum dot (PQD) thin film. The double-plasmon-enhancement strategy for reducing the random lasing threshold is proposed by spectrally matching the longitudinal and transverse localized surface plasmon resonances of the GNRs with the two-photon absorption and emission wavelengths of the PQDs. Using this PQD-plasmon hybrid laser device as the illumination source, the speckle-free two-photon imaging has been achieved. The imaging properties of these RLs with different GNRs are investigated.

Chapter 6 reports a novel RL based on the electrospun polymer fibers with the assistant of Förster resonance energy transfer (FRET). By statistical analysis the random lasing properties, clear paramagnetic phase and spin-glass phase have been observed in this FRET-assisted RL under different pump energy. The replica symmetry breaking (RSB) phase transition is verified to be occurred at the laser threshold, which is robust among the RLs with different donor-acceptor ratio.

Chapter 7 concluded the research work in this thesis. Several potential study topics are given, which can be done in the future.

Chapter 2 Background Review

2.1 Introduction

The feedback mechanism of the RLs is based on multiple scattering of the disordered medium and the gain is provided by the doped fluorescent materials. In conventional lasers, the light scattering occurred inside the laser cavities will prevent the formation of lasing oscillation. Thus, the light scattering is normally considered to be detrimental to lasers. However, in the gain system with strong disorder, the light scattering plays a positive role. First, multiple light scatterings increase the optical path and lifetime of photons in the gain medium, which benefit stimulated emission and increase gain. Second, the light loops formed by the light scattering provide coherent feedback for lasing oscillations. In the past decades, lasing generation in disordered systems has become hot research topics attracting the attention from both theoretical and experimental researchers. In RL systems, there are two different feedback mechanisms: one is energy density or energy feedback; the other is field or amplitude feedback. The former feedback is called incoherent or non-resonant feedback, and the latter feedback is called coherent or resonant feedback. Based on the feedback mechanism, RLs can be divided into two types: (1) incoherent RL based on energy density or energy feedback; (2) coherent RL based on field or amplitude feedback).

In 1966, Ambartsumyan and coworkers demonstrated a non-resonant feedback cavity by replacing one of the mirrors in the laser cavity with a scattering surface.[5] Light multi-scatterings occurred in this new type of cavity, changing the direction of the transport light. The light does not return to its original position after a round trip in the cavity. Thus, there is no spatial resonance of the electromagnetic field in such a cavity. The time of the light inside the cavity is not sensitive to the light frequency. In such system, only part of the energy or photons are coupled back into the gain medium, that is, the system has only feedback of energy or intensity. This non-resonant feedback can also be explained by analyzing the light modes. When a mirror of the laser cavity is replaced by a scattering plane, the emitted light leaking from the cavity becomes the main loss mechanism for all light modes. This results in many low Q resonances replacing the independent high Q resonance. These low Q resonances overlap each other to form a continuous spectrum and non-resonant feedback. The absence of resonant feedback indicates that the cavity spectrum tends to be a continuous spectrum, which means the spectrum does not exhibit an independently determined resonant frequency. As the pump increases, the emission spectrum gradually narrows toward the center of the gain spectrum. However, the narrowing process is much slower than the that of the conventional lasers. Because many modes in a non-resonant feedback laser cavity interact with the gain medium, the statistical characteristics of this lasing are completely different from the conventional lasers. Such laser without resonant feedback is spatially incoherent and its phase is also unstable. The only resonant component in this laser is the gain medium. The average frequency of the emission will not depend on the size of the laser cavity, but only on the center frequency of the gain spectrum. If the center frequency is sufficiently stable, the emission of this laser will exhibit stable emission at the center frequency.

Two years later, Letokhov theoretically predicted the properties of the RLs.[6] When mean free path of photon l_s (the average distance transmitted by two consecutive scattering events of the photon) is very small and less than the scale of the system but is greater than the wavelength of light, the photons are diffused in the system. In a homogeneous and linear gain system, the photon energy density $W(\vec{r},t)$ in the diffusion condition can be written as

$$\frac{\partial W(\vec{r},t)}{\partial t} = D\nabla^2 W(\vec{r},t) + \frac{\nu}{l_g} W(\vec{r},t) \tag{2.1}$$

where ν is the light speed in the scattering system, l_g is the gain length (the propagation distance of a light after being amplified e times.), and D is the diffusive factor, which can be express as

$$D = \frac{\nu l_t}{3} \tag{2.2}$$

where l_t is the transport mean free path (the propagation distance of a light before losing its original transport direction). The equation 2.1 can be further written as

$$\frac{\partial W(\vec{r},t)}{\partial t} = \sum_n a_n \Psi_n(\vec{r}) e^{-(DB_n^2 - \nu/l_g)t} \tag{2.3}$$

where $\Psi_n(\vec{r})$ and B_n are the eigenfunction and eigen value of the following equation

$$\nabla^2 \Psi_n(\vec{r}) + B_n^2 \Psi_n(\vec{r}) = 0 \tag{2.4}$$

When the extrapolation length z_e is beyond the physical boundary of the scattering medium, the boundary condition is Ψ_n=0. Normally, z_e is far less than the size of the scattering system and can be ignore. When the pump crosses the threshold, the soliton of equation 2.3 changes from exponential decay to exponential increase. In this changing point, we have

$$DB_1^2 - \frac{\nu}{l_g} = 0 \tag{2.5}$$

where B_1 is the smallest eigenvalue. If the scattering medium has a sphere profile with a diameter of L, we can get $B_1 = 2\pi n/L$. If the scattering medium has a cube profile with a length of L, we can get $B_1 = \sqrt{3}\pi/L$. Regardless of the shape of the scattering medium, the minimum eigenvalue B_1 is always in the order of 1/L. Putting $B_1 \approx 1/L$ back to equation 2.5, the critical volume V_{cr} can be deducted as

$$V_{cr} \approx L^3 \approx \left(\frac{l_t l_g}{3}\right)^{\frac{3}{2}} \tag{2.6}$$

When the volume of scattering medium V exceeds the critical volume V_{cr}, the photon energy density $W(\vec{r}, t)$ will exponentially increase based on the time t.

The above theory can be intuitively understood based on two parameters. One is the mean free path of photon generation L_{gen}, defined as the average distance of a propagation photon before generating second photon via the stimulated emission. This value can be estimated by l_g. The second parameter is the mean free path of a photon staying in the scattering medium $L_{pat} \sim \nu L^2/D$. In the conditions that $V \geq V_{cr}, L_{pat} \geq L_{gen}$, each photon can generate the second photon before escaping the scattering medium. This is so-called chain reaction, which can be simply understand as one photon becomes two photons and two photons become four photons. The total number of photons will rapidly increase. This process of photon generation is similar to the multiplication of neutrons in an atomic bomb.

2.1.1 Incoherent random laser

In 1994, Lawandy and co-workers observed a spectral narrowing phenomenon (laser-like) in the methanol solution containing rhodamine 640 perchlorate dye and TiO_2 scattering particles with diameter of 250 nm.[7] In this system, the laser dye is the gain medium pumped by a pulsed laser. TiO_2 scattering particles work as the scattering medium. Compared with the gain system containing only rhodamine laser dye, the emission spectrum of this dye-scattering particles system has a narrowing effect when the pump energy increases. By analyzing the relationship between the emission intensity and the pump energy, a threshold behavior can be observed in this random gain system.

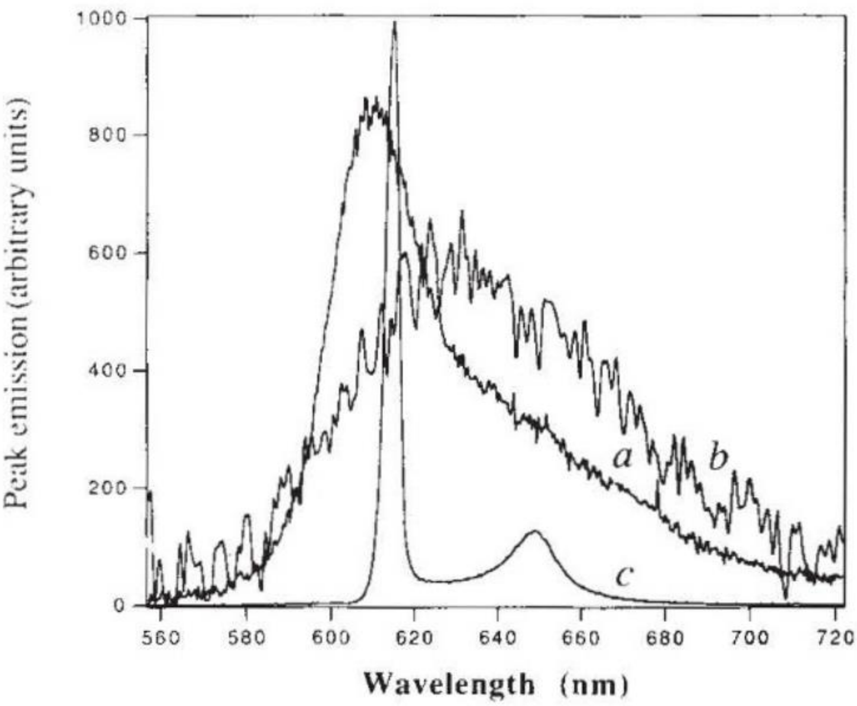

Figure 2.1 The emission spectra of (a) the pure laser dyes and (b-c) the mixture of laser dyes and TiO_2 scattering particles. The spectra of b and c have been scaled up by a factor of 10 and 1/20, respectivly.[7]

Figure 2.1a shows the emission spectrum of the pure laser dyes. Figure 2.1b and c show the emission spectra of the mixture of laser dyes and TiO_2 scattering particles under the pump of 2.2 μJ and 3mJ, respectively. A clear spectral narrowing effect can be observed in the scattering particle-doped scattering system. Figure 2.2 shows the full width at half maximum (FWHM) of the emission as a function of the pump power. When the pump power exceeds the threshold, the FWHM of the emission in the dye-particles system quickly decreases from 70 nm to 4 nm. The threshold behavior suggests the existence of feedback. Since the narrowed emission spectrum is relatively wide compared with lasing and there are no sharp emission peaks, this feedback is considered to be non-resonant feedback, and the threshold of this feedback is closely related to scattering strength of the system. In this scattering system, photons are easily escaped from the gain area. After multiple light scattering, the photons reenter the gain area and are amplified due to energy feedback. In general, the stronger the scattering, the greater the chance that the photon will return, which means that the energy feedback is stronger. The threshold of a RL system is determined by the photon loss rate and the photon generation rate. This is the first experimental demonstration of RLs. In the next year, Wiersma and co-workers proposed the conception of RL.[8] They further used diffusion theory to explain lasing dynamic of the incoherent RLs.[9]

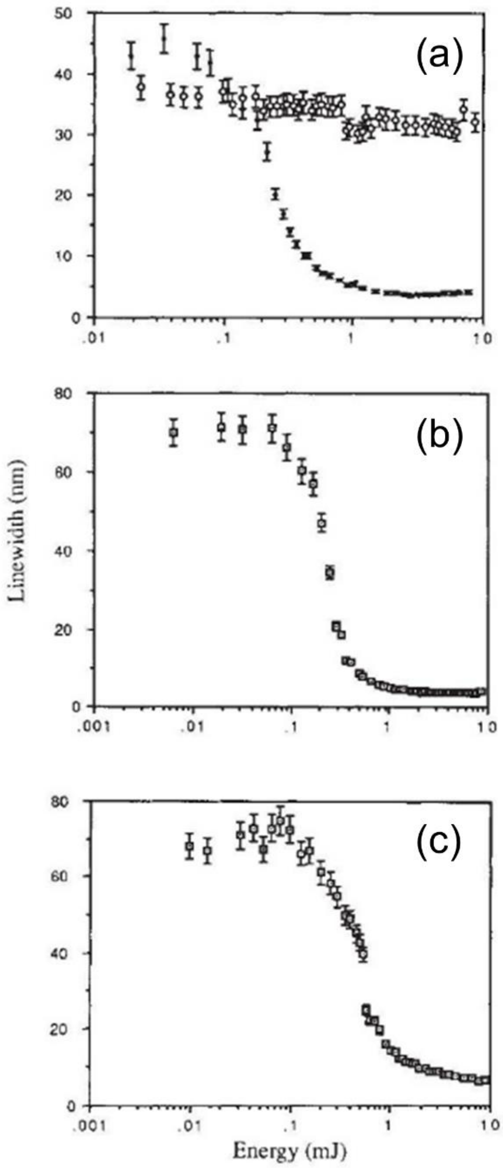

Figure 2.2 The linewidth of the emission as a function of pump power in the pure laser dyes system (circles in a) and the mixture of laser dyes and TiO_2 scattering particles with particle density of 5.7×10^9 (square in a), 2.8×10^{10} (b), and 1.4×10^{11} cm^{-3}(c).[7]

They built the theoretical model based on a pump-prob measurement of a powder slab. The gain medium was considered to be a four-energy-level system(3,2,1,0), in which from level 0 to level 3 is the pump progress, from level 2 to level 1 is the radiative transition, and from level 3 (or 1) to level 2 (or 0) is the fast relaxation. Thus, the population of level 3 and 1 is almost zero. The variation of the population in level 2 can be described by a rate equation. The dynamic of the whole system can be written as

$$\frac{\partial W_G(\vec{r},t)}{\partial t} = D\nabla^2 W_G(\vec{r},t) - \sigma_{abs}v[N_t - N_2(\vec{r},t)]W_G(\vec{r},t) + \frac{1}{l_G}I_G(\vec{r},t) \tag{2.7}$$

$$\frac{\partial W_R(\vec{r},t)}{\partial t} = D\nabla^2 W_R(\vec{r},t) + \sigma_{em}vN_2(\vec{r},t)W_R(\vec{r},t) + \frac{1}{l_R}I_R(\vec{r},t) \tag{2.8}$$

$$\frac{\partial W_A(\vec{r},t)}{\partial t} = D\nabla^2 W_A(\vec{r},t) + \sigma_{em}vN_2(\vec{r},t)W_A(\vec{r},t) + \frac{1}{\tau_e}N_2(\vec{r},t) \tag{2.9}$$

$$\frac{\partial N_2(\vec{r},t)}{\partial t} = \sigma_{abs}v[N_t - N_2(\vec{r},t)] - \sigma_{em}vN_2(\vec{r},t)[W_R(\vec{r},t) + W_A(\vec{r},t)] - \frac{1}{\tau_e}N_2(\vec{r},t) \tag{2.10}$$

where $W_G(\vec{r},t)$, $W_R(\vec{r},t)$, and $W_A(\vec{r},t)$ are the energy density of the pump light, the prob light, and the amplified spontaneous emission (ASE), $N_2(\vec{r},t)$ is the population density in energy level 2, N_t is the total population of the whole system, σ_{abs} and σ_{em} are the absorption and emission cross sections, l_G and l_R are the transport mean free path of the pump and prob light. I_G and I_R are the intensity of the pump and prob light, τ_e is the lifetime in energy level 2.

In a slab geometry, the critical volume can be simplified as the critical thickness, which can be described as

$$L_{cr} = \pi\sqrt{\frac{l_t l_g}{3}} = \pi l_{amp} \tag{2.11}$$

where l_{amp} is the mean free path of amplification, determined as the average distance between the start and end points of the gain path. In the slab structure, if the thickness of the slab is determined, the system has a critical amplification free path, that is, $l_{cr} =$

L/π. At the beginning of the pump, the mean free path l_{amp} was reduced due to the increased excitation level. Once l_{amp} reaches L_{cr}, the gain of the system will exceed the loss at the boundary of the system, resulting in instability of the system and increasement of ASE energy density. The increased ASE further excites the system and increase l_{amp}. This process will continue as long as the ASE is enhanced. The time scale for the formation of ASE is l_g/ν. Inside this window, the time it takes for the ASE energy density to diffuse out of the medium is L^2/D. In this system, there are two mutual factors that cause the output ASE energy flow to instantaneously oscillate. First, since the de-excitation needs to be established for a certain period of time, the excitation will be an overshoot. Second, once large-scale ASE established, its energy densities will slowly wear out due to the multiple scattering, which will result in an undershoot of the ASE energy density below the threshold. The oscillations are damped because the increase of l_{amp} during the de-excitation is opposed by re-excitation owing to the presence of pump light. As a result, the system can reach the equilibrium situation $l_{amp} = l_{cr} = L/\pi$ after a few oscillations.

2.1.2 Coherent random laser

In 1998, Cao and co-workers demonstrated a novel RL in a polycrystalline film containing ZnO powders (Figure 2.3).[10,11] When the pump power is below threshold, only a wide spontaneous emission spectrum can be observed. As the pump power exceeds a certain threshold, a narrow and discrete laser peak appears on the emission spectrum. They also found the emission spectrum is anisotropic, which means the emission spectrum is different in different collection direction. After this, similar phenomena have been reported in π-conjugated polymer film, polymer doped with laser dyes, and crystal materials containing polymer and laser dyes.[12–14]

These lasing properties are different from the incoherent RL. These systems contain resonance feedbacks providing discrete spikes on the emission spectrum when the pump power is above the threshold. These spikes are similar to the longitudinal modes of a conventional laser. These systems are named as coherent RLs. In coherent RLs, the scattering mean free path l_s is relatively small, resulting in strongly scattering for the emission. In these strong scattering systems, many closed cavities are formed, which provide coherent feedback. Thus, lasing resonances are formed within these closed cavities. Each closed cavity corresponds to one of some discrete laser peaks in the emission spectrum.[15] Since the closed cavities are formed in different regions of the system, different laser peaks will appear under different pump condition. In the same way, the emission spectra observed at different angles are distinctive, corresponding to the lasing generated in different cavities. This lasing dynamic of coherent RLs can also be explained based on the analogue of Anderson localization mentioned in Chapter 1. The closed cavities will form interference for the propagation light and result in standing-wave patterns with high degree of light confinement. There spatial resonances enable the coherent feedback in strong scattering system and amplify the spontaneous emission to lase. Based on this conception of Anderson localization, coherent RLs have been demonstrated in photonic crystals and optical fiber.[16,17]

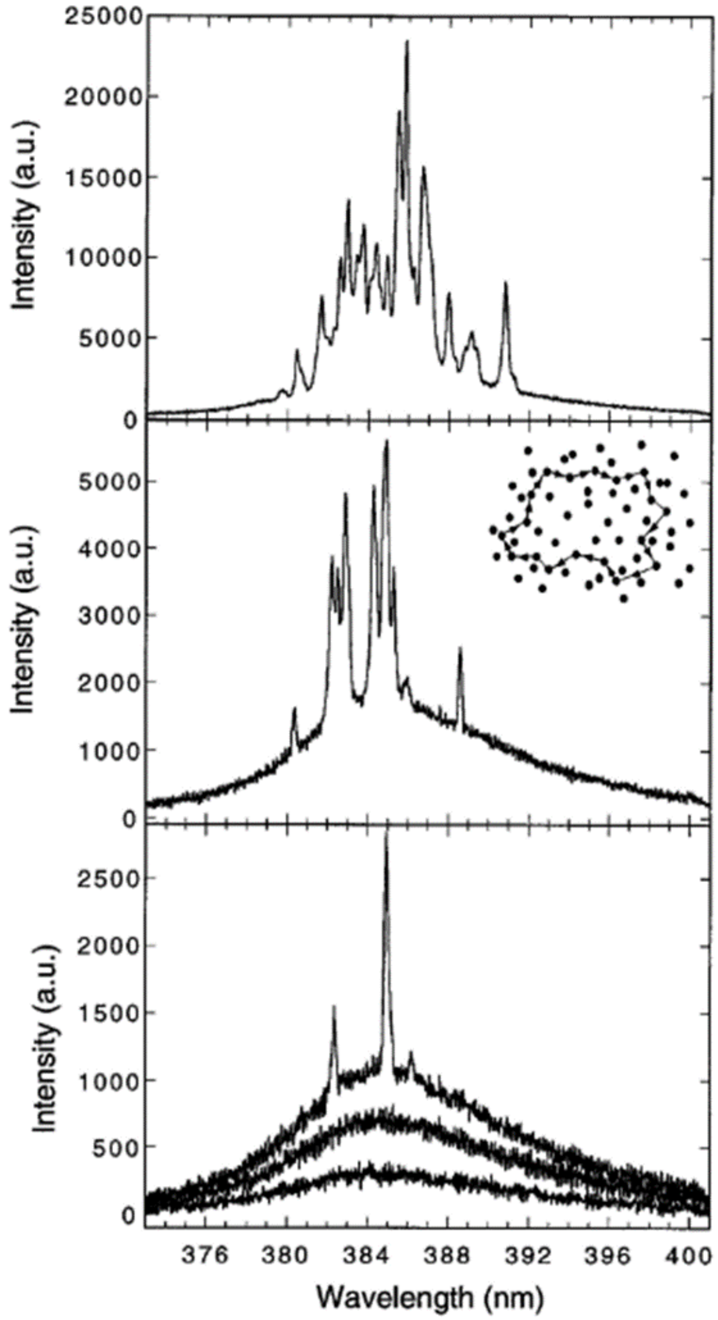

Figure 2.3 Emission spectra from ZnO powder. The insert shows the formation of a closed cavity based on the scattering provided by several particles.[11]

However, recently, it is also found that the coherent random lasing can be observed in the RL systems exhibiting weak scattering strength. Most of these RL systems are constructed based on waveguide structures, which providing light confinement to produce resonant modes.[18] Uppu and co-workers also showed that the 'luck photons' with extreme long propagation distance in the gain medium can be amplified to generate coherent lasing in dye-nanoparticles system with weak scattering strength.[19]

2.2 Theory and simulation of random laser

In the theoretical model of the incoherent RLs, only the feedback of the light intensity is considered. The feedbacks of the electromagnetic field and the phase have not been taken into account. Therefore, the incoherent RL model can only describe the narrowing effect of the emission spectra and the existence of the threshold but cannot explain the interference phenomenon of the coherent RL. Thus, new numerical models are needed to simulate the dynamic of coherent RL. The closed cavity theory qualitatively describes the effects of light interference and photon localization but does not quantitatively explain the properties of the closed cavities. Due to the multiple light scatterings, most of the energy is scattered out of the closed cavity, which causes the loss of such cavity to be large. As a result, the threshold of the coherent RLs should be very high, which is contrary to the experimental observation. This indicates the closed cavity model can only provide an intuitive explanation, more accurate theory models are desired. Thereafter, many researchers proposed a series of new models to quantitatively explain the experimental phenomena of coherent RLs, such as the random resonator theory, semi-classical theory based on FDTD method, chaotic laser with quantum theory, and Anderson localization, which will be detailly described in the following.

2.2.1 Random resonator

Apalkov *et al* proposed a random resonator theory to revise the above-mentioned closed cavity theory in 2002.[20] The random resonator theory is based on a two-dimensional ring structure, as shown in Figure 2.4. The effective in-plane dielectric constant in the core region is higher than the surrounding environment ε by an increasement of $\delta\varepsilon$. In this case, the random resonator can be regarded as a waveguide structure and support the whispering gallery mode. On a microscopic scale, these random resonators correspond to a certain group of scattering particles. The light trapping is provided by the coherent multiple light scattering of all the scattering particles inside the resonator. They demonstrated that the fluctuation of the dielectric constant induced by the finite particles size highly promotes the light confinement. Moreover, they provided quantitative prediction of lasing threshold upon the excitation size and disorder of the system, which matched the experimental observations reported by Cao's group.

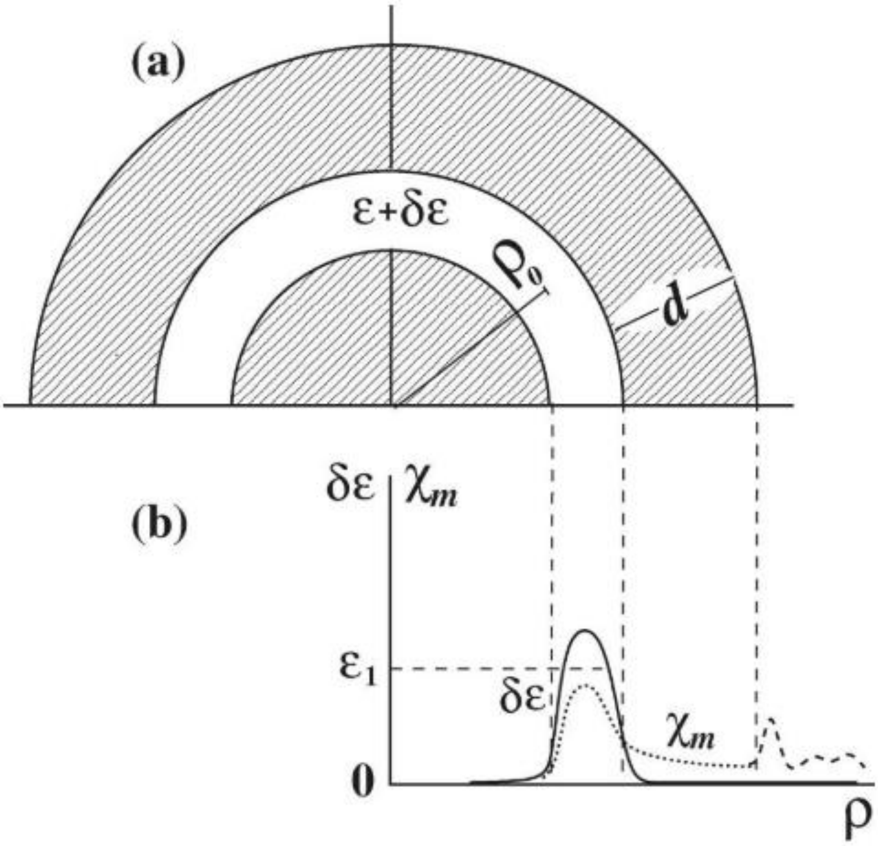

Figure 2.4 Diagram of the random resonator. (a) the two-dimensional resonator with waveguide structure. (b) The solid line represents the refractive index distribution of the system and the dotted line represents the field distribution. The dotted line outside the resonator is the evanescent field leakage.[20]

2.2.2 FDTD method

In 2000, Jiang and Soukoulis combined the semiclassical laser theories with Maxwell's equations to build a numerical model incorporating with the finite-difference time-domain (FDTD) method.[21] They coupled the Maxwell's equations with the rate equations of electronic population in a disordered system, and then used the FDTD method to solve the equations to obtain the spatial distribution and time evolution characteristics of the electromagnetic field in the disordered system, as well as the emission spectra via Fourier transform. The gain medium is a four-energy-level system (0,1,2,3). The electronic is excited from level 0 to reach level 3 and rapidly relax to level 2 with relax time of τ_{32}. The radiative transition between level 2 and level 1 will generate emission with frequency ω_a and lifetime τ_{21}. Finally, the electronic will relax to the ground level 0 with relax time of τ_{10}. The population $(N_3, N_2, N_1,)$ in the four levels can be expressed as

$$\frac{dN_3(\vec{r},t)}{dt} = P_r(t)N_0(\vec{r},t) - \frac{N_3(\vec{r},t)}{\tau_{32}} \tag{2.12}$$

$$\frac{dN_2(\vec{r},t)}{dt} = \frac{N_3(\vec{r},t)}{\tau_{32}} + \frac{\vec{E}(\vec{r},t)}{\hbar\omega_a} \cdot \frac{d\vec{P}(\vec{r},t)}{dt} - \frac{N_2(\vec{r},t)}{\tau_{21}} \tag{2.13}$$

$$\frac{dN_1(\vec{r},t)}{dt} = \frac{N_2(\vec{r},t)}{\tau_{32}} - \frac{\vec{E}(\vec{r},t)}{\hbar\omega_a} \cdot \frac{d\vec{P}(\vec{r},t)}{dt} - \frac{N_1(\vec{r},t)}{\tau_{10}} \tag{2.14}$$

$$\frac{dN_0(\vec{r},t)}{dt} = -P_r(t)N_0(\vec{r},t) + \frac{N_1(\vec{r},t)}{\tau_{10}} \tag{2.15}$$

where $P_r(t)$ indicates the external pump rate, $\vec{P}(\vec{r},t)$ is the polarization density, which can be further written as

$$\frac{d^2\vec{P}(\vec{r},t)}{d^2t} + \Delta\omega_a \frac{d\vec{P}(\vec{r},t)}{dt} + \omega_a^2\vec{P}(\vec{r},t) = \frac{\gamma_r}{\gamma_c} \cdot \frac{e^2}{m}[N_1(\vec{r},t) - N_2(\vec{r},t)]\vec{E}(\vec{r},t) \tag{2.16}$$

where $\Delta\omega_a$ are the linewidth of the emission, $\gamma_r = 1/\tau_{21}$, $\gamma_c = e^2\omega_a^2/6\pi\varepsilon_0 mc^3$, e and m are the charge and mass of the electron. $\vec{P}(\vec{r},t)$ can be introduced to Maxwell's equation

$$\Delta \times \vec{E}(\vec{r},t) = -\frac{\partial\vec{B}(\vec{r},t)}{\partial t} \tag{2.17}$$

$$\Delta \times \vec{H}(\vec{r},t) = \varepsilon(\vec{r})\frac{\partial\vec{E}(\vec{r},t)}{\partial t} + \frac{\partial\vec{P}(\vec{r},t)}{\partial t} \tag{2.18}$$

where $\vec{B}(\vec{r},t) = \mu\vec{H}(\vec{r},t)$. The disorder of the system is described by the fluctuation of the dielectric constant. The electromagnetic field distribution of the random medium can be obtained by solving the Maxwell's equations via FDTD method. Using Fourier transfer of the $\vec{E}(\vec{r},t)$, the emission spectrum can be calculated accordingly. Normally, in the numerical model, the random medium is surrounded by air and the whole model is covered with strongly absorbing layers which perfectly absorb the light escaping from the random medium. Based on this model, they calculated the lasing properties of a one-dimensional RL system. The interactions between localization effect and optical amplification were investigated. Moreover, this method can simulate emission intensity profiles and localized laser modes, explaining the multiple modes and anisotropic properties of the emission spectra. Based on this model, they also predicted various phenomena and properties of the RLs, such as, the mode competition, the laser saturations, and the average mode length. Moreover, they observed the energy exchange between localized modes in their numerical model. Soon after, these predictions were experimental confirmed by Ling and co-worker.[22] Some following works has successfully adopted this method to further analysis the lasing dynamic and properties in RL with different configurations.[23–26]

The advantage of this semi-classical theory is that the laser emission properties can be directly simulated in a random system with given structure and material information. Numerical simulations can reveal the laser spectrum, the dynamic response, and the spatial distribution of the laser mode. However, this method also has a drawback that it requires a large amount of computing power and running time when simulating a sample with large area and high resolution. Thus, this method is mainly used to simulate one and two dimensional RL systems.

2.2.3 Chaotic Laser

Chaotic cavity laser is a special kind of RLs, in which the dynamics of the cavity are chaotic due to the irregular shape of the cavity and the random position of the scattering particles in the cavity. A typical feature of chaotic laser is that there are one or few openings in the cavity, whose sizes are smaller than the light wavelength. As a result, photons can be trapped within the cavity. The statistical distribution characteristics of the threshold in such chaotic cavity laser has been firstly calculated by Beenakker and co-workers in 1998.[27] The average pumping rate at the laser threshold is much lower than that for compensating the cavity losses. The average number of the non-competing laser modes is proportional to the square root of the pumping rate. Moreover, they used the classical space burnout model is to interpret the mode competition and found that the average number of the excited modes is reduced. Later, the same group further calculate the statistical characteristics of the radiation below the laser threshold based on the relationship between the input and the output power. However, the saturation gain is ignored and the method they proposed only suitable for the linearly gain medium below threshold. In 2001, Hackenbroich and co-workers found the coupling of the overlapping resonance modes which caused by the external radiation field induced suppression and noise.[28] They used quantum theory to study these overlapping modes. By their method, the photon statistical characteristics of the single-mode hybrid laser can be analyzed and the gain nonlinear effect above the laser threshold was considered. Although many theoretical works on chaotic lasers has been reported, few experimental studies have been reported due to the difficulty in constructing a cavity with opening size smaller than the light wavelength.

2.2.4 Analytic approximation solution

By analytic approximation approach, the conditions of the coherent steady-state light oscillations in RLs can be simulated.[29–31] Similar with Fabry-Perot cavity laser, the requirement of the threshold in one dimensional RLs includes the both the steady-state round-trip gain condition and the round-trip phase shift condition.

2.2.5 Anderson localization

In 1958, Anderson discovered the localization effect in the random electronic system.[32] This localization of electrons is caused by the strong fluctuation of the system. Analogue to the optical system, the scattering and fluctuation in RLs are also strong, which will result in a similar localization phenomenon of light. In a strong scattering system, Anderson localization of light means the eigenmodes of the light wave equation in a finite size 2ξ is localized (ξ is localization length). They are the spatial localized solutions of the Maxwell's equations with exponential tails attenuated from the center. In a scattering system, the localization length is determined by the following factors: the refractive index difference between the scattering particles and the surrounding system, the size of the particles, the wavelength of the light, and the disorder of the system. According to the relationship between system size L and localization length ξ, the localization systems can be divided to two types: (1) $\xi > L$, in this system, the system dimension is not large enough to trap the light; (2) $\xi < L$, the light is localized because light cannot escape from the disordered system. The localized mode can reach the boundary through the exponential tail. The leakage rate of the localized mode is proportional of $\exp(-2r/\xi)$, where r is the distance from the boundary. Therefore, in a sufficiently large system, the leakage of the localized modes can be ignored. For the second localization system described above, the localized mode in a disordered system is similar with the mode of the conventional optical cavity, like Fabry-Perot cavity. The laser mode in the strong scattering system with gain is equivalent to the quasi-mode in the cold cavity in the absence of gain. Thus, by only simulate the quasi-mode in the cold cavity, the localized random lasing modes can be obtained. This theory successfully explained the properties of the threshold, spectrum and other characteristics of RLs.

2.3 Control of random laser

2.3.1 Direction control

In conventional laser, the well-defined cavity will define the direction of lasing emission. However, due to the random scattering of the disorder medium, the RLs exhibit multiple emission directions. When it comes to real applications, controllable emission direction is always desired. To this end, many methods have been proposed.

One simple way is demonstrating RLs in one dimensional structure. The waveguide will introduce an additional optical feedback to the scattering system and guide the lasing to emit from one direction. Figure 2.5a shows a RL based on a plasmonic nanostructure proposed by Zhai and co-workers.[33] The laser dyes were doped in a polymer film deposited on a glass substrate. On the surface of the glass, gold nanoparticles with irregular geometry are randomly assembled to providing strong scattering. Since the refractive index of the polymer is larger than that of the air. Part of the scattered light that reaching the interface between polymer and air will be reflected back to the polymer due to the total reflection effect. A waveguide structure is thus formed in between the air-polymer interface and plasmonic nanostructure. Based on this configuration, the directional random lasing can be achieved. In 2012, Hu *et al* demonstrated a coherent RL based on a liquid core optical fiber (Figure 2.5b). The scattering particles and gain medium were doped in the core region of the fiber. Using this fiber structure, the lasing will be guided and emit out from the facet of the fiber.

The divergence angle of the output beam is measured to be only around 7°. Such RL exhibits coherent characteristic, although the doped particles can only provide weakly scattering. They proved that the waveguide effect will highly enhance the scattering of the system and promote the coherent random lasing. Other fiber based RLs also exhibit the feature of directional random lasing, showing more potential in various application.[34]

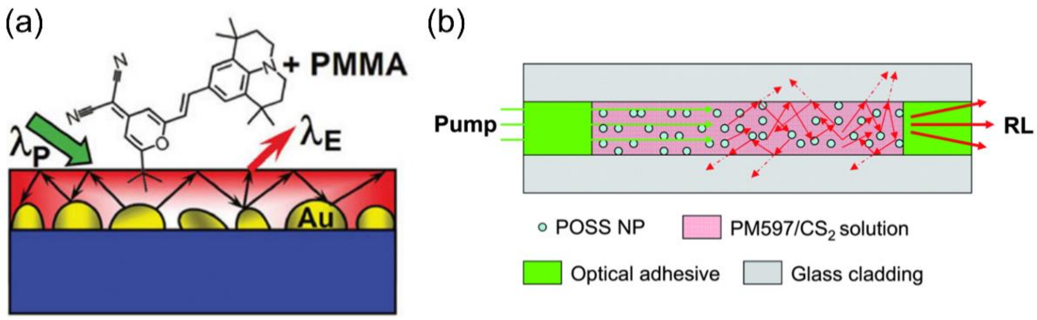

Figure 2.5 (a) RL based on the waveguide formed by plasmonic nanostructure and polymer films.[33] (b) RL based on liquid core optical fiber.[18]

Apart from changing the RL structure, the emission direction can be controlled via simply modulating the spatial pattern of pump beam. In the study done by Meng *et al*, a pump laser with a strip beam profile was used to illuminate the RL samples (Figure 2.6a).[35] Since only the laser dyes under pumping can provide gain for the emission. Such strip pump configuration will form a gain waveguide region in the polymer. The light emission scattered out from this region will be quickly dissipated. Therefore, only the light inside this waveguide can be amplified to lase. Lasing oscillation occurred preferentially along the waveguide-like region of the pump beam, giving rise to directional random lasing. Later, Rotter's group provided a universal method to control the emission directions and laser modes in a two-dimensional disorder system.[36] In this theoretical study, they used a spatial light modulator to shape the spatial distribution of the pump, as shown in Figure 2.6b. Based on the steady-state ab initio laser theory and optimization algorithm, one or several lasing modes with individual emission direction and wavelength can be selectively excited under the illumination of optimized pump configuration.

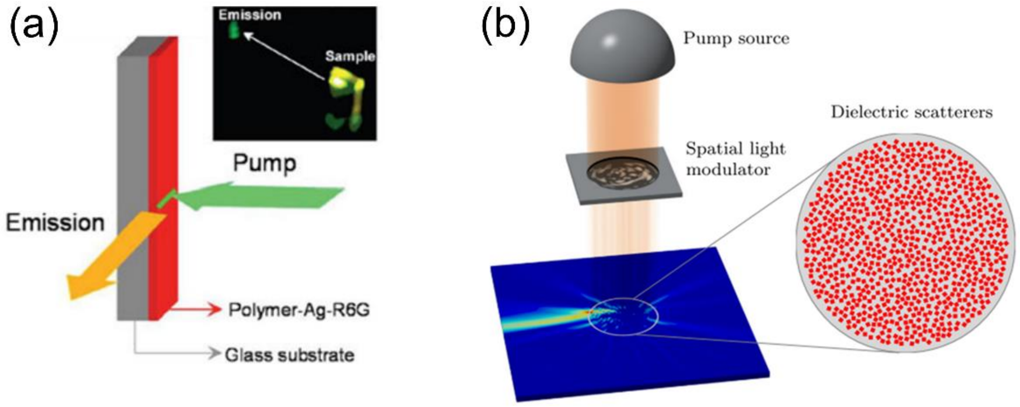

Figure 2.6 (a) RL under strip pumping condition.[35] (b) Numerical model of a two-dimensional RL under the pump with modulated intensity distribution.[36]

2.3.2 Wavelength control

Since RLs can be easily constructed based on random gain medium with size ranging from micrometer to centimeter, enabling the flexibility of the RLs. Thus, controlling the lasing wavelength properties became a hot topic in the research field of RLs. Generally, there are two research objectives for the wavelength controlling. One is to demonstrate RLs with multiple lasing wavelengths. The other is to achieve *in-situ* lasing wavelength tuning.

To achieve the wavelength control in board wavelength range, the most efficient way is to change the species of the gain materials. Meanwhile, different gain materials will have different absorption and emission spectral profile. In order to obtain optical feedback, the disordered medium should have a good scattering ability among the whole emission bands of the gain medium. For example, Ziegler and co-workers used gold nanostars to provide light scattering for the broadband RLs covering the range from green to near infrared (Figure 2.7a).[37] Because the gold nanostarts have anisotropy structures, which can support complex multi-plasmon resonances. The extinction spectrum of the ensemble of gold nanostars exhibits board extinction spectrum, providing efficient coherent feedback over an extensive range of wavelengths. Other novel scatterers with similar strong scattering among large wavelength range have also been fabricated for the RLs construction, opening an effective way to achieve multi-color random lasing.[38]

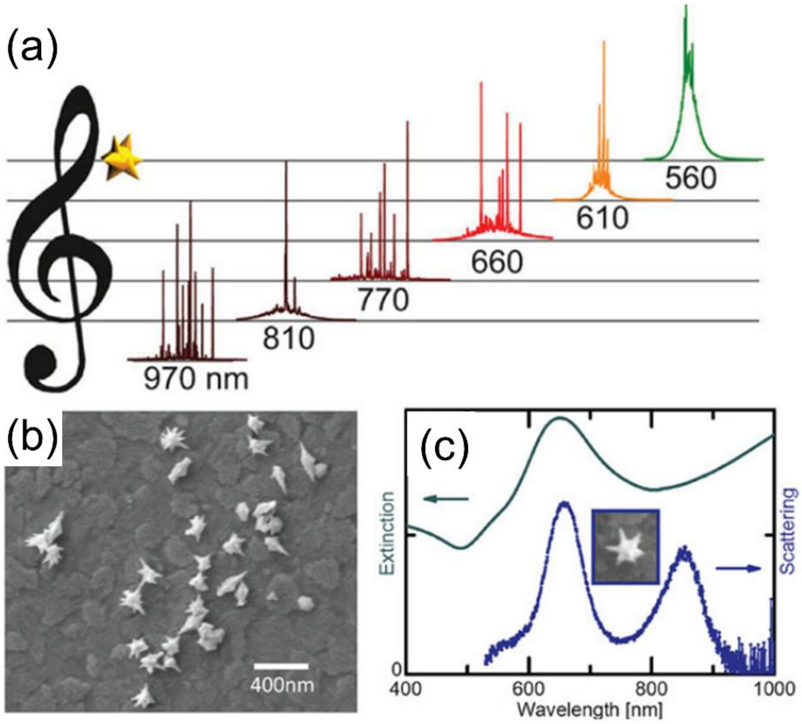

Figure 2.7 (a) Random lasing spectra of the mixture of different laser dyes and gold nanostars. (b) TEM image of gold nanostars. (c) Extinction spectrum (olive curve) of ensemble nanostars and scattering spectrum of a single nanostar.[37]

Instead of changing the gain medium, multi-color random lasing can be simultaneously achieved in RLs doped with several gain materials. Figure 2.8a shows a red-green-blue plasmonic RL based on a multi-polymer-layer structure. Three different gain materials are used to provide the red, green, and blue emission, respectively. The optical feedback is provided by the doped Ag nanoparticles. By optimizing the mass ratio of the gain materials, white random lasing can be achieved (Figure 2.8b).

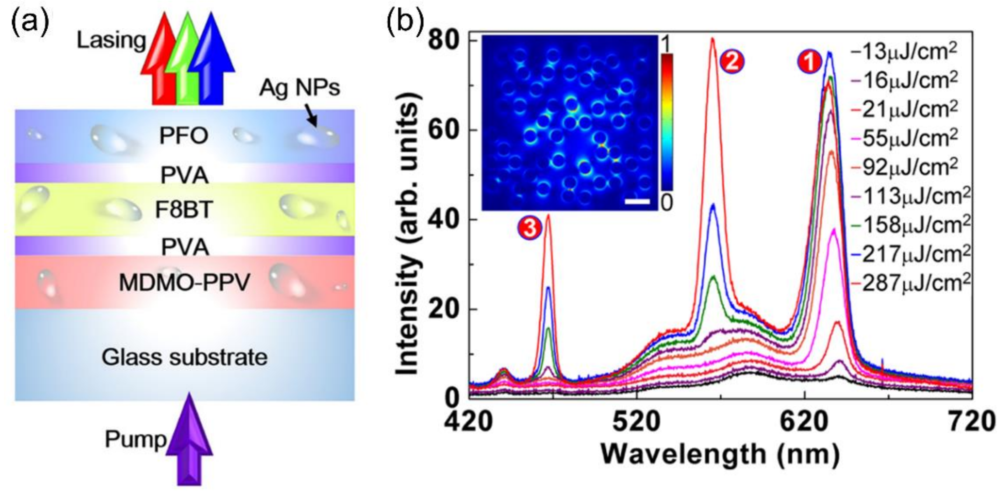

Figure 2.8 (a) Schematic of the RGB RL. (b) Emission spectra of the RGB RL under different pump power. The insert shows the calculated electric field enhancement caused by the Ag nanoparticles.[39]

If the gain materials are chosen to have a good spectral overlap between the absorption and emission spectra, Fòrster resonance energy transfer (FRET) can be realized. In FRET system, at least two gain materials are needed, one is donor, another is acceptor. Donor can be directly excited by the pump sources and then transfers its energy to nearby acceptor. In this manner, the long wavelength emission (from acceptor) can be obtained even under the pump far away from the absorption of the acceptor. In 2012, Luis and co-workers fabricated polymeric scattering particles doped with Rhodamine 6G (acceptor) and Nile Blue (donor) laser dyes, as shown in Figure 2.9a.[40] By controlling the acceptor-donor ratio, long wavelength, short wavelength, and multiple wavelength random lasing can be achieve, respectively (Figure 2.9b). This FRET-assisted RL provide a new strategy to overcome the inherent low visible absorption and poor photostability problems associated with commercial red-emitting laser dyes, avoiding the need to resort to specially engineered expensive dyes.

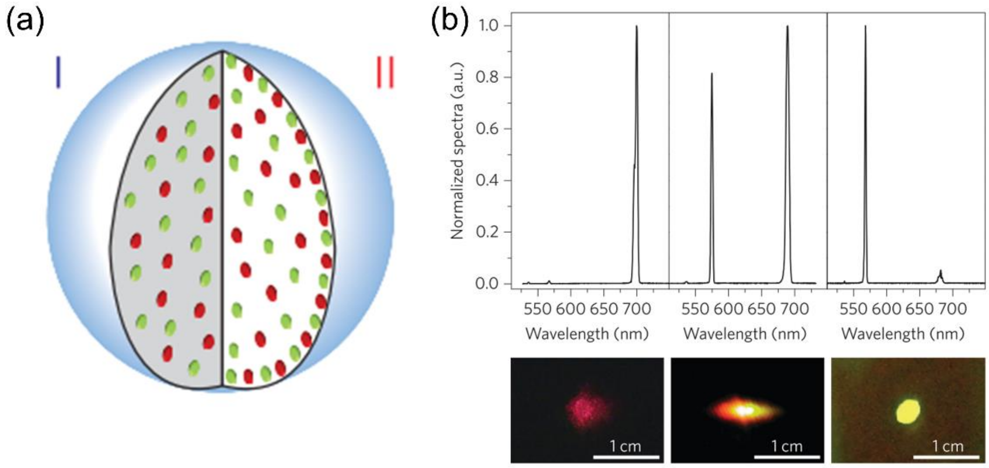

Figure 2.9 (a) Schematic of FRET-assisted RL. (b) Lasing spectra of the FRET-assisted RL with different doping ratio. Their corresponding images are listed in the bottom.[40]

In the above list studies, the wavelength control is realized via changing the gain or disorder medium during the RLs fabrication. However, it is a big challenge to control the wavelength of an already made RL. A simple manner is fabricating RLs which are sensitive with external environment. For example, Hu's group demonstrated a band-gap-tailored RL based on doping laser dyes in cholesteric liquid crystals (CLCs), as shown in Figure 2.10a.[41] The optical feedback is provided by CLCs whose structure can be modified via temperature control. An external near infrared light is used to illuminate and heat up the RLs. As a result, the CLCs structure changes as the illumination time increases, resulting in the modification of the disorder of the system.

Since the lasing properties (e.g. wavelength) is associated with the system disorder and structure. A large wavelength tuning up to 80 nm was achieved in this RL system (Figure 2.10b).

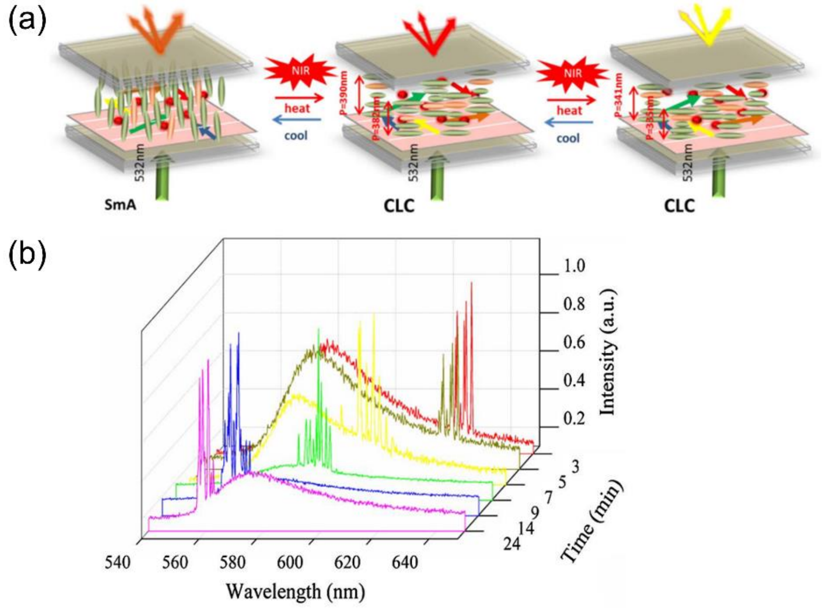

Figure 2.10 (a) Schematic of the band-gap-tailored RL. (b) Random lasing spectra at different NIR irradiation times.[41]

Similar with the method mentioned in the direction control section, the spatial pattern of the pump laser can be programmed to achieve the wavelength control. This strategy was theoretical proposed by Bachelard and co-workers in 2012.[42] Their numerical model is based on a one-dimensional RL. By partially pumping this RLs, the laser modes are selectively excited. Two years later, the same group experimental demonstrated this method in a one-dimensional microfluid random laser. Figure 2.11a shows the original lasing spectrum of the RL under uniform pump. By using spatial light modulator to program the pump intensity profile, certain laser mode was selectively excited and other modes were suppressed (Figure 2.11b). This method paves the way towards versatile tunable and controlled RLs as well as the taming of other laser sources

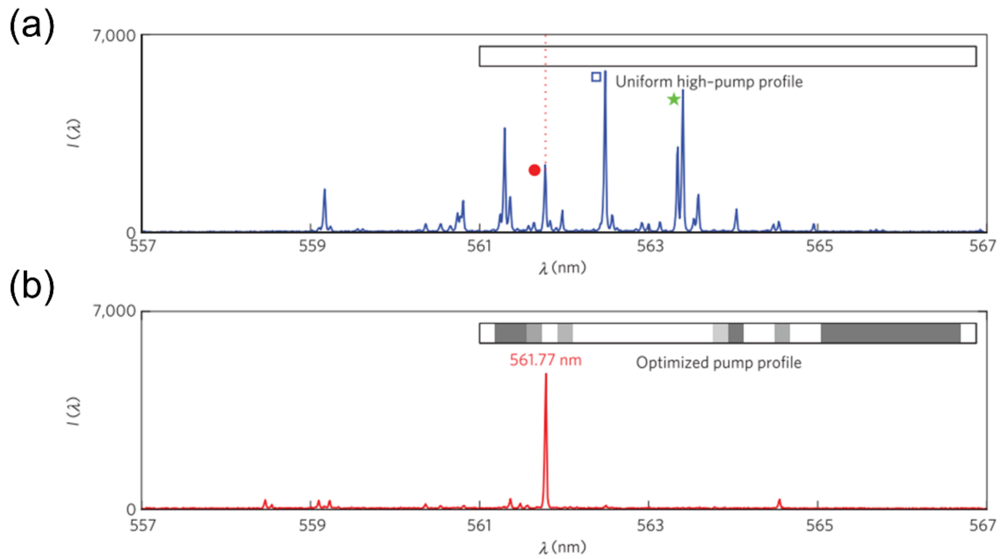

Figure 2.11 (a) Random lasing spectrum under uniform pump. (b) Random lasing spectrum under optimized pump profile showing single lasing mode.[43]

2.4 Applications of random lasers

Compared with conventional laser, RLs have many unique properties, such as low spatial coherent and high randomness, enabling the RLs great potential in some specific applications. Following, I will highlight some of most promising applications.

2.4.1 Random bit generation

Random numbers are important in many fields, such as, secure communication, scientific simulations, and cryptography. Thus, to find an effective algorithm to generate true random numbers is essentially important. Since RLs contains complex lasing dynamic due to the random scatterings provided by the disorder medium. The random lasing exhibits intrinsic randomness in terms of lasing modes and intensity. By measuring these unpredictable lasing properties, the random numbers can be generated. For example, Bao's group demonstrated Brillouin random fiber laser in a nun-uniform fiber based on the Brillouin scattering and enhanced Rayleigh scattering.[44] Ture random number generation with bit rate of 71 Mbps was achieved.

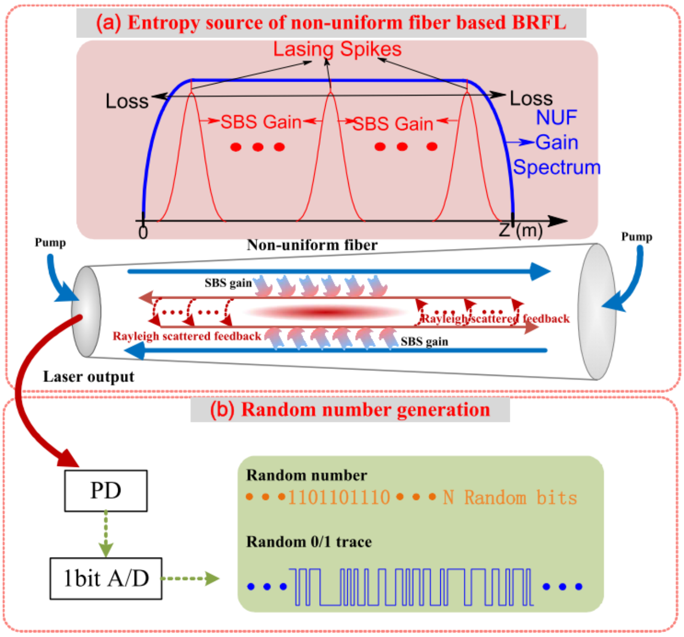

Figure 2.12 (a) Schematic of Brillouin random laser. (b) Schematic of the random number generation.[44]

2.4.2 Cancer diagnostic

Since the lasing properties of the RLs is highly sensitive to the scattering medium. The small change in the random medium will result in a remarkable variation in the lasing properties. Based on this effect, the cancer diagnostic can be realized based on measuring the lasing properties of the RLs. In 2004, Polson and co-workers demonstrated RLs in human colon healthy and cancerous tissues, as shown in Figure 2.13.[45] They found the lasing spectra obtained from the cancerous tissue showed more lasing spikes than that from the healthy tissue. After analyzed the laser cavities using power Fourier transform method, it was found that the cancerous tissue has more disordered microstructures which can form more laser cavities. Based on this feature, the cancerous tissue can be distinguished. Recently, similar strategy has been used to for the diagnostic of human breast tumor tissues.[46]

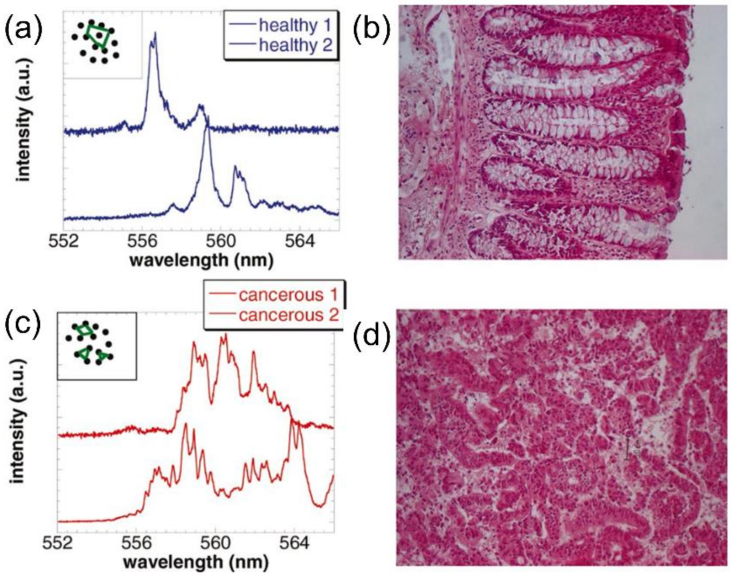

Figure 2.13 (a) Random lasing spectra from the healthy tissue infiltrated with laser dyes. (b) Optical image of healthy tissue. (c) Random lasing spectra from the cancerous tissue infiltrated with laser dyes. (d) Optical image of cancerous tissue.[45]

2.4.3 Speckle free imaging

In the modern imaging applications, lighting sources are indispensable components that directly determine the imaging quality and performance of the whole imaging system. Laser is such a commonly used lighting source with the features of high emission intensity and superior spatial coherence. These features not only benefit the imaging in lossy media but also reaveal more details behind the imaging (e.g. phase information in hologram). However, such excellent spatial coherence also induces the so-called speckle, i.e. an interference pattern of bright and dark fringes, which worsens the image formation and thus limits the use of lasers in full-field imaging. Different from the conventional lasers, the lasing dynamic of the RLs is based on the multiple light scattering in disordered gain media. Due to the random scattering feedback, the spatial modes of a RL are highly inhomogeneous with uncorrelated phases, leading to lowered spatial coherence. Compared with other low spatial-coherence light sources such as light emitting diodes, amplified spontaneous emission (ASE) sources, and fiber-based super-continuum light sources, RLs show higher spectral radiance due to the presence of lasing feedback. These features make RLs a promising class of light sources in the real-time full-field imaging applications. In 2012, Cao *et al* firstly used RLs for the speckle free imaging application, showing better imaging results with less speckle pattern and high brightness (Figure 2.14).[3] Thereafter, several studies have been successfully demonstrated using different RLs for the speckle free imaging.[47–50]

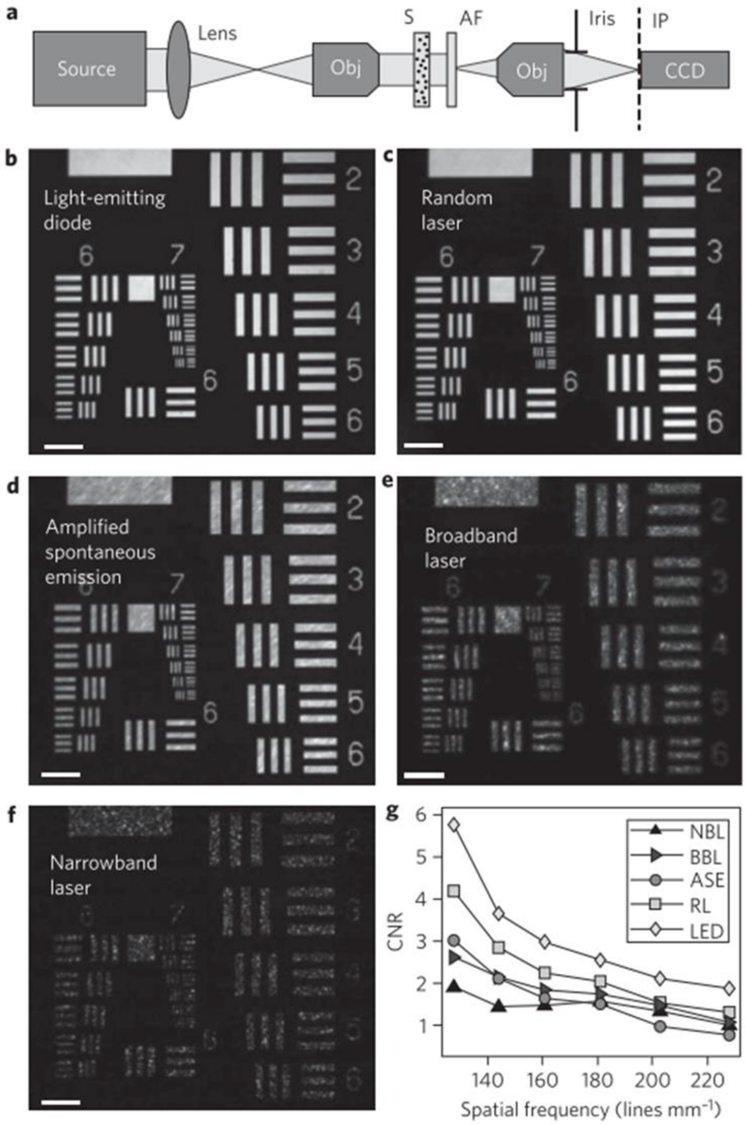

Figure 2.14 (a) Schematic of the imaging setup. Imaging results using (a) LED, (b) RL, (c) ASE, (d) Broadband laser, and (f) Narrowband laser. (g) Contrast-to-noise ratios under different illumination conditions.[3]

2.5 Summary

In summary, a detailed review of RLs including their basic conception, development, properties, and potential applications is presented in this chapter. The RLs are mirrorless novel type of laser with many unique properties such as compact structure, low spatial coherence and easy fabrication. Based on the lasing spectra characteristics, the RLs can be classified into two types: coherent and incoherent RLs. The incoherent RLs exhibit emission narrowing effect and threshold. Apart from these features, the coherent RLs show multiple spikes on the top of the emission spectra, resulting from strong localization or luck photons. Then, I summarized several theories and numerical methods for the investigation of lasing dynamics and properties in different types of RLs. Due the flexibility of the RLs, both emission wavelength and direction can be controlled, and corresponding methods are introduced. By the end of this chapter, several main applications of RLs are listed, showing the significance of RLs.

Chapter 3 Random Laser in Polymer Optical Fiber

3.1 Introduction

As introduced in Chapter 2, due to their easy fabrication, unique properties, and promising applications, much attention has been devoted to RLs over the past two decades.[3,9,11,45,51–55] Generally, RLs are constructed based on disordered systems containing gain medium, such as solutions and polymer films containing fluorescent dyes and scattering particles.[56,57] In recent years, a novel type of RL—one dimensional random fiber laser (RFL)—has been proposed and attracted great interest.[34] In 2007, Christiano et al. reported the first demonstration of RFL by inserting TiO_2 particles and rhodamine 6G dyes into the hollow core of a photonic crystal fiber, which opened the research field of RFLs.[58] Subsequently, both coherent and incoherent RFLs based on various fiber structures have been demonstrated.[18,59,60] These RFLs have several merits like low threshold, directional output and low-cost fabrication, indicating that they are superior to other conventional RLs in some applications.[18] According to the feedback mechanism, RFLs can be generally classified into two categories: (1) RFLs based on common single mode fibers with the feedback provided by Rayleigh scattering and Raman effect,[61–67] (2) RFLs based on specific fibers (e.g. liquid core optical fibers, polymer optical fibers, and erbium-doped fibers) with the feedback provided by doped particles or randomly distributed Bragg gratings.[18,68–73] For the first type of RFLs, their length are normally more than several kilometers, which limits their applications.[60]

Conversely, the size of the second type of RFLs is in the centimeter scale.[68] Moreover, the properties of the second type of RFLs (e.g. shape, size, lasing wavelength and laser threshold) could be tuned via controlling the fiber materials, scatterers, and optical gain medium.[69,70,74] As a result, the second type of RFLs can be regarded as ideal experimental systems for the investigation of random lasing with novel materials (like plasmonic materials), which have already been reported in several studies.[59,75,76] However, these studies mainly focus on experimental studies and corresponding theoretical models are still lacking to date. There is a need to find an effective numerical model to describe the lasing dynamic in the RFLs. Moreover, although RFLs have great potential in various applications, no practical application has been reported in the past studies.

In the chapter, I will present the polymer optical fiber RLs (POFRLs) demonstrated by doping TiO_2 scattering particles and Rh640 perchlorate dyes into the core of the POFs. The optical gain in the POFRL was provided by Rh640 perchlorate dyes which is a widely used organic luminescent dyes for many dye laser systems. The TiO_2 scattering particles worked as scatterers to provide multi-scattering events for light propagation and the resulting scattering strength is in the weakly scattering regime (scattering mean free path $l_s \gg$ emission wavelength λ). Multimode and coherent random lasing was observed in the POFRLs, which resulted from the waveguide configuration of the POFRLs. Moreover, it shows that the ROFRLs can be employed as an illumination source for full-field speckle-free optical imaging application because of their low spatial coherence. In addition, a two-dimensional numerical model based on a modified Monte Carlo method to simulate the lasing dynamic in the POFRLs is presented, whose results show a qualitative agreement with the experimental observations. To the best of our knowledge, this is the first work that demonstrates the specific imaging application of TiO_2 scattering particles doped POFRLs and provides an effective numerical model to describe the lasing dynamic in the POFRLs.

3.2 Fabrication of polymer optical fiber random laser

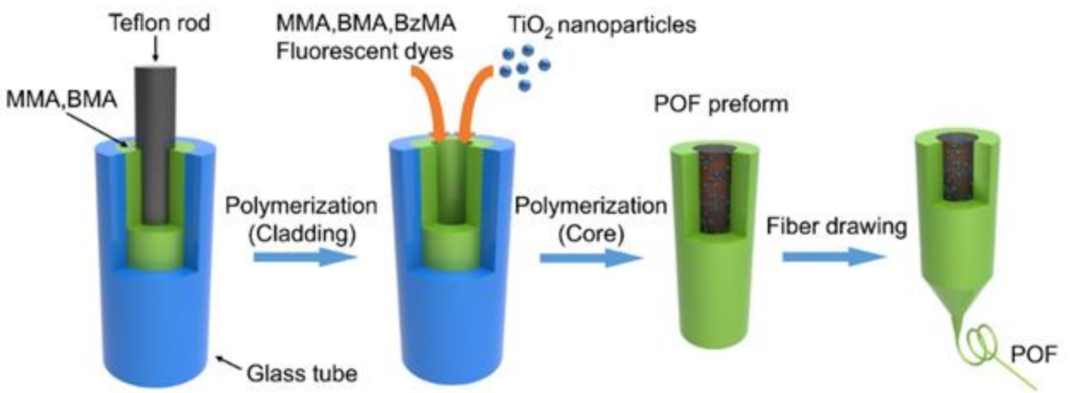

Figure 3.1 Schematic of POFRL fabrication process.

The POFRLs used in this work were fabricated using "Teflon technique", which contains two steps: cladding and core polymerization, as shown in Figure 3.1.[77,78] First, the methyl methacrylate (MMA) and butyl methacrylate (BMA) were filtered by a column of inhibitor remover and mixed together with molar ratio of 75:25. The monomeric mixture were poured into a glass tube mold and added with the 0.1 mol %

initiator Lauroyl peroxide (LPO) and 0.25 mol % chain transfer agent 1- decanethiol (DT). The diameter of the glass tube is 22 mm and a Teflon rod with 10 nm diameter was fixed along the central axis of the tube. Then, the glass tube was transferred into an oven for cladding polymerization. The temperature of the oven was given by a preprogrammed temperature profile, which included five stages and take about 96 hours for the fully cladding polymerization (as shown in Figure 3.2).

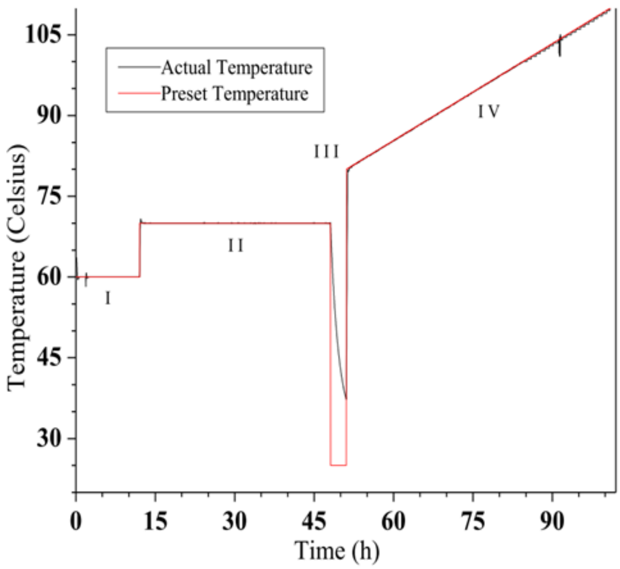

Figure 3.2 Actual and preset temperature profiles for the polymerization of the preform monomers.

Second, the hollow core of the as-fabricated cladding preform tube was filled with 800 ppm Rh640 perchlorate dyes, 400 ppm TiO_2 scattering particles, 0.1 mol % LPO, 0.25 mol % DT, and the monomeric mixture of MMA, BMA, and Benzyl methacrylate (BzMA) with molar ratio of 75:19:6. Then, the preform tube were mounted on a rotating system in the oven during the core polymerization process (Figure 3.3). The tubes were rotated at very slow speed during the polymerization process in the oven for four days. Since the tubes were rotated during the polymerization process, a uniform distribution of TiO_2 scattering particles in dye-doped preform could be obtained. The core polymerization went through the same heat process as mentioned above in the cladding polymerization. The POF preform was finally obtained and subsequently drawn into the POF at 235-260 degree centigrade using a home-made fiber drawing tower. The core and cladding diameters of the obtained POF were around 456 μm and 1004 μm, respectively. The corresponding refractive indexes of the core and cladding of the POF were calculated to be 1.5135 and 1.4904, respectively. The POF were cut into 5cm-long pieces and one fiber end-face for each piece was coated with gold mirror of 96% reflectance using a sputter deposition machine. From the concentration and the diameter of the doped TiO_2 scattering particles, the scattering mean free path l_s was determined to be around 600 μm, demonstrating that the POFRLs are in weakly scattering regime.

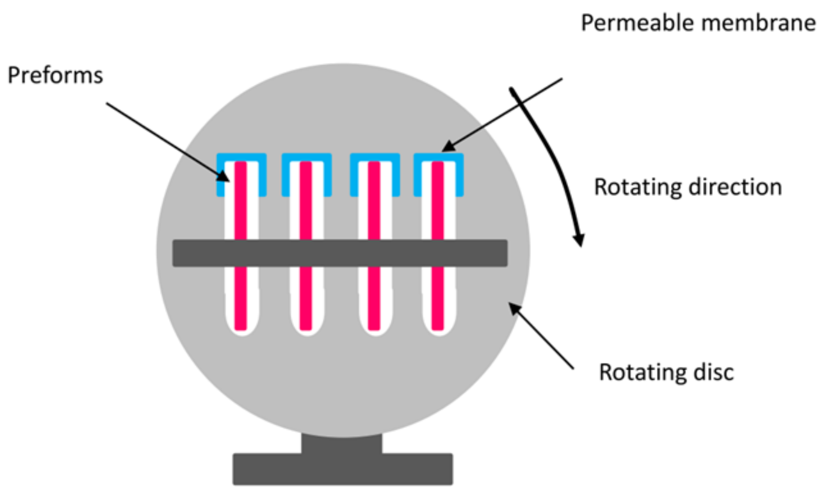

Figure 3.3 Rotating system to ensure more uniform distribution of the TiO_2 scattering particles in the dye-doped core materials during the long (4-5 days) preform

polymerization (curing) process. The whole system is put in an oven during the whole polymerization process.

3.3 Emission and random lasing measurements

3.3.1 Set-up

The emission properties of the POFRL were measured by an in-house setup, which consists of a Nd:YAG pulse laser (wavelength: 532 nm, pulse width: 6 ns), a HR4000 spectrometer, an optical power meter and several optical components, as shown in Figure 3.4. The laser beam was split into two parts via a 50:50 beam splitter (Thorlab, BS013). One laser beam was detected by a power meter (Coherent, LabMax-Top) to determine the laser power. Another laser beam was focalized with a cylindrical lens (Thorlab, LJ1629L1-A) to a 2.5 cm length and 1 mm width thin stripe to side-illuminate the POFRL. The emission and random lasing spectra of the POFRL were collected by a spectrometer (Ocean Optics, HR4000) equipped with a grating H6 (1200 line/mm) and a multimode fiber.

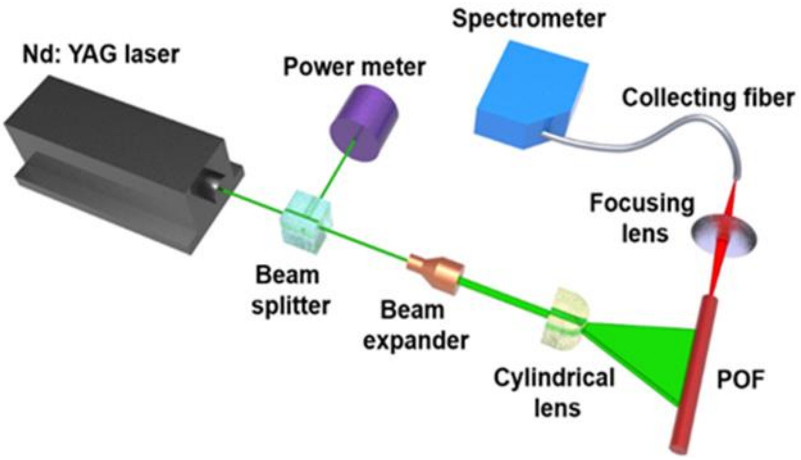

Figure 3.4 Schematic of the experiment setup for measuring the emission properties of the POFRL.

3.3.2 Spectral characteristics of the polymer optical fiber random laser

Figure 3.5a shows the evolution of emission spectra recorded for the POFRL excited at different pump powers. At low pump powers (sub-threshold), a broad spontaneous emission spectrum centered at 625 nm was observed and its full-width-half-maximum (FWHM) was measured to be approximately 37 nm. Several discrete narrow peaks (i.e. lasing modes) started to emerge as the pump power exceeded the laser threshold, which indicated that resonant feedback was generated in the POFRL. According to the previous studies, RLs with resonant (field or amplitude) feedback are categorized as coherent RLs.[79,80] The FWHM of the lasing mode narrowed down to 0.5 nm, which is two orders of magnitude narrower than the FWHM of the spontaneous emission peak. With increasing pump powers, the lasing modes disappeared and only one sharp peak (center wavelength: 625 nm, FWHM: 12 nm) was observed in the spectrum. The reason for the vanishing of the lasing modes could be due to the high pump power which excites all the lasing modes in the POFRL.[81–83] A very large number of the lasing modes with different wavelengths exist in the POFRL system (several thousands) and the spectral distance between each lasing mode is much smaller than the resolution of our spectrometer. Therefore, the spectrometer cannot resolve each lasing mode when they are all excited. Figure 3.5b shows the FWHM of the main lasing peak as a function of the pump power. The laser threshold was calculated to be around 9.2 mJ·cm^{-2}.

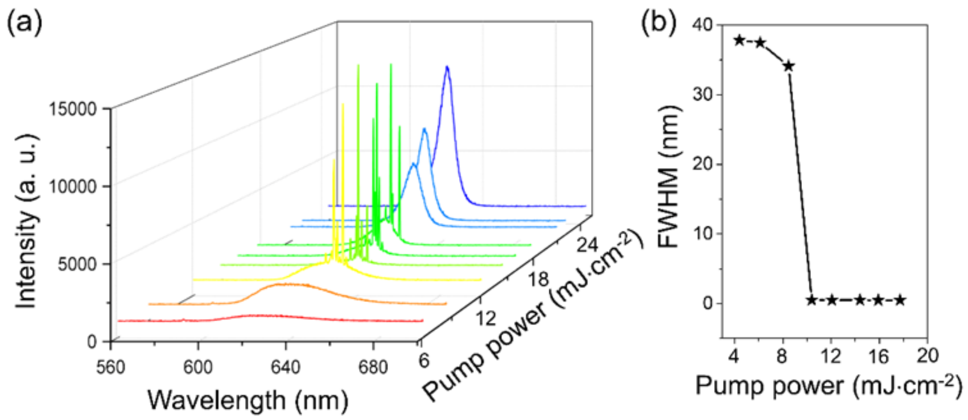

Figure 3.5 (a) Emission spectra of the POFRL at different pump powers. (b) FWHM as a function of pump power.

Figure 3.6a shows several lasing spectra collected from the POFRL at different pump powers (above laser threshold). It can be seen that the wavelength of each lasing mode was consistent, which indicates that there are several stable laser cavities in the POFRL. Figure 3.6b shows the schematic of the lasing mechanism of the POFRL, providing visualization of how the laser cavity is formed. Initially, the pump laser excites the fluorescent dyes to generate emission light. Due to the multi-scattering and reflection events provided by the doped TiO_2 scattering particles and waveguide configuration, the light path of the emission light significantly increases. The very large gain experienced by the emission light is the root cause for random lasing phenomena. The laser cavities are formed between several neighboring TiO_2 scattering particles together with the core-cladding interface. Since the structure of the POFRL and the positions of the doped TiO_2 scattering particles are immobile, the established laser cavities are stable, which results in random lasing at fixed wavelengths. However, the intensities of these lasing modes vary as the pump power changes. This can be attributed to the mode competition and the intrinsic statistical fluctuations of the RL.[81,84–86]

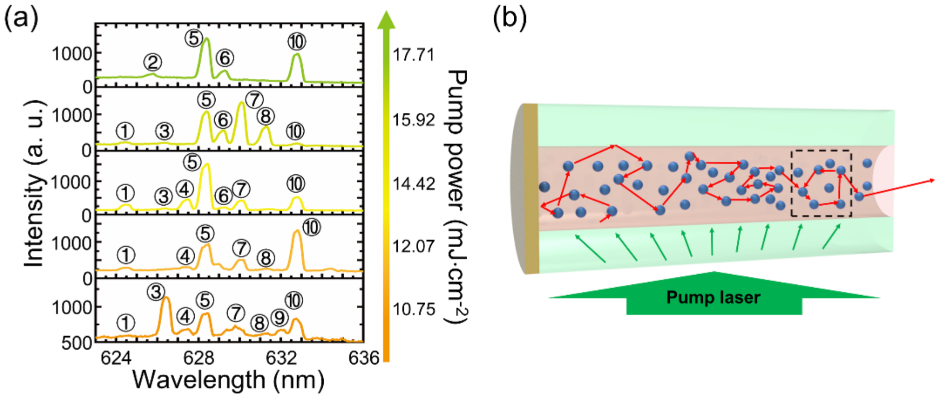

Figure 3.6 (a) Lasing spectra of the POFRL at pump powers above the laser threshold. The corresponding pump powers are listed on the right side of the spectra. The lasing modes are marked with numbers from 1 to 10. (b) Schematic of the lasing mechanism of the POFRL. Blue spheres represent doped TiO_2 scattering particles, red line indicates the light propagation path and the black dashed box points out a typical laser cavity.

3.3.3 Spectral characteristics of the dye soliton with TiO_2 scattering particles

In order to show the influence of waveguide effect provided by the POF on the lasing properties, a control sample was prepared by filling a quartz cuvette with the MMA solution containing TiO_2 scattering particles and Rh640 perchlorate dyes with the same concentration used in the POFRLs. The emission spectra obtained from the control sample at different pump powers are shown in Figure 3.7a. At low pump power, a broad spontaneous emission peak centered at 628 nm was observed with a FWHM of 41 nm. When the pump power increased, a narrowed lasing peak (centered at 618 nm) emerged on top of the broad emission spectrum. Notably, only one peak appeared in the emission spectra at any value of pump power, indicating incoherent lasing behavior in the cuvette RL system. Similar results have also been reported by Ignesti and co-researchers. They found that the cuvette RL systems exhibit incoherent random lasing when the scattering mean free path l_s is below 1000 μm (in this case, $l_s \approx 600$ μm) due to the numerous moderately amplified non-resonant lasing modes with strongly spatial coupling.[82,87] The different lasing behaviors between the POFRLs (coherent lasing) and the cuvette RLs (incoherent lasing) result from the waveguide effect provided by the POFRLs. First, the reflection of the core-cladding interface of the POF together with the scattering of the doped scattering particles will form the loop of scattering-reflection-scattering for light propagation in the core of the POFRL, leading to the increase of the scattering events and the generation of the resonant laser cavities.[18] Second, the waveguide confinement will lengthen the path length of the light inside the gain medium to experience large amplification, giving rise to the random lasing. Figure 3.7b plots the dependence of the emission intensities on the pump power. The threshold value is determined to be around 37.3 mJ·cm^{-2}, which is four times larger than that of the POFRL. This implies that the POFRL shows a low threshold feature.

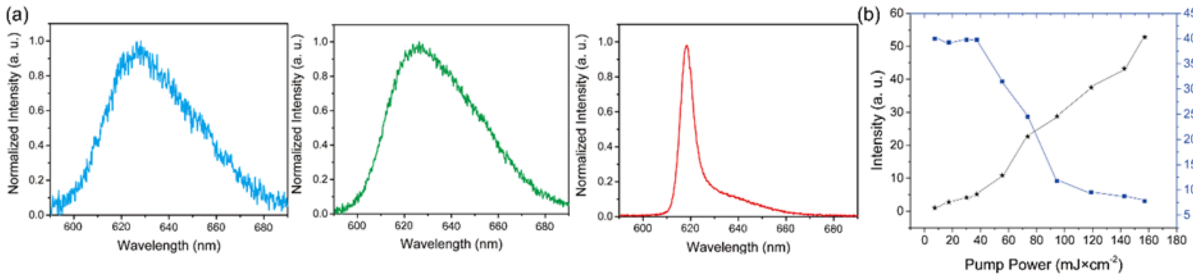

Figure 3.7 (a) Emission spectra of the control sample at different pump powers of (blue) 7.18, (green) 37.29, and (red) 157.46 mJ·cm^{-2}. (b) The FWHM and the peak intensity of the emission spectra as a function of pump power.

3.4 Cavity length analysis

As mentioned in the previous section, the waveguide configuration increases the multi-scattering events and enhances the formation of laser cavities. To obtain a better understanding of this phenomenon, power Fourier transform (PFT) analysis was performed to determine the length of the lasing resonant cavity of the POFRL.[88–90] The lasing spectrum of the POFRL at 17.71 mJ·cm^{-2} pump power and the corresponding PFT analysis result are shown in Figure 3.8. The peaks in Figure 3.8 indicate the Fourier components $p_m = mnL_c/\pi$, where m is the order of the Fourier harmonic, n is the refractive index of the core of the POF, and L_c is the cavity path length. For n=1.5135, m=1 and p_1=15.7 μm, L_c was calculated to be 32.6 μm.

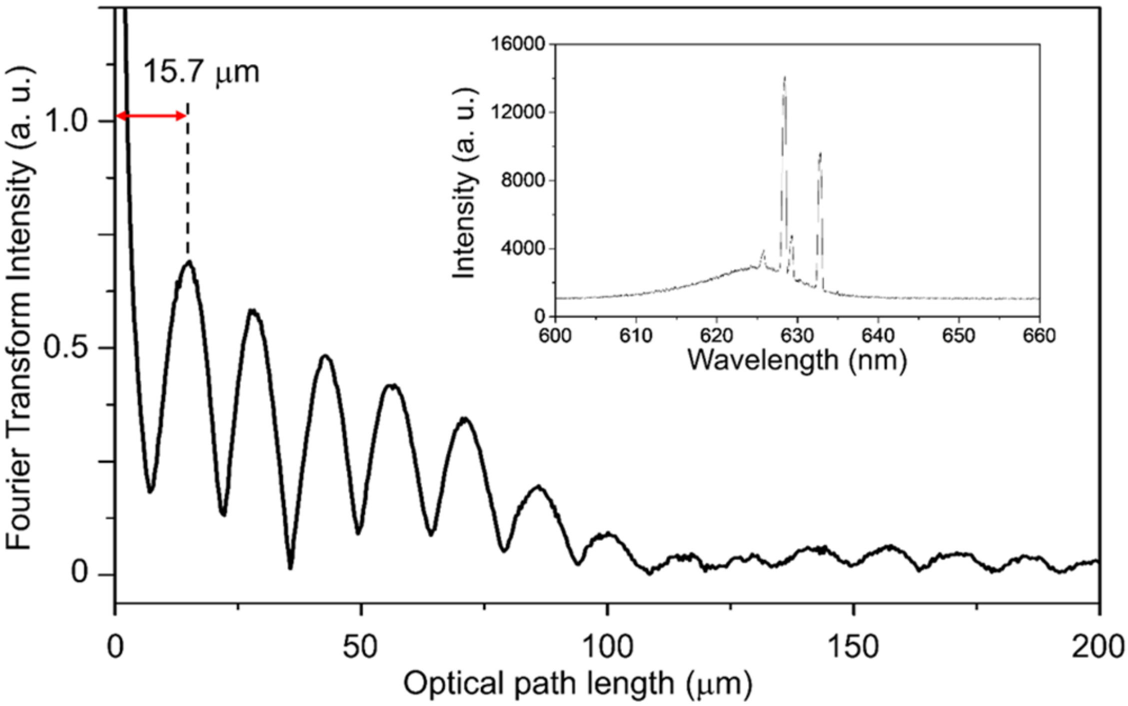

Figure 3.8 The power Fourier transform of the lasing spectra of the POFRL. The optical path length of the first order Fourier harmonic is determined to be 15.7 μm. The corresponding lasing spectra is shown in the insert figure.

The L_c is one order shorter than the scattering mean free path l_s (≈ 600 μm) provided by TiO_2 scattering particles. The PFT analysis for other emission spectra of the POFRL at different pump powers (as shown in Figure 3.9) is performed. It can be seen that the PFT results for the emission spectra at the pump powers of 12.07 and 14.42 mJ·cm^{-2} are almost the same as those shown in Figure 3.8. This means that the lasing generated from the same laser cavity produced these three emission spectra. However, the PFT results for the emission spectra at the pump powers of 10.75 and 15.92 mJ·cm^{-2} are quite different from the others, because new laser cavities are excited in these two cases.[88] Regardless of the pump power, the laser cavity length L_c is always much shorter than the scattering mean free path l_s of the TiO_2 scattering particles. Such low L_c value is due to the waveguide confinement effect provided by the POF, which highly increases the multi-scattering probability of the light and results in laser cavities with the cavity path length shorter than expected.[18,68,69]

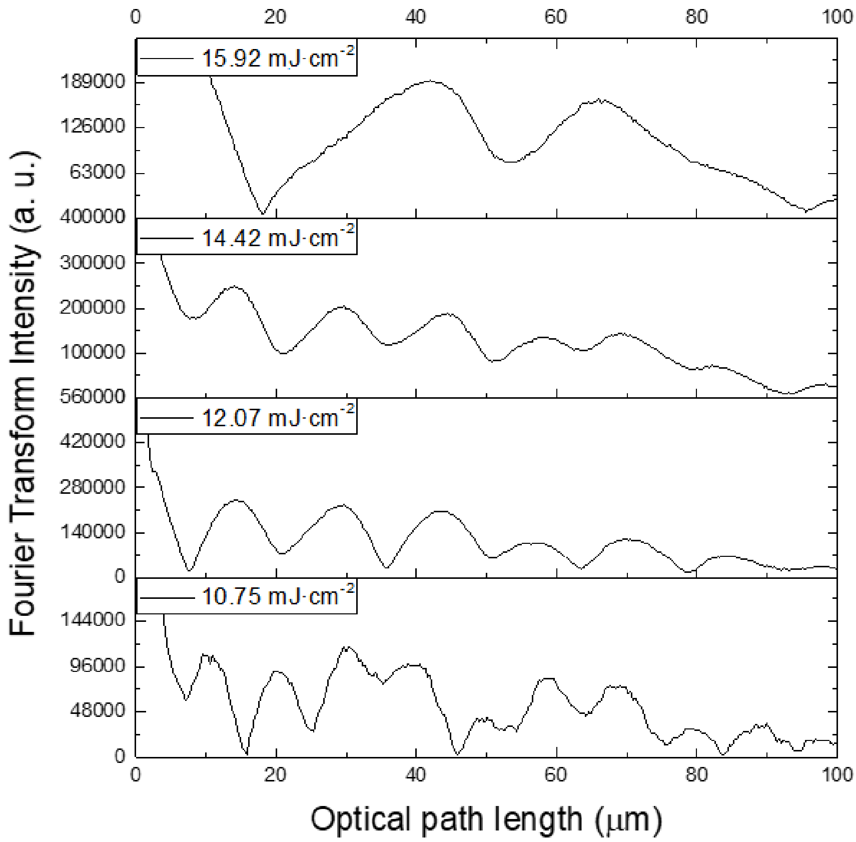

Figure 3.9 The power Fourier transform of the lasing spectra of the POFRL at different pump powers.

3.5 Speckle-free optical imaging

As mentioned in Chapter 2, one major application of RLs is speckle-free optical imaging due to their low spatial coherence.[3,83,91] Here, the spatial coherence of the POFRLs was measured and their potential in speckle-free imaging was tested. Figure 3.10a shows the experiment setup for optical imaging using the POFRL as illumination source. For spatial coherence measurements, the output of the POFRL was focused by a lens to illuminate and transmit through a frosted glass. The coarse surface of the frosted glass introduced random phase delays to the transmitted light, which would create speckled image using the light sources with a high degree of spatial coherence. The resultant image was collected by an objective lens (10×) and recorded by a camera, as shown in Figure 3.10b. To analyze the spatial coherence, a parameter called the speckle contrast C is defined as $\mathrm{C} = \frac{\sigma_I}{\langle I \rangle}$, where σ_I is the standard deviation of the image intensity and $\langle I \rangle$ is the average intensity of the image. A totally spatial coherent light has a speckle contrast of 1, whereas a light without spatial coherence has a speckle contrast of 0. Here, the measured speckle contrast was $\mathrm{C} = 0.07$, showing that the spatial coherence of the ROFRLs is very low. A control experiment realized using a 650 nm commercial laser as the illumination source (Figure 3.10c) gave a speckle contrast of $\mathrm{C} = 0.76$.

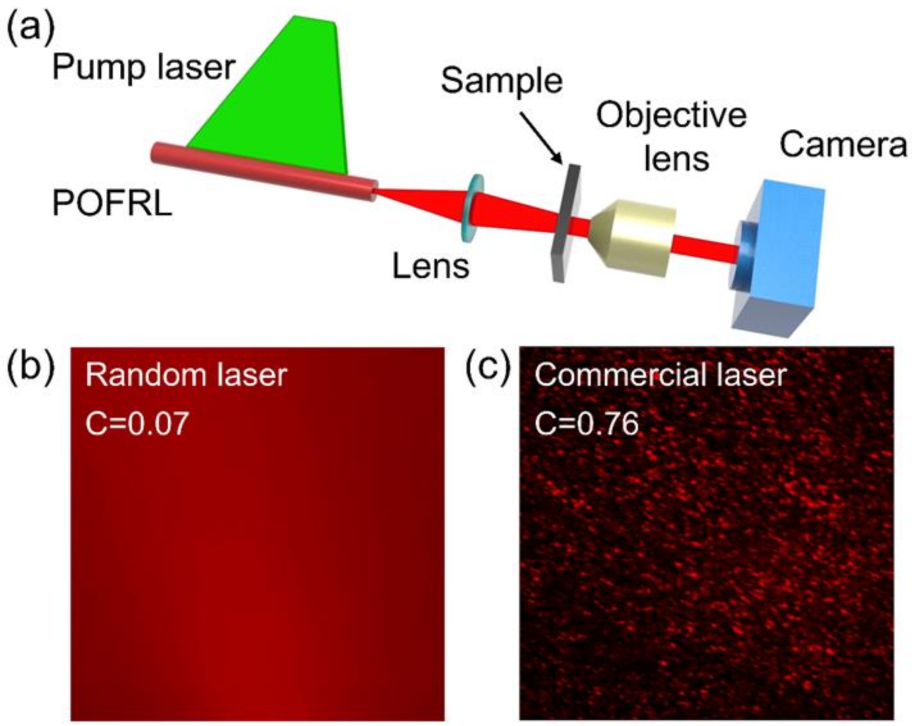

Figure 3.10 (a) Schematic of experimental set-up for speckle-free imaging with the POFRL as the illumination source. Optical images of the speckle pattern using (b) a POFRL and (c) a 650 nm commercial laser as the illumination source.

For the speckle-free imaging, a custom-made mask embedded with the university logo replaced the frosted glass to work as the imaging object. Under the illumination of the POFRLs, a clear speckle-free imaging was obtained, as shown in Figure 3.11a. For comparison, the imaging using a 650 nm laser to illuminate the mask was tested. Poor-quality image with speckle pattern was observed due to the high spatial coherence of the commercial laser, as shown in Figure 3.11b. This suggests that the POFRLs can serve as the illumination source for the speckle-free imaging application. The calculated speckle contrasts are shown in the top left corner of each images.

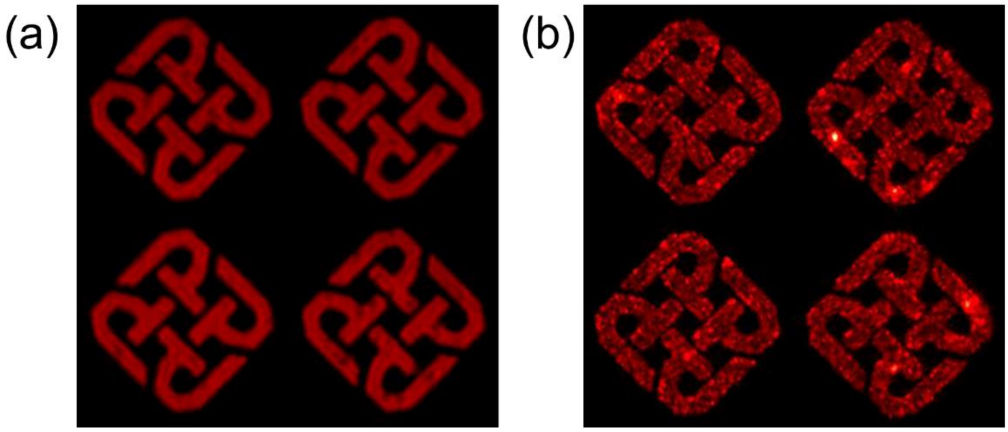

Figure 3.11 Optical images of the university logo mask under the illumination of (a) a POFRL and (b) a 650 nm commercial laser.

3.6 Simulation

3.6.1 Simulation model based on Monte Carlo method

Several theoretical models have been reported to describe the lasing dynamic in RL, as listed in Chapter 2, e.g., Anderson localization model,[92,93] the diffusion equation with gain,[9,94,95] and the Monte Carlo simulation.[19,87,96–98] Because the POFRL is in the weakly scattering regime, which means that the interference effects do not play a role in the lasing process of the POFRL. The Monte Carlo simulations treats light propagation as random walkers of photons inside a region with scattering and gain, and is suitable for modeling the lasing dynamic of the POFRL.

Although the POFRLs can be regarded as one-dimensional RL system from the macroscopic perspective in the experiment. The simulation model, considering the effect of the scattering particles and the waveguide structure, cannot be simply built based on one-dimensional structure. According to the axisymmetric waveguide structure of the POFRLs, a two-dimensional simulation model was proposed based on a rectangular region with orthogonal grids (Figure 3.12). The simulation regions are partitioned by the orthogonal grids into numerous small cells with same sizes.[87,99] The center of each cell is indicated by the vector index(x, y), with x, y integers in the range of $1 \leq x \leq L_x, 1 \leq y \leq L_y$. The total number of cells is $L_x \cdot L_y$. Two long sides of the rectangular region are set as reflective boundary representing the core-cladding interface of the POF. The other two sides are set as output boundary, where the output photons are collected. It should be noted that the orthogonal grids are set at a 45° angle to the boundaries. This construction allows the light walkers to propagate along the y axis instead of being trapped between two reflective boundaries, which is consistent with the waveguide effect in POFRLs. The simulation model is a four-level system based on an initialization step and a loop of three distinct steps as shown in Figure 3.12.

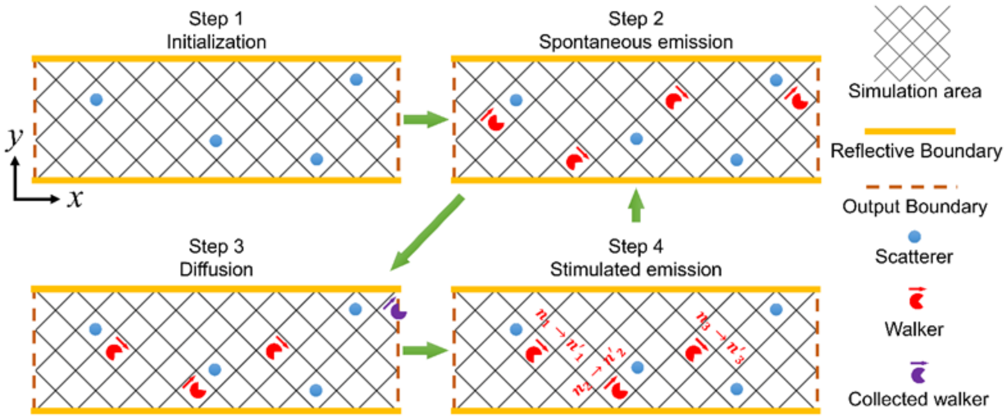

Figure 3.12 Schematic of Monte Carlo simulation model, which consists of four steps. Step 1, initialization. Step 2, spontaneous emission. Step 3, diffusion. Step 4, stimulated emission.

Step 1: Initialization. The scatterers are generated and occupy the cells. Their positions are randomly distributed among the simulation region. The total number of the scatterers is determined by the mean free path l_{mpf}. The unoccupied cells behave as the active medium and they are homogeneously excited to have the initial population $N(x, y) = N_0$ at the initial time. The total initial energy (pump power) is $E_0 = \hbar\omega_0 \iint N_0 dxdy$, where ω_0 is the central frequency of spontaneous emission.

Step 2: Spontaneous emission. Each cell (active medium) undergos a spontaneous emission process with a probability $(\gamma_0 N)$ determined by its population $N(x, y)$ and the decay rate γ_0. When this event occurs, a new walker is generated to carry one photon ($n_i = 1$) with frequency ω_i and a random propagation direction. The frequency ω_i is randomly selected among 1001 channels (from -500 to 500 channel centered with frequency ω_0 i.e. channel 0) with a linewidth of Ω channels according to Gaussian distribution. Meanwhile, the population $N(x, y)$ of this cell is reduced by one unit.

Step 3: Diffusion. All the walkers located in the simulation region move one unit along their propagation directions to their neighbor cells. When a walker encounters a reflective boundary or a scatterer, its propagation direction changes and its position is updated accordingly. When a walker reaches the output boundary, it is “destroyed” (i.e. escaped from the simulation region) and its information (photons n_i and frequency ω_i) is collected.

Step 4: Stimulated emission. Each walker interacts with the cell in the same position. Part of the population of the cell transfers to the walker and increases the walker’s photons according to the following equation: $N(x,y) \to [1-\gamma(\omega_i)n_i]N(x,y)$, $n_i \to [1+\gamma(\omega_i)N(x,y)]n_i$, where $\gamma(\omega_i) = \gamma_0/[1+(\omega_i/\Omega)^2]$ is the stimulated emission coefficient.[87,96]

Compared with previous studies using Monte Carlo method to model the RL systems, four major modifications are made in the numerical model to satisfy the real experimental conditions of the POFRL system. Fist, the simulation region here is set to be rectangular with large length-width ratio, conforming to the geometric structure of the POFRL. Second, reflective boundary condition has been introduced to the two long sides of the simulation region as an analogy of the core-cladding interface in the POFRL to provide the waveguide effect. Third, since the two parallel long sides of the simulation region are reflective boundary in the numerical model, a 45° rotation is introduced to the orthogonal grids (i.e. the available diffusion directions of photon walkers) to avoid the trapping of the photon walkers. Fourth, the scatterers in the model are immobile, whereas the scatterers in previous studies have variable positions in each simulation step. Because their RL systems are based on liquid where the scattering scattering particles are free to move in the liquid.

3.6.2 Simulation results

The simulation region was initialized to be $L_x = 500,\ L_y = 50$, and has a large length-width ratio like the POFRL configuration. Other parameters were set in the simulation as $l_{\mathrm{mpf}} = 100,\ \gamma_0 = 2 \times 10^{-5}$, and $\Omega = 50$ channels, respectively. The mean free path l_{mpf} is comparable to the size of the simulation region corresponding to a weakly scattering regime. Then the simulation model was performed many times at different pump powers. Figure 3.13 shows the numerical spectra at three different pump powers. These pump powers were $E_0 = 1.6 \times 10^6\ \hbar\omega_0$ (subthreshold), $E_0 = 2 \times 10^6\ \hbar\omega_0$ (near threshold), and $E_0 = 6 \times 10^6\ \hbar\omega_0$ (well above threshold), respectively. At subthreshold pump power, only one broad spontaneous emission can be observed in the spectra (Figure 3.13a). Then, several discrete narrow peaks appeared as the pump power increased to near threshold (Figure 3.13b). Each individual sharp peak in the numerical spectrum indicates one or several photon walkers which have long light path in the active medium and experienced strong amplification.[98] When the pump power increases well beyond the threshold, same with the experimental observations, the numerical spectrum consists of only one narrow peak (Figure 3.13c). This is because the high pump power boosts the number of the walkers. These photon walkers are strongly coupled by the interaction with the background active medium, leading to the average effect on amplification and limited photon number fluctuations for each walker.[87] The simulation results clearly prove that the simulation model exhibits random lasing behavior, similarly with the POFRL.

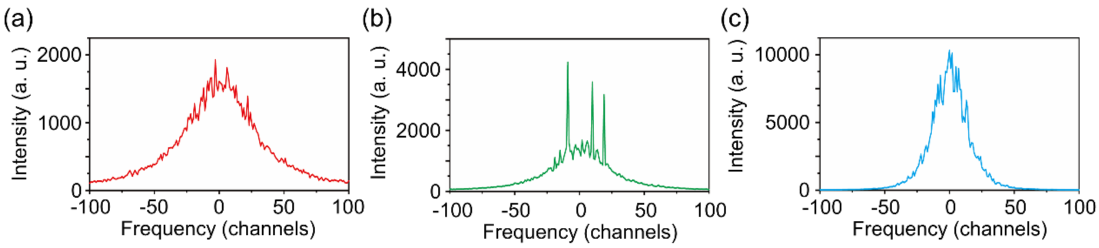

Figure 3.13 Numerical spectra at three different pump powers (a) $E_0 = 1.6 \times 10^6\ \hbar\omega_0$, (b) $E_0 = 2 \times 10^6\ \hbar\omega_0$, and (c) $E_0 = 6 \times 10^6\ \hbar\omega_0$.

In order to show the influence of waveguide effect on the calculated lasing spectra, a set of simulations using the numerical model without refractive boundary as an analogy of the absence of waveguide effect was performed, the results are shown in Figure 3.14. It can be seen that no lasing peak can be observed without the refractive boundary, indicating that the waveguide effect is indeed the cause of the lasing.

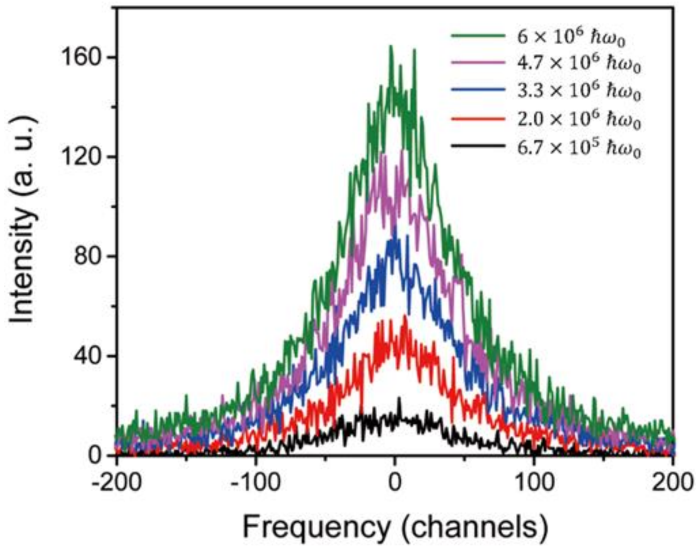

Figure 3.14 Numerical spectra from simulation model without refractive boundary at different pump powers.

In order to further confirm that this numerical model is suitable for the POFRL, five numerical spectra were calculated at the same pump power near threshold ($E_0 = 2 \times 10^6\ \hbar\omega_0$), as shown in Figure 3.15. In each spectrum, several lasing modes could be found. Some lasing modes also appeared in other spectra but their lasing intensities were different. Such lasing intensity fluctuation suggests that the numerical model exhibits mode competition phenomenon, which has been observed in the experiments. In the following, I will analyze the sources of the lasing modes in the numerical model. In general, two types of lasing modes could co-exist in the RL systems.[15] One is the localized modes generated from fixed laser cavities with resonant feedback.[88] Another is the extended modes generated from spatially extended fields in gain medium with non-resonant feedback.[98] In particular, the extended modes were observed in liquid RL systems as well as their corresponding numerical models.[19,87,98] However, the scatterers in their experimental and numerical systems are fluid, thus only extended modes can be formed to generate random lasing. In this case, the POFRL is a solid RL system and the scatterers in the numerical model are immobile, which could establish the fixed laser cavities. In contrast to the localized modes, the Q factor of the extended modes is much lower.[15] As a result, the laser peaks of extend modes show less sharpness compared with that of cavity modes. On the other hand, the extended modes are generally found to be in the central region of the gain curve where the gain is highest due to their low Q factor.[15] Moreover, the extended modes show huge shot-to-shot fluctuation because they have a large spatial overlap with other modes.[15,100] Based on the above-mentioned features of the extended modes, the modes numbered 6 and 7 in Figure 3.15 are likely to be the extended modes. Whereas the other modes in the numerical spectra should be related to the fixed laser cavities.

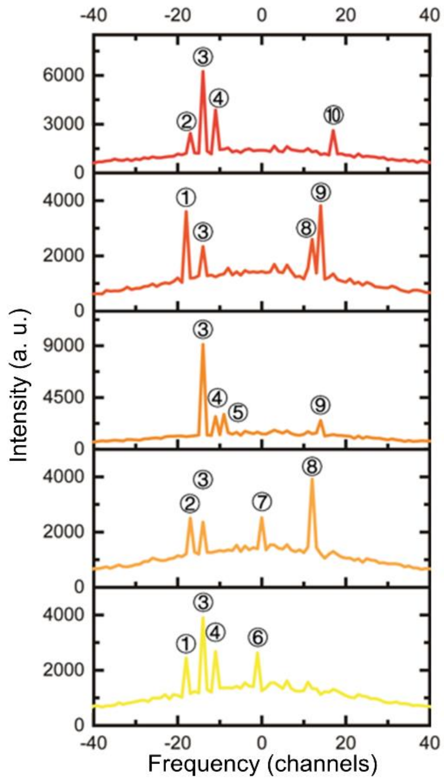

Figure 3.15 Numerical spectra for five different shots at the same pump power $E_0 = 2 \times 10^6\ \hbar\omega_0$. The lasing modes are marked with numbers from 1 to 10.

3.7 Summary

In summary, a method to fabricate TiO_2 scattering particles doped POFRLs has been developed. Although the scattering strength provided by TiO_2 scattering particles is located in weakly scattering regime, multimode and coherent random lasing can still be observed in the POFRLs. Based on PFT analysis, it was found that the laser cavity length was 32.6 μm, which is much shorter than the scattering mean free path (l_s=600 μm) provided by the TiO_2 scattering particles, indicating that the waveguide configuration plays an important role in generating coherent random lasing. Using the

POFRLs as the illumination source, the spatial coherence of the PORFLs was investigated and a speckle free imaging application was presented. Finally, a two-dimensional four-level numerical model based on Monte Carlo dynamic was proposed to describe the lasing dynamic in the POFRLs. The numerical model is composed of the waveguide effect, immobile scatterers and random photons walkers according to the physical configuration of the POFRL system. The simulation results show the random lasing spectra and mode competition phenomenon, which are in a qualitative agreement with the experimental observations. A more quantitative description will be provided in the future. This work built a primary connection between the theoretical models and experimental works performed in POFRL, which will benefit the future research in this field and its applications.

Chapter 4 Biofluidic Random Laser Cytometer for Biophysical Phenotyping of Cell Suspensions

4.1 Introduction

Optofluidics that synergistically combine optics and microfluidics are the keys to the next generation cytometers.[101,102] Due to the flexibility of microfluidic system, optofluidic devices show great promise for numerous applications, particularly for bio-sensing platform.[103–106] One of the most remarkable optofluidic devices is biofluidic laser, which integrates biological liquid suspensions and optical cavities into compact optofluidic system.[107] The lasing properties such as intensity, spectrum, and threshold are sensitive to specific biomarkers such as biophysical alternations of the samples, which provided an label-free approach to the liquid biopsy diagnostics.[107] Compared with the traditional optofluidic bio-sensing devices using fluorescence (*i.e.* spontaneous emission) as the sensing signals, the biofluidic laser shows several merits. First, the laser signal exhibits much higher peak intensity with a very narrow linewidth (normally, below one nanometer), and delivers higher signal-to-noise ratio (SNR) hence the signal is easier to be detected and determined.[107] Second, the laser feedback is an innate amplifier for optical signal variation induced by the biophysical alternations of the liquid biopsies, endowing the biofluidic laser with a high sensitivity.[108] Third, the unique threshold of lasing in a biofluidic system is highly correlated with the biophysical state, which is a sensitive indicator for the biomarker detection. Therefore, biofluidic lasers have attracted great interest and a lot of attention has been devoted to this topic.[107] To date, biofluidic lasers have been demonstrated in various configurations wherein the laser feedbacks are provided by optical cavities of various configurations, such as high-Q ring resonators,[108–110] Fabry-Perot cavities,[111,112] and distributed feedback gratings[113,114]. These well-defined optical cavities generally require precise design and fabrication. For example, Fabry-Perot cavity consists of a pair of mirrors which need to be perfectly aligned to each other. This would increase the manufacturing costs and difficulty, which limits the developing of the biofluidic lasers.[111] Therefore, there is a need to achieve laser feedback in optofluidic devices via a facile approach.

A cavity-free optofluidic laser has been proposed by Shivakiran Bhaktha and colleagues in 2012.[115] In their work, the conception of RL was firstly introduced into the optofluidic devices to achieve laser feedback without optical cavities. Different from traditional lasers, laser feedback in RLs is provided by multiple light scattering in disordered systems containing gain medium.[52,80] This unique laser feedback renders many advantages to RLs that include ease of fabrication and controllable lasing properties (e.g. intensity, wavelength, threshold, and direction).[57] Although several studies have investigated the random lasing properties in optofluidic systems,[43,116] applying RLs in biofluidics for bio-sensing is still very challenging, mostly due to the limited understanding of the intercellular and intracellular biophysical properties of the biopsies[108]. However, by carefully choosing biophysically well-defined bio-samples, the biological tissues have already been demonstrated that they are suitable media to induce the generation of random lasing. In 2004, Polson and co-researchers firstly reported that random lasing can be observed in gain-medium-infiltrated human colon tissues that was composed of highly hierarchical structures.[45] Thereafter, the random lasing action has been achieved based on other biological tissues, such as chicken breast,[117] bone tissue[118] and butterfly wings[119,120], in which solid niche (e.g. in bone tissue) or fibers (e.g. in chicken breast and butterfly wings) can provide strong scatterings and form laser cavities. Clinically, it has been proposed that RLs have the potential application for tumor detection because the lasing properties are highly sensitive with the malignant alternations of the tumor tissues.[46] It was found that the RL induced by the cancerous tissue exhibited more laser modes than that induced by the healthy tissue, which might be due to the more heterogeneous cancerous tissue that provides more laser cavities.[45] For instance, Wang *et al.* has demonstrated that the human breast tumor tissues with different malignancy grades were highly correlated with the specific RL spectra and thresholds.[46]

However, previous demonstrations of RL in biosensing on solid tissues suffered from the availability of solid biopsies in clinical practices. Comparing to solid tissues that need surgical cutting from the disordered organs, liquid biopsies are much easier to obtain in clinical practices. Importantly, liquid biopsies, such as circulating tumor cells (CTCs) that shed from the primary tumors, provide prognostic biomarkers at the very initiation of the disease. Thus, it is of great value to apply novel biosensing techniques to liquid biopsy prognostics. Technically, RL detection at the subcutaneous vessel is inherently noninvasive, which could be developed *in vitro* by the biofluidic platform embedded with RL peripheries. The advantages of applying RL in liquid biopsy prognostics are considerable. As far as we are aware, no study on the application of RL to biological liquids *in vitro* or *in vivo* has been conducted.

In this chapter, I will present a novel biofluidic RL (BFRL) cytometer for the characterization of cell suspensions. Suspensions of human breast epithelial cells (MCF-10A) and human breast cancerous cells (MCF-7 and MDA-MB-231) are used. The BFRL is achieved by lasing in a geometrically well-defined microfluidic channel filled with cell suspensions added with gain medium. The lasing properties are distinct when different types of cells are introduced, which enables the identification of the different cell types via analyzing the random lasing spectra. Careful analysis reveals the roles of biophysical alternations of the cell suspensions in determining the specificity of the laser spectra. To the best of our knowledge, this is the first demonstration of using BFRL to distinguish normal and cancerous cells in liquid suspensions, which paves the way towards novel cytometers for liquid biopsy prognostics.

4.2 Preparation of cells

Human breast epithelial cells (MCF-10A), breast cancerous cells (MCF-7 and MDA-MB-231) were obtained from ATCC (Manassas, VA). MCF-10A cells were cultured in the Mammary Epithelial Growth Medium (MEGM; CC-3150, Lonza, Walkersville, MD) added with 0.4 % (v/v) bovine pituitary extract (BD, Franklin Lakes, NJ), 0.1 % (v/v) human epithelial growth factor (hEGF; Cell Signaling Technology, Beverly, MA), 0.1 % (v/v) hydrocortisone (Sigma-Aldrich, St. Louis, MO), 0.1 % (v/v) insulin (Sigma-Aldrich) and 0.1 % (v/v) of a reagent mixed with 30 mg/ml gentamicin and 15 μg/ml amphotericin (GA-1000, Lonza). MCF-7 cells were cultured in a high-glucose Dulbecco's modified Eagle's medium (DMEM; Invitrogen, Carlsbad, CA) with the supplement of 10 % fetal bovine serum (Atlanta Biological, Atlanta, GA), 0.5 μg/ml fungizone (Invitrogen, Carlsbad, CA), 5 μg/ml gentamicin (Invitrogen), 100 units/ml penicillin, and 100 μg/ml streptomycin. MDA-MB-231 cells were cultured in DMEM-F12 (Invitrogen) added with 10 % fetal bovine serum and 100 units/ml penicillin. All cells were cultured at 37 °C with ~100 % humidity and 5 % CO_2 in an incubator. To obtain suspended cells for the experiments, 0.25 % trypsin-EDTA in phosphate buffered saline (PBS) was used to re-suspend the cells, following by centrifuge and replacement of fresh culture media. The cells were then diluted to the target cell density ($\sim 2 \times 10^6$ cells/ml) by adding additional culture media and 2.5 mM Rhodamine 640 dye before injected into the optofluidic device. Rhodamine 640 is commonly used in flow cytometry for labelling and it causes minimal influences to the suspended cells.[27] All the experiments were conducted within 2 hr after the cells were suspended.

4.3 Fabrication of optofluidic device

The optofluidic device is fabricated by standard photolithography based on the replica molding of elastomeric polydimethylsiloxane (PDMS) (Sylgard-184, Dow Corning, Midland, MI). First, a 35 μm thick layer of negative photoresist (SU8-2025, MicroChem, Westborough, MA) with a zigzag channel was designed and patterned on a silicon wafer. The mold master was the silanized with vaporized (tridecafluoro-1,1,2,2,-tetrahydrooctyl)-1-trichlorosilane (Sigma-Aldrich, St. Louis, MO) in a vacuum chamber. The PDMS substrate containing microchannels was fabricated by the soft lithography procedures. The PDMS substrate was then bonded onto a glass slide (Citoglas, Jiangsu, China) by oxygen plasma treatment. Figure 4.1 shows the (Scanning Electron Microscope) SEM image of the as-fabricated optofluidic device. The width of the channel is 400 μm and the total length of the channel is 3 cm. The design of the zigzag shape is to promote random lasing, as it has been reported that the channels with multi-scattering structures for light can enhance the efficiency of random lasing and reduce the lasing threshold.[18,43,115]

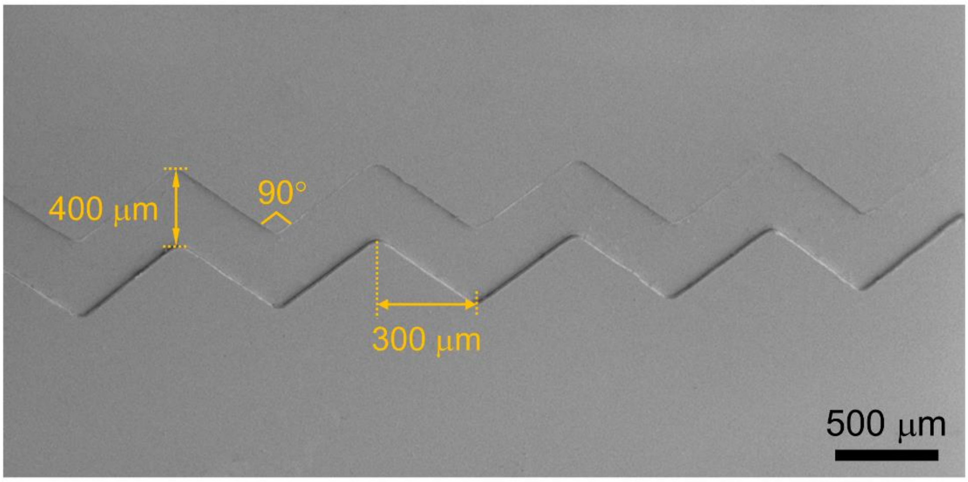

Figure 4.1 SEM image of the zigzag channel in the BFRL. The detailed structure parameters are indicated in the image.

4.4 Morphology characterization

FEI Quanta 450 FEG scanning electron microscope (SEM, Dawson, NE) at a scanning voltage of 5 kV and a spot size of 4.0 was applied to capture the images of the optofluidic channel at a tilt angle of 45º.

The cells were stained using immunofluorescence staining method at a floating state. To stain floating cells, the cells were first resuspended by using 0.25 % trypsin-EDTA in phosphate buffered saline (PBS; Sigma-Aldrich, St. Louis, MO). The cells were fixed with 4 % paraformaldehyde (PFA, Sigma-Aldrich, St. Louis, MO) in phosphate buffered saline (PBS, Sigma-Aldrich, St. Louis, MO) for 10 min and then treated with 0.3% Triton X-100 in PBS for 10 min. 10 % goat serum was applied for 1 hr to avoid non-specific binding of the staining molecules in the next steps. The Lamin-A primary antibody (Abcam, Cambridge, MA) was applied for 1hr. The cytoskeletal actin was stained with Alexa-555 conjugated phalloidin (Life Technologies, Carlsbad, CA) followed by staining the nucleus with 0.1% Hoechst 33342 (Sigma-Aldrich, St. Louis, MO) for 10 min. And the stained images were obtained by using laser confocal microscope (TCS SP8 Confocal Microscope, Leica, Germany). Bright field imaging is conducted by a phase-contrast inverted microscope (TE300, Nikon, Tokyo, Japan) and an sCMOS microscope camera (Zyla, Andor, Belfast, UK) was applied to capture high-resolution images (~570 nm/pixel).

4.5 Emission and random lasing measurement

4.5.1 Experimental set-up

The experimental set-up for random lasing measurement is similar to that used in last chapter. The pump source was a Q-switch Nd:YAG pulse laser (Continuum, Inlite II-50), operating at 532 nm wavelength with 6 ns pulse duration and 10 Hz repetition rate. A power meter (Coherent, LabMax-Top) equipped with a pyroelectric energy sensor was used to determine the pump laser power. The laser beam was focalized to the front surface of the BFRL and random lasing from the BFRL was collected by a multimode fiber with 50-μm core diameter (Thorlabs, GIF50C) located by the side of the opofluidic chip and directed to a spectrometer (Ocean Optics, HR4000). The expose time for each spectrum is set to be 1s to reduce the intensity fluctuation of the random lasing. By injecting the mixture of the cells with concentration of 2×10^6 cells/ml and 2.5 mM Rhodamine 640 dye into the zigzag channel, the BFRL was filled with liquid suspensions of MCF-10A, MCF-7 or MDA-MB-231 cells. In order to fully excite the BFRLs, a side-pumping configuration is employed, as shown in Figure 4.2. The pump laser beam was focalized by a cylindrical lens to a line of 2.5-cm long and 1-mm wide. The pump laser beam was adjusted precisely to cover the channel of BFRL to achieve uniform pumping. The zigzag channel performed as a waveguide hence the random lasing generated in the BFRL would be guided to emit through the exit of the channel. A multimode fiber was placed closed to the exit of the optofluidic channel to collect and transmit the random lasing spectra to the spectrometer. The random lasing properties of the BFRLs were then measured and analyzed under the same experiment configuration.

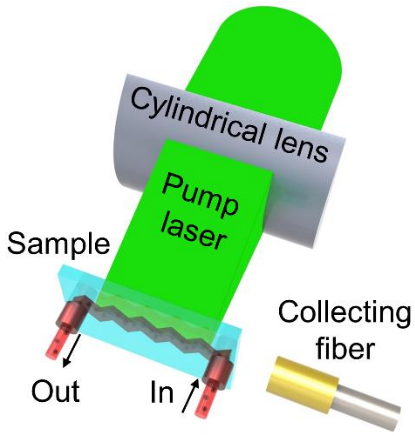

Figure 4.2 Schematic of the pump and collection configuration.

4.5.2 Evolution of the emission spectra and random lasing

Figure 4.3a shows the evolution of emission spectra recorded from the BFRL filled with MCF-10A cell suspensions excited at different pump powers. The intensity of the collected emission spectra increases as the pump power increases. More importantly, only spontaneous emissions with broad spectra between 600 nm and 660 nm were observed when the pump power was low, while a narrow emission band at ~610 nm manifested itself in the emission spectra when the pump power exceeded a certain threshold. These discrete sharp peaks emerging on the top of the narrow emission band were features of coherent random lasing and the corresponding pump power threshold was the lasing threshold.[121,122] The full-width-half-maximum (FWHM) of the main sharp peak was measured to be 0.35 nm, as shown in the insert of Figure 4.3a. Similar random lasing characteristics have also been observed in the emission spectra recorded from the BFRL filled with MCF-10A and MDA-MB-231 cells (see Figure 4.3b and c). The corresponding FWHM of the sharp peaks are 0.41 nm and 0.27 nm, respectively. It is worth noting that, for the cell suspensions with different types of cells, the intensity and profile of the random lasing spectra were different. Especially, the lasing spectra obtained from the BFRL filled with MCF-10A shows an almost smooth profile with weak lasing peaks. Such feature indicates the incoherent random lasing behavior due to the low scattering strength.[80]

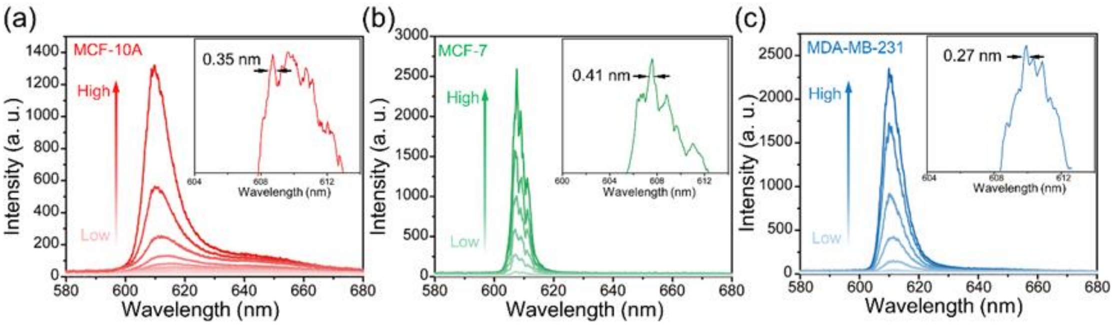

Figure 4.3 Lasing spectra of the BFRL filled with (a) MCF-10A, (b) MCF-7, and (c) MDA-MB-231 cells with same cells concentration at different pump powers. The insert in each figure shows the zoom-in lasing peaks. The FWHM of the main lasing peaks is marked.

4.6 Lasing mechanism of the BFRL filled with the cells

To get a better understanding of the origins of these spectral differences, I summarized the lasing mechanism of the BFRL and clarified these differences accordingly, see the schematic in Figure 4.4. Excited by the incident laser beam, fluorescent dyes in the zigzag channel worked as gain medium and emitted spontaneous emission. The existing of the cells provided large amount of scattering events for the emission light since the refractive index of the cells are different with the solution (~1.40 versus ~1.35).[123] The light path was increased by the zigzag shape of the channel, which dramatically increased the scattering events furthermore. All these scattering provided enough amplifications for the emission light to generate the random lasing. The multi-scattering events were the keys for the formation of random lasing and the different lasing properties reflected the different scattering conditions. In fact, highly disordered biological system that intensely scattered light displayed the typical random lasing spectra, which is characterized by multiple sharp peaks on the base spectra, as shown in Figure 4.3.[46] Moreover, the emission spectra of the BFRL with or without cells were quite different: for the optofluidic device without cells, only ASE can be observed in the emission spectrum. This means that the random lasing arises from the multiple light scattering provided by the cells.

To describe the scattering strength provided by the cells, the scattering mean free path l_s is defined as the average distance that light travels between two consecutive scattering events. This parameter is determined as[124,125]

$$l_s = \frac{1}{\rho\sigma_s}, \tag{4.1}$$

where ρ is the particle density of the cell suspension and σ_s is the scattering cross section of an individual cell. The scattering cross section σ_s is a parameter associated with the size and refractive index of the cells, given by[69,126]

$$\sigma_s = \frac{8}{3}x^4\left(\frac{n^2-1}{n^2+2}\right)^2 \sigma_g\,, \tag{4.2}$$

where $x = \pi d/\lambda$ is the so-called size parameter, n is the refractive index of the cells, d is the diameter of an individual cell, λ is the light wavelength, and $\sigma_g = \pi d^2/4$ is the geometrical cross section. Thus, equation 4.1 can be rewritten as

$$l_s = \frac{3\lambda^4}{2\pi^5 d^6 \rho}\left(1+\frac{3}{n^2-1}\right)^2, \tag{4.3}$$

The light scattering strength in BRFL is mainly determined by the biophysical properties (size and refractive index) of the cells and the cell densities. Particularly, by analyzing the sensitivities of the three parameters, it was found that the light scattering is mostly related to the single cell scattering properties.

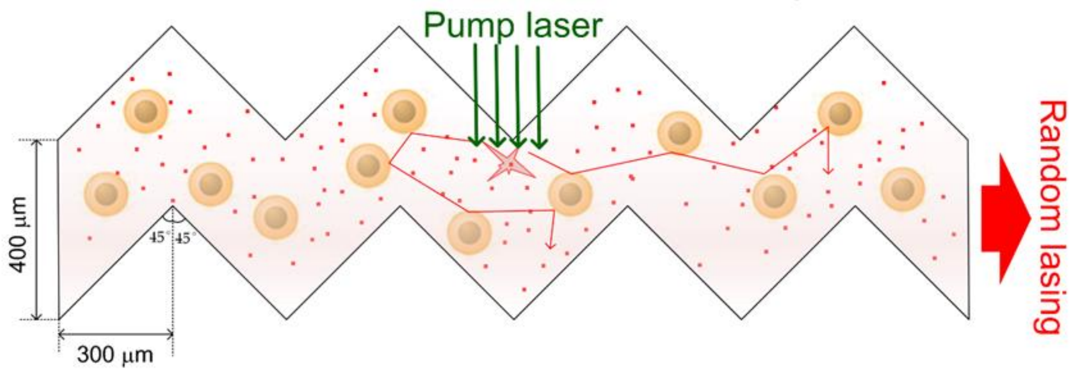

Figure 4.4 Schematic of the lasing mechanism of the BFRL. The suspended cells introduced large amounts of scattering events, which initiates the random laser.

4.7 Sensitivity analysis

According to Equation 4.3, the scattering mean free path l_s is influenced by cell refractive index n, cell diameter d and cell concentration ρ. The influences of these three parameters could be determined by standard sensitivity analysis. The sensitivity of the three parameters are:

$$\frac{\Delta l_s}{l_s} = \frac{-12n^2}{(n^2+2)(n^2-1)} \times \frac{\Delta n}{n} \approx -70.6\frac{\Delta n}{n} \tag{4.4}$$

$$\frac{\Delta l_s}{l_s} = -6\frac{\Delta d}{d} \tag{4.5}$$

$$\frac{\Delta l_s}{l_s} = -\frac{\Delta \rho}{\rho} \tag{4.6}$$

Usually, the variation of refractive index of different cell types is usually 0.15% ~0.80%,[123] which contributes to the variation of scattering mean free path by 10.6% ~

56.5%. The variation of the cell diameter between the normal cell MCF-10A and cancerous cells (MCF-7 and MDA-MB-231) is 42.9%, which contributes to the variation of the scattering mean free path by 257%. The accuracy of the cell counting method is ~2%,[127] which contributes to the variation of the scattering mean free path by 2%. It can be seen that the cell diameter and the cell refractive index are the main contributors to the variations of the scattering properties. And the error induced by the cell counting could be neglected.

4.8 The relationship between biophysical properties and the lasing threshold

4.8.1 Size of the cells

As the biophysical properties of the cells strongly influence the light scattering properties, different lasing properties could perform as the indicator of the different biophysical properties of the suspended cells. Since the density of the particle density ρ of the three cell suspensions was the same (2×10^6 cells/ml). The main parameter which influences the scattering mean free path l_s is the diameter of the cells d and refractive index of the cells n. The morphologies of the normal cells (MCF-10A) and the cancerous cells (MCF-7 and MDA-MB-231) are shown in the optical images in Figure 4.5a. The diameter of the MCF-10A cells (14.23 ± SE 0.35 μm) were much smaller while the MCF-7 cells and MDA-MB-231 cells were almost of the same size

(20.36 ± SE 0.28 μm for MCF-7 and 19.75 ± SE 0.56 μm for MDA-MB-231), as shown in Figure 4.5b.

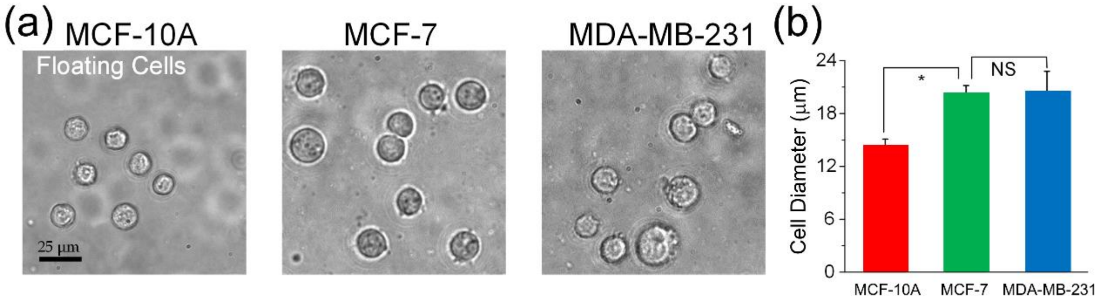

Figure 4.5 (a) Optical images of MCF-10A, MCF-7, and MDA-MB-231 cells. (b) Diameters of MCF-10A, MCF-7, and MDA-MB-231 cells. * indicates statistical significance at a level of 5%.

4.8.2 Lasing threshold

Moreover, it has been reported that the refractive index of the normal cells is lower than that of the cancerous cells.[128] According to Equation 4.3, the scattering strength provided by MCF-10A cells is much weaker than that provided by the two types of cancerous cells. The BFRL filled with MCF-10A cells shows less sharp peaks on the lasing spectra due to the low scattering strength provided by MCF-10A cells. Additionally, the intensity of the BFRL filled with MCF-10A cells is much weaker than that with other cell types (Figure 4.6). These spectral differences provide important features to distinguish cells based on their biophysical properties, and potentially is a powerful approach for label-free cell identification.

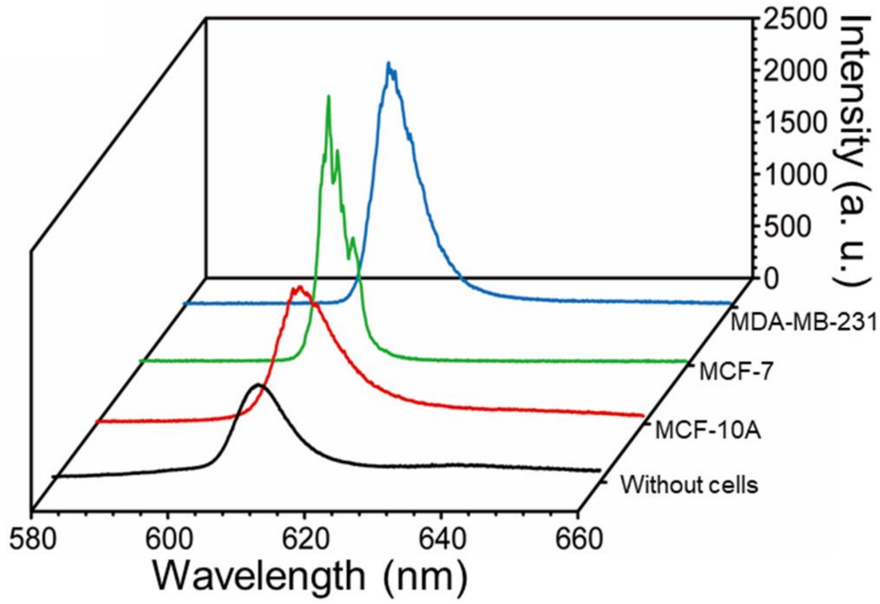

Figure 4.6 Emission spectra of the BFRL with three different cells and without cells at the same pump power.

To quantitatively analyze the influence of biophysical properties of the cells on the lasing properties, the intensities of the main lasing peak of the BFRL are extracted as a function of the pump power (Figure 4.7). Nonlinear dependences of the lasing intensities on the pump power were observed in the BFRL with all the three types of cells, exhibiting lasing threshold behavior. The lasing thresholds of the BFRL are determined to be 80.4 ± SE 1.8 nJ/mm^2 (for MCF-7), 83.8 ± SE 2.5 nJ/mm^2 (for MDA-MB-231), and 96.2 ± SE 1.6 nJ/mm^2 (for MCF-10A), respectively. The BFRL filled with MCF-10A cells exhibits the largest lasing threshold and the smallest slope value of the lasing intensity versus the pump energy. This is because the scattering strength provided by the normal cells (MCF-10A) is much weaker than that provided by the cancerous cells (MCF-7 and MDA-MB-231). As a result, the pathlength for the emission light prorogation in the BFRL filled with MCF-10A is relatively short, which means the emission light need experience more amplification to lase. Thus, the MCF-10A cells with small cell size and low refractive index can be easily distinguished based on the lasing threshold of the BFRL.

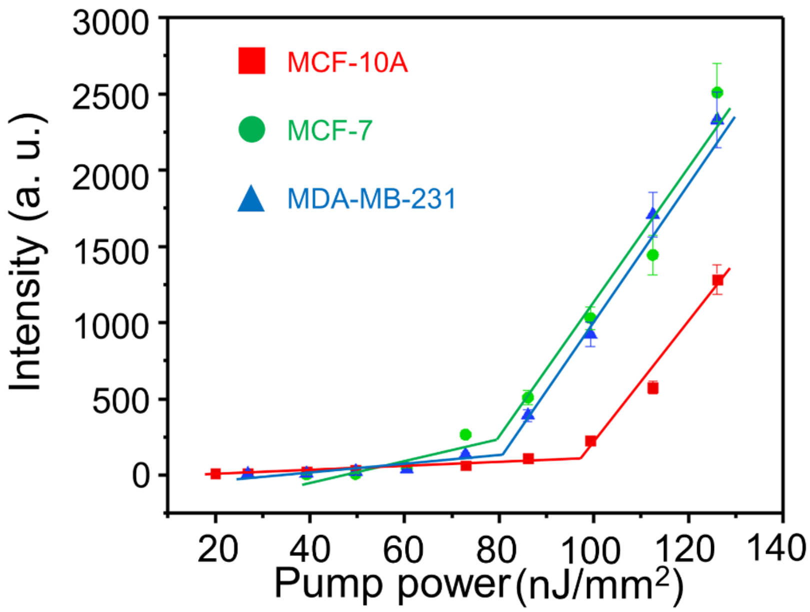

Figure 4.7 The lasing intensity as a function of pump power of the BFRL filled with three different cells.

4.8.3 Repeatability and reliability of the BFRL

To clarify the repeatability of the experiment results, all three BFRL devices has been measured 10 times. Figure 4.8a-c shows the lasing spectra obtained from five separate measurements on the three BFRL devices at the same pump power (126 nJ/mm^2). Although, the fluctuation of lasing intensity and modes can be clearly observed, which results from the intrinsic random feature of the BFRL. Such fluctuation is within an acceptable range. The lasing threshold values for the three BFRL devices still show the same tendency (Figure 4.8d), which means the threshold can be regard as an effective signal for the distinction of the cell types.

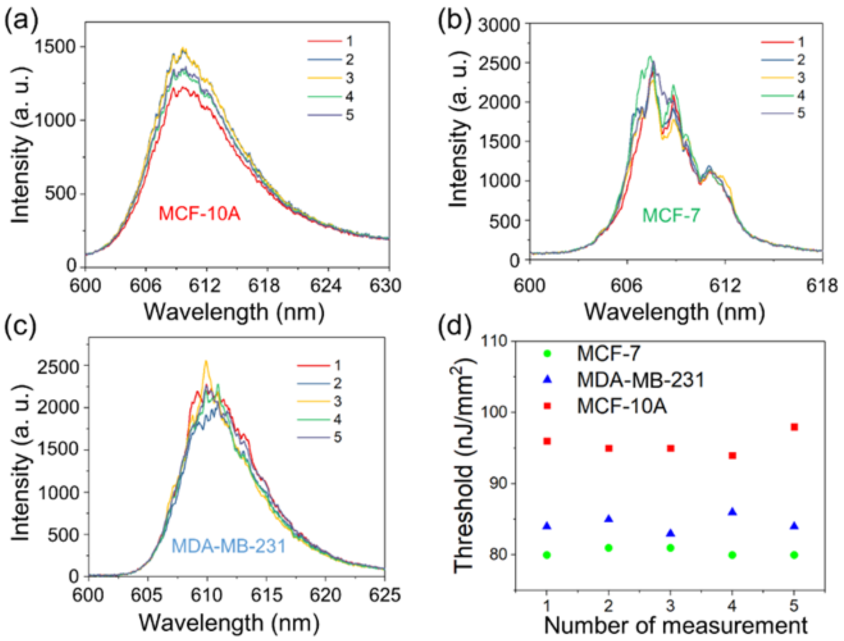

Figure 4.8 Lasing spectra obtained from five separate measurements on the BFRL filled with (a) MCF-10A, (b) MCF-7 and (c) MDA-MB-231 at the same pump power (126 nJ/mm^2). (d) The calculated lasing threshold values for five separate measurements on the three BFRL devices.

To further investigate the influence of the different batches of microfluidics and cells, more experiments were carried out. Figure 4.9 shows the lasing spectra from the three different batches of microfluidics under the same experiment condition. The lasing spectra are slightly different between each other regarding to the spectrum profile. Such spectrum fluctuation is caused by the variation of the laser cavities (i.e. light path loop). The laser cavities are formed by the scattering and reflection provided by the cells and the microfluidics. Either the microfluidic device or the cells were changed, the laser cavities would vary accordingly. The intensity fluctuation arises from the intrinsic properties of RL (e.g. competition between the laser cavities).[129] However, the main peak positions of the laser spectra are always same. This is because the main peak positions are determined by the scattering strength of the whole system. Although there might be some random errors that have been introduced to the different microfluidic devices due to the fabrication. Such random errors are normally less than 1 μm (i.e. photolithography precision) and the induced variation of scattering strength can be neglect compared with the whole system.

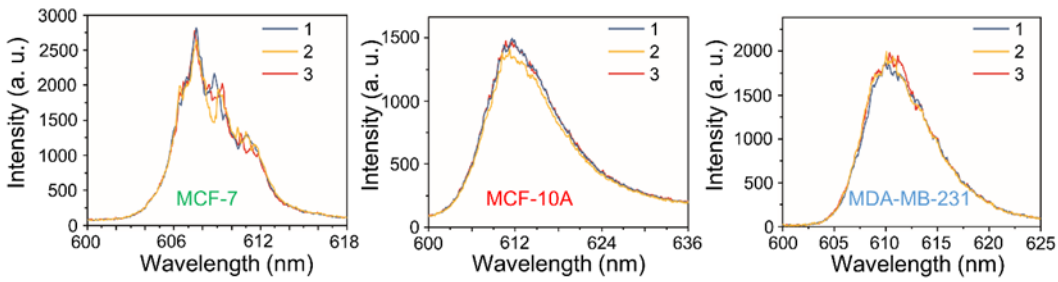

Figure 4.9 Lasing spectra from the BFRLs built in three different batches of microfluidic device with identical microfluidic design under same experiment condition. Total three microfluidic devices are tested, and the lasing spectra are labeled as batch 1,2,3, respectively. Batch 1 is the result shown in main text.

In the case of the sample with different cell batches, the measured laser spectra from the experiments are shown in Figure 4.10. The results are similar with that using different batches of microfluidics. The reason is also the same. Using different cell batches will only change the laser cavities in the system but not change the scattering strength of the whole system. Thus, the BFRL is still reliable among the samples with different cell and device batches.

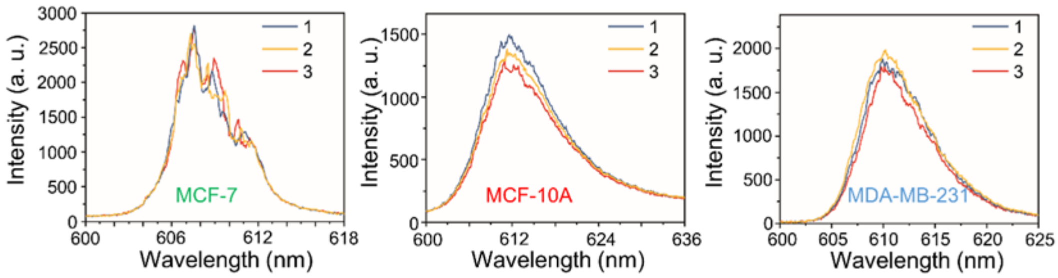

Figure 4.10 Lasing spectra from the BFRLs with different cell batches under same experiment condition. Total three cell batches are tested, and the lasing spectra are labeled as batch 1,2,3, respectively. batch 1 is the result shown in main text.

4.8.4 The influence of cell density on lasing threshold

Besides the size and the refractive index of the cells, the cell density also shows an important influence on the laser thresholds because the scattering strength of the BFRL are highly dependent on the filled cell density. To verify this influence, a set of experiments with cell density varied from 7×10^3 cells/ml to 8×10^7 cells/ml was carried out, results are shown in Figure 4.11. The threshold of the BFRL with different types of cells all show sustained reduction as the cell density increases. Similar density dependent threshold variation has been reported in previous studies.[130–132] This phenomenon can be explained as following. When the cell density is low (i.e. low scattering strength), the system is operated in the weakly diffusion region and the optical feedback provided by the system is too low to form effective laser cavity. In this case, the emission spectra are mainly manifest as ASE or incoherent random laser. With the increasement of the cell density, the optical feedback gradually becomes strong enough to form several laser cavities with sufficient quality factor. Accordingly, the laser threshold is decreased, and discrete sharp peaks emerges on the top of the emission spectra. However, when the cell density becomes larger than 10^7 cells/ml, the increasement of the cell density will not significantly reduce the lasing threshold. This is because the cells with large density forms numerous laser cavities, which cause the strong mode competition and consume large pump energy. In this study, the cell density is set to be 2×10^6 cells/ml. Under this cell density, the laser threshold values are low and the differences between the laser threshold values of the BFRL with different cell types are distinct.

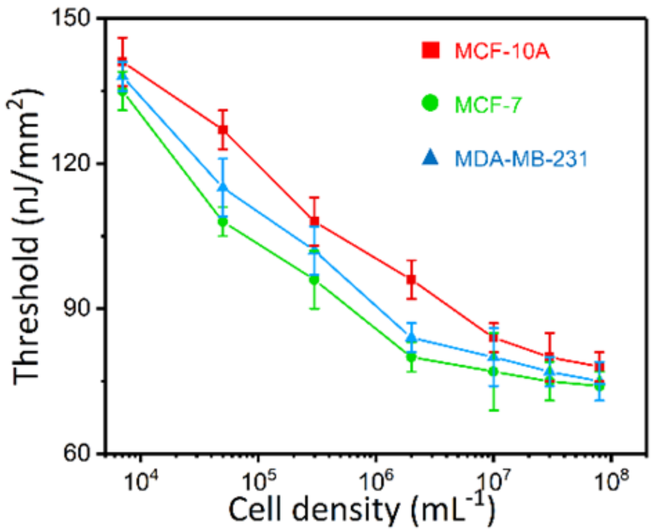

Figure 4.11 The threshold values of the BFRL devices as a function of the cell density.

4.9 The relationship between subcellular biophysical properties and lasing wavelength

The lasing threshold is an effective indicator related to the whole cell biophysical property – cell size and refractive index, and we used these indicators to successfully draw a distinction between the normal cells and the cancerous cells. However, the lasing threshold of the BFRL filled with the cancerous cells are similar to each other. To distinguish the MCF-7 cells from the MDA-MB-231 cells, their lasing spectra are carefully compared, as shown in Figure 4.12a, of the BFRL filled with the cancerous cells at the same pump power of 126 nJ/mm^2. The intensities of these two lasing spectra are similar. It is observed that the lasing wavelength of the BFRL filled with MCF-7 cells has a 2.3 ± SE 0.2 nm blue-shift with respect to that of the BFRL filled with MDA-MB-231 cells. This lasing wavelength shift phenomenon has been observed in previous studies, wherein the scattering strength of the RL system is variable.[18,69,74,133,134] The corresponding mechanism can be illustrated based on analyzing another important biophysical property such as refractive index. For example, Hu *et al* shows that 0.011 refractive index variation could result in a spectral shift up to 18.5 nm.[69] In this case, the refractive index of the MCF-7 cells (1.401) is higher than that of MDA-MB-231 cells (1.399),[123] and it is very likely that one of the main sources for the 2.3 nm spectral shift is coming from the small difference (0.002) of refractive index (also see the sensitivity analysis section 4.7). Thus, RL delivered a very high precision quantification of refractive index variations of biological samples, which could be used to develop high precision cytometers. Theoretically, high refractive index and short light wavelength will result in a short scattering mean free path, leading to more scattering events, see Equation 4.3. The BFRL system with strong scattering strength would trap light effectively and increase the light propagation path inside the system. The longer the light path is, the stronger amplification the emission light experiences. As a result, the emission light at short wavelength band would be preferentially amplified to lase as the scattering strength of the BFRL increases. Consequently, the MCF-7 and MDA-MB-231 cells can be distinguished based on this spectral blue-shift observation.

According to the discussion in the previous section, the BFRL filled with MCF-10A cells shows the weakest scattering strength due to the small cell size. Therefore, its lasing wavelength should have a red-shift compared with the other two samples. However, it can be seen from Figure 4.12b that the lasing wavelength of the BFRL filled with MCF-10A cells is almost the same with that of the BFRL filled with MDA-MB-231 cells at high pump power. This means there are other effects that play an important role in the spectral shift.

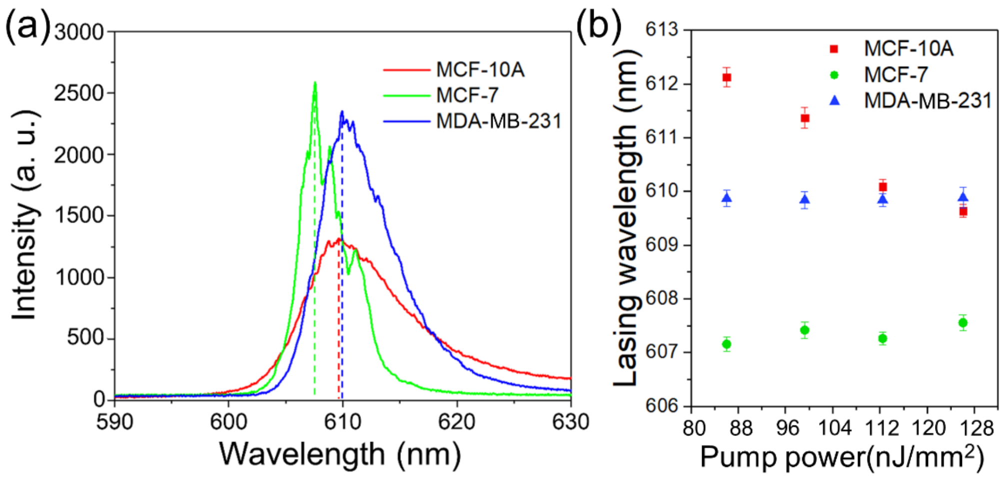

Figure 4.12 (a) Lasing spectra of BFRL filled with MCF-10A cells (red curve), MCF-7 cells (green curve), and MDA-MB-231 cells (blue curve) at the pump power of 126 nJ/mm^2. (b) The lasing wavelength of BFRL filled with MCF-10A cells (red square), MCF-7 cells (green circle), and MDA-MB-231 cells (blue triangle) as a function of pump power.

To interpret this observation, the subcellular biophysical properties of the cells were taken into account. Figure 4.13a-c shows the core-shell structure of three different cell lines. Clear shell subcellular structure can be observed in the normal cells (MCF-10A). The cell cortex (represented by the cortical actin, stained in red) and the nuclear lamina (represented by Lamin-A, stained in green) are the two structural shells of the cell.

Nevertheless, due to the epithelial-mesenchymal transition (EMT) during cancer progression, the rigid structural proteins are down regulated and thus the shell structure of the invasive cancerous cells (MDA-MB-231) become less obvious.[135] In order to show how the subcellular biophysical properties of the cells affect the lasing properties, I present the schematic of a typical light path loop in BFRL, as shown in Figure 4.13d. The light path in the BFRL consists of two parts, one is the light traveling in the gain medium, another is the light traveling inside the cells. The latter one would be manipulated by the subcellular biophysical properties of the cells, which further influence the lasing properties of the BFRL.[136–138] Since the gain medium is outside of the cells, the light traveling inside the cells cannot be amplified. For normal cells (MCF-10A), the hierarchical subcellular structure would scatter the light out and prevent the light traveling inside the cells. This light scattering strength is inversely proportional to the light wavelength. It means that the emission light at short wavelength band travels less pathlength inside the cells and avoids the loss, resulting in a blue-shift of the lasing spectra. For the MDA-MB-231 cells, the scattering strength provide by the cortical shell and the lamina shell is relatively week because of the homogenized shell structure.[139,140] Thus the light inside the cancer cells cannot be amplified and the lasing wavelength of the BFRL filled with the MDA-MB-231 cells shows no obvious different from the case with the MCF-10A cells, which deviates from the scattering theory. Moreover, this subcellular biophysical structure difference could also be one of the main contributions to the spectral shift between the BFRL filled with MCF-7 and MDA-MB-231 cells.

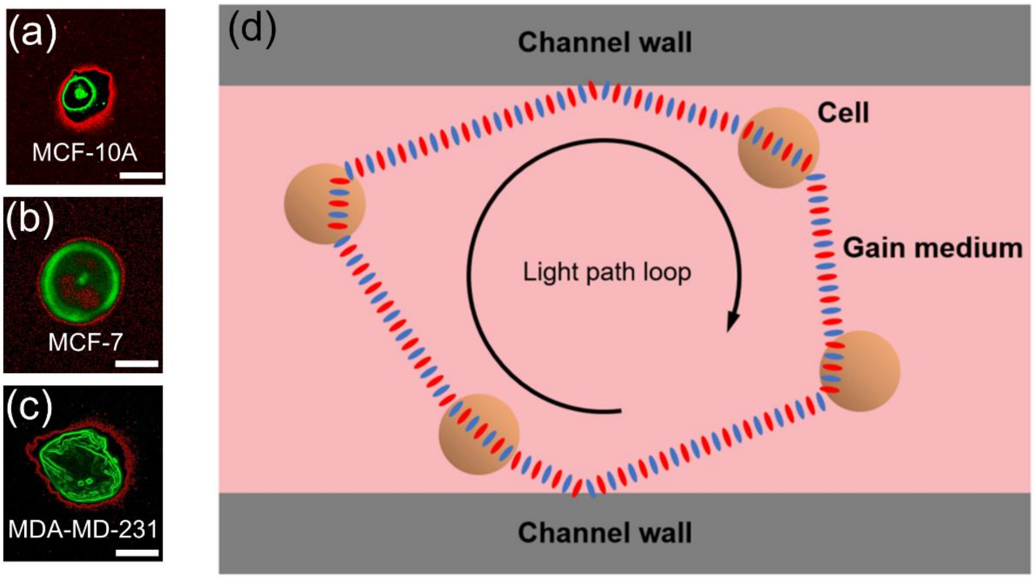

Figure 4.13 (a-c) Immunostaining of the three types of cells. The cortical actin (red) and the nuclear lamina Lamin-A (green) represent the shell structures of the cell. The scale bar indicates 10 μm. (d) Schematic of the light path loop in BFRL. The pink background represents the solution contains gain medium. The brown circles represent the cells. The light path is indicated by the wavefronts as the intercalated red and blue ellipses.

4.10 Power Fourier transform analysis and laser cavity size in the BFRL

Equivalent lasing cavity in the BFRL is a comprehensive indicator of the light scattering properties of the cell suspensions, which could be extracted from the lasing spectra. The equivalent lasing cavity is thus highly related to the biophysical properties of the suspended cells, such as cell size, refractive index, subcellular structure. The power

Fourier transform (PFT) analysis as performed to verify the sizes of the lasing cavities excited in the BFRL.[141] Figure 4.14 shows the PFT results (in $k = 2\pi/\lambda$ space) of the random lasing spectra recorded in the BFRL at the same pump power of 128 nJ/mm^2. For each sample, five spectra from five identical measurements are analyzed to verify the repeatability. The peaks in the PFT results corresponds to the Fourier components $p_m = mnL_c/\pi$, where m is the order of the Fourier harmonic, n is the refractive index of the liquid medium of the BFRL, and L_c is the pathlength of the lasing cavity. The fundamental Fourier components $p_{m=1}$ (i.e. the optical pathlength) of the three PFT results are determined to be 29.0 ± SE 0.5 μm, 12.1 ± SE 0.3 μm, and 21.9 ± SE 0.7 μm, respectively. For $n = 1.3611$, the L_c of the BFRL are calculated to be 66.9 ± SE 1.2 μm (with MCF-10A), 27.9 ± SE 0.7 μm (with MCF-7), and 50.5 ± SE 1.6 μm (with MDA-MB-231), respectively. The BFRL filled with MCF-7 cells has the smallest laser cavity, whereas the BFRL filled with MCF-10A cells has the largest laser cavity. The size of the laser cavity is associated with scattering strength in the RL system. The laser cavity with small size means that the scattering strength in RL system is strong, and vice versa. Based on the previous discussion regarding to the lasing threshold, the BFRL with MCF-10A shows weakest scattering strength among the three BFRLs, which is consistent with the PFT results. However, it should be noticed that the PFT results show obvious differences between the BFRLs with MCF-7 ($p_{m=1}$=12.1 μm) and MDA-MB-231 cells ($p_{m=1}$=21.9 μm). This is because the PFT analysis extracts and reveals the small variation in the lasing spectra (e.g. wavelength shift). The calculated cavity sizes are bigger than the individual cells. It means the lasing cavity is formed by several cells, which comprises both the light path in the gain medium and inside the cells. As mentioned in pervious discussion, the light path inside the MDA-MB-231 cells are longer than other cases due to their subcellular biophysical structure. The light travels inside the cells cannot experience gain amplified. Thus, the light path in the gain medium should be longer to obtain sufficient gain to lase, which results in a large laser cavity in the BFRL with MDA-MB-231 cells. This means that the PFT results are in good agreement with above findings based on the lasing spectra. This suggests that the BFRL can be used to identify the different biophysical properties and consequently distinguish normal and cancerous cells in liquid suspensions via analyzing the random lasing properties.

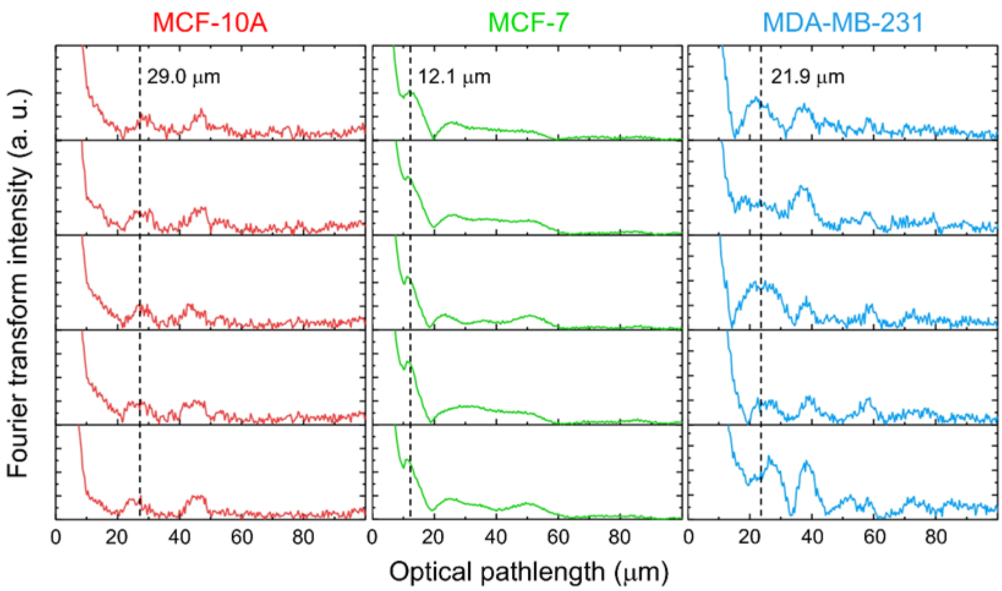

Figure 4.14 The power Fourier transform results of the lasing spectra of the BFRL with three different cells. The optical pathlengths of the first order Fourier harmonic are listed in each curve. For each sample, five spectra from five identical measurements are analyzed.

4.11 Cell type classification and detection of floating cancerous cells using BFRL

Tumor cells are shed into liquid biopsies during the whole carcinoma development. Highly aggressive circulating tumor cells often appears during the later stages of the cancer progressions.[142] Detection of floating cancerous cells in liquid biopsies is one of the core concerns in clinical practices.[143] Biophysical alterations of malignant tumor cells are hallmarks of cancer cells. For example, tumor cells in liquid biopsies tend to be much larger than the normal cells and with higher refractive index.[144] Also, the more malignant tumor cells tend to contain more disrupted cytoskeletons.[145] Considering the BFRL successfully characterized the biophysical properties of the suspended cells, the BFRL properties can be used as the indicators to classify the cells and detect the cancerous cells in a cell mixture.

We firstly determine the most important BFRL properties by principle component analysis (PCA). Three properties (i.e. threshold, peak shift and optical pathlength of fundamental Fourier component $p_{m=1}$) are chosen in the PCA model. PCA delivers linear combinations of the three parameters and the lower-order component dominant the features for classifying the cell types.[146] In the analysis, the first-order principle component is $0.68 \times \text{threshold} + 0.10 \times \text{peak shift} + 0.73 \times \text{optical pathlength}$, in which the optical pathlength is the most important property for cell classification and the threshold comes next. The cell classification result by the first-order and the second-order principle component (indicated by principle component 1 and principle component 2, respectively) is shown in Figure 4.15a. Using a single indicator of the principle component 1, the three types of cells are successfully classified, as shown in the colored rectangular blocks in Figure 4.15a. On the other hand, Using the dominant BRFL properties (i.e. threshold and optical pathlength) for cell type classification, we can only classify the three cell types model in a two-dimensional map by using the two properties together, as shown in Figure 4.15b.

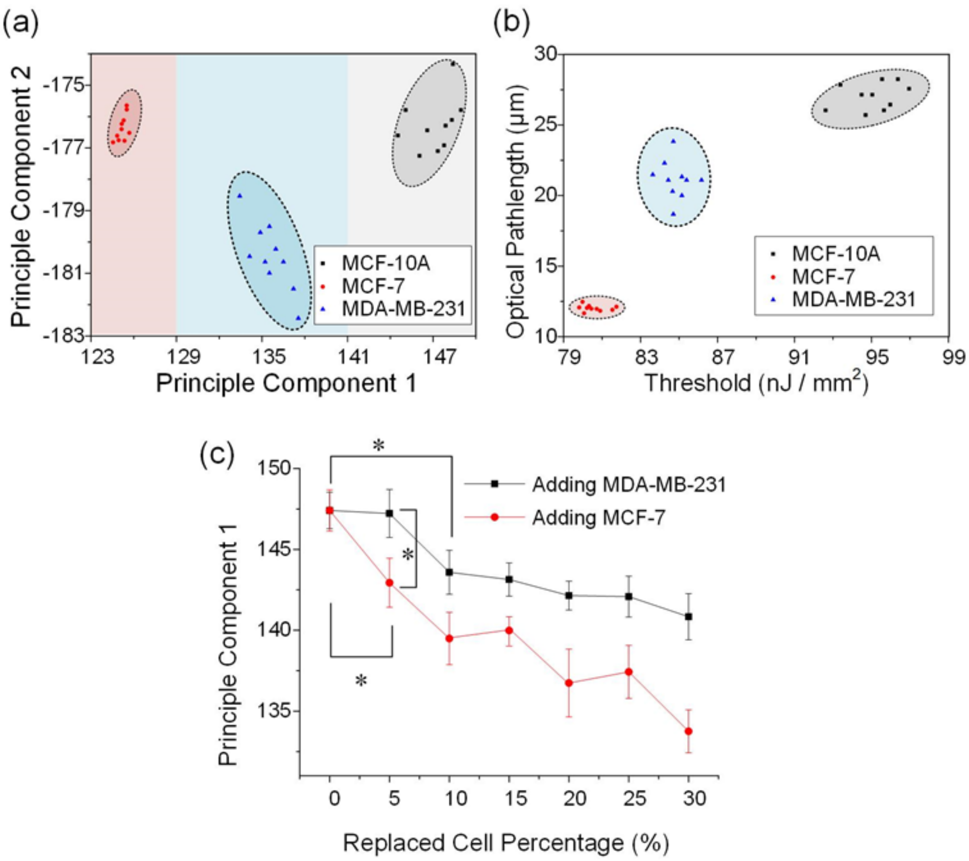

Figure 4.15 Cell classification and cancer cell detection. (a) principle component analysis for cell type classification (10 measurements for each cell type). The principle component 1 is the first-order component, which equals $0.68 \times \text{threshold} +$

$0.10 \times \text{peak shift} + 0.73 \times \text{optical pathlength}$, and the principle component 2 is the second order component, which equals $0.71 \times \text{threshold} - 0.37 \times \text{peak shift} - 0.60 \times \text{optical pathlength}$. Using principle component 1 could be capable of classifying the cell types, as indicated by the colored rectangular blocks. (b) cell classification by thresholds and optical pathlength. (c) Detecting cancerous cells in cell mixtures using principle component 1. 5% MCF-7 in MCF-10A could be detected and 10% MDA-MB-231 could be detected. Moreover, MCF-7 and MDA-MB-231 could be distinguished at 5% addition. * indicates statistical significance at a level of 5%.

To further validate cancerous cell detection in cell mixtures using BFRL, small amount of cancerous cells (e.g. MFC-7 and MDA-MB-231 cells) are added into MCF-10A suspensions and BFRLs are performed on the mixture suspensions. By using the principle component 1 introduced in the last paragraph, we successfully identified 5% MCF-7 in cell mixture and 10% MDA-MB-231 in cell mixture, see Figure 4.15c. Moreover, the MCF-7 and the more invasive cancer cell MDA-MB-231 could be distinguished at an addition of 5%. On the other hand, detection sensitivity by principle component 1 is much higher than using single BFRL properties such as threshold, peak wavelength and optical pathlength (see Figure 4.16). Thus, the first-order principle component derived by PCA is a good indicator for cancerous cell detection, which provides a potential strategy for RL bio-sensing.

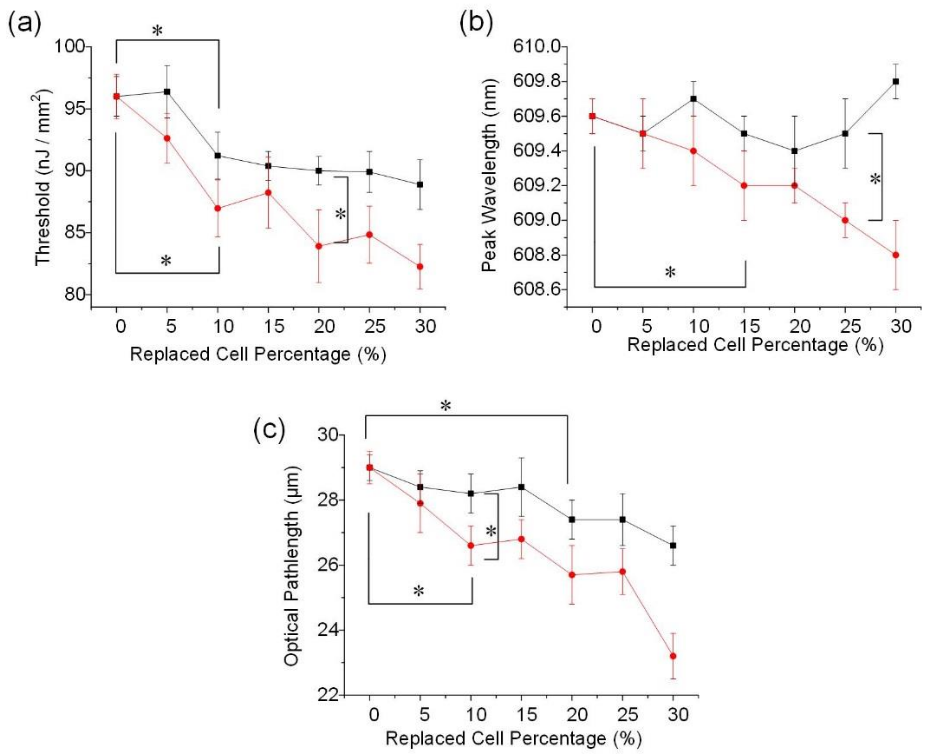

Figure 4.16 Detecting cancerous cells (MCF-7 and MDA-MB-231) in cell mixtures (in MCF-10A suspensions). (a) Using Threshold as an indicator, 10% MCF-7 in MCF-10A could be detected and 10% MDA-MB-231 could be detected. Moreover, MCF-7 and MDA-MB-231 could be distinguished at 20% addition. (b) Using the peak wavelength as an indicator, 10% MCF-7 in MCF-10A could be detected and MDA-MB-231 could not be detected up to 30%. Moreover, MCF-7 and MDA-MB-231 could be distinguished at 25% addition. (c) Using the peak wavelength as an indicator, 10% MCF-7 in MCF-10A could be detected and 20% MDA-MB-231 could be detected. Moreover, MCF-7 and MDA-MB-231 could be distinguished at 10% addition. * indicates statistic significance at a level of 5%.

4.12 Summary

In summary, a label-free RL cytometer with the sensing strategies of the different lasing properties tuned by the whole-cell as well as the subcellular biophysical properties of the single floating cells is presented in this chapter. Three key parameters were proposed in the BFRL, i.e. lasing threshold, wavelength shift and optical pathlength. The lasing threshold was demonstrated strongly relevant to the whole-cell scattering of the biofluids. On the other hand, the peak shift of the lasing spectra was strongly influenced by the subcellular structure of the cells, i.e. cortical shells and nuclear lamina shells. The PFT analysis further confirm the influence of the cellular and subcellular structure on the random lasing properties in the BFRL, leading to a sensitive and parameterized sensing strategy. By performing more measurements with different batches of microfluidic devices and cells, the repeatability and reliability of the BFRL is verified. A cell type classification strategy is introduced by adapting principle component analysis, and the first order principle component is shown a good indicator for detecting cancerous cells in cell mixtures. This work extends the biological RL system to integrate with optofluidic devices and reveals the possibility of the random-laser-based cytometer, which opens a new way for cancerous cell diagnostic using random laser.

Chapter 5 Double Plasmon Resonance Reduced Threshold of Two-photon Random Lasing in All-inorganic Perovskite Quantum Dots for Speckle-free Imaging

5.1 Introduction

As mentioned in Chapter 2, the RL is a promising class of light sources in the real-time full-field imaging applications. Several pioneering studies have demonstrated the use of one-photon-pumped RLs to achieve speckle-free imaging, and in those RLs fluorescence dyes as gain media are simply mixed with disordered structures as random cavities. These RLs often work under pumping at about 500 nm and emit frequency down-converted lights. Up to date, no frequency up-converted (two or multi-photon pumped) RL has been demonstrated for imaging applications. This might be due to the fact RLs generally work at much higher thresholds than conventional CW lasers because of their “mirrorless” feature. When it comes to frequency up-converted random lasing, the required threshold power density is even higher because both multiphoton excitation and emission efficiencies are intrinsically lower than that of their one-photon counterparts. Therefore, it is urgent to design a new kind of RLs device which can realize upconversion lasing at a lowered threshold in order to significantly expand the practical applications of RLs, such as speckle-free bio-imaging.[147] To this end, selecting a gain material with outstanding optical properties is the key to achieving low-threshold frequency up-converted RLs.

In the past few years, perovskite metal halide quantum dots have emerged as an outstanding family of materials for various optoelectronic applications in the fields of light-emitting diodes[148], ASE devices,[149] and optically pumped lasers.[150,151] These applications benefit from many exotic properties of perovskite quantum dots (PQDs), such as prolonged carrier diffusion length, high photoluminescence (PL) efficiency and large multi-photon absorption cross section etc.[152] Notably, compared with II-VI semiconductor QDs, both ASE and lasing processes from PQDs occur at much lower thresholds under both one-photon and multiphoton pumping.[150,153,154] For instance, the two-photon pumping threshold of an inorganic PQD-based laser is a twentieth of that of traditional semiconductor QD-based lasers such as CdSe/ZnS QDs.[154]

Considering the lowered lasing threshold of PQD-based lasers and the stringent requirement of random lasing, it is reasonable to expect that PQDs be a promising class of gain medium for achieving multi-photon-pumped low-threshold random lasing. In 2014, Dhanker *et al.* observed, for the first time, random lasing in a methylammonium lead iodide perovskite planar microcrystal network,[155] thereafter followed with several reports in various PQD-based disordered systems.[156] For example, Wang and co-workers demonstrated a one-photon-pumped RL consisting of amino-mediated anchoring halide PQDs onto an array of monodispersed silica spheres. Yet, it has remained a great challenge in realizing low-threshold PQD-based random lasing under multiphoton pumping at room temperature due to the high lasing threshold. To the best of our knowledge, two-photon-pumped PQD-based random lasing has only been demonstrated in the liquid nitrogen environment.[156]

To reduce the RL threshold, one effective strategy is embedding noble metal nanoparticles into the optical gain materials to form plasmon-assisted disorder nanostructures.[131] In these systems, plasmonic nanoparticles not only work as light scattering centers, but also generate near-field "hot spots", thereby providing strong local electric field enhancements and consequently improving the transition rates of the surrounding gain materials. By overlapping the localized surface plasmon resonance (LSPR) band of the metal nanoparticles and the emission frequency of the gain medium, the pump thresholds of plasmonic RLs reduce significantly.[157] Inspired by my earlier demonstration of plasmonic dual-enhancement of upconversion emission in lanthanide-doped nanocrystals[158], in this chapter, I introduce the double-plasmon-resonance enhancement mechanism to simultaneously promote the absorption and emission rates of the PQDs in order to achieve remarkably low-threshold RL. In this design, double-resonant gold nanorods (GNRs) are embed into a thin film of well-dispersed all-inorganic $CsPbBr_3$ PQDs at controlled density, and the two GNR LSPR bands are delicately tuned to spectrally match the two-photon excitation and emission frequencies of the PQDs. With increasing the density of the embedded GNRs, an intriguing four-stage emission evolution from the hybrid device was observed, namely, ASE (for a pristine film of $CsPbBr_3$ PQDs), incoherent and coherent random lasing, and plasmon-enhanced ASE, accompanied with a monotonic decrease in the threshold value for achieving population inversion in each stage. In particular, the coherent RL threshold is only fiftieth of that for the two-photon RL made of a thin film of ZnO nanocrystals,[147] and is also significantly lower than that recently reported from a PQDs-based two-photon micro-cavity laser.[154] More importantly, it was found that the coherent RL radiation has the lowest speckle contrast in imaging formation among the other three two-photon-induced emissions and a commercial CW laser. To the best of our knowledge, this is the first demonstration of using plasmonic double-resonance effect to achieve low-threshold two-photon PQDs-based RL at room temperature, which would significantly promote the research of multi-photon RLs and their applications potentially in real time, full-field imaging and projection applications (e.g. bio-imaging).

5.2 Sample preparation and characterization

5.2.1 Chemicals

Tetrachloroauric acid ($HAuCl_4{\cdot}3H_2O$), sodium borohydride ($NaBH_4$), cetyltrimethylammonium bromide (CTAB), ascorbic acid (AA), silver nitrate ($AgNO_3$), hydrochloric acid (HCl), cesium bromide (CsBr), Lead bromide ($PbBr_2$), N, N-Dimethylformamide (DMF), Oleic acid (OA), Oleylamine (OAm), toluene, are bought from Aladdin and used without further purification.

5.2.2 Morphology characterization

TEM images are captured with a JEM-2100F field-emission electron microscope and JEM-2011 Transmission Electron Microscope. SEM images are captured with a JEOL Field Emission SEM. AFM images are obtained with a NTMDT. Absorption spectra were obtained with a Shimadzu UV2550 spectrophotometer. X-ray diffraction (XRD) pattern was measured with a Bruker AXS D2 phaser X-ray diffractometer equipped with a Cu Kα radiation source (λ=1.5418 Å) at 40 kV and 30 mA.

5.2.3 Synthesis of $CsPbBr_3$ QDs

$CsPbBr_3$ QDs were synthesized by a hot-injection method. A mixture of 0.267 g Cs_2CO_3, 0.833 mL of oleic acid (OA), and 10 mL of octadecene (ODE) was degassed under argon flow in a 50 mL four-neck flask at 130 °C for 10 min. Then the reaction was kept at 150 °C for another 10 min until all the Cs_2CO_3 have reacted with OA. After cooling to room temperature naturally, the Cs-precursor was kept in a glove box. ODE (10 mL), OA (1 mL), oleylamine (OAm, 1 mL), and 0.36 mmol of $PbBr_2$ were mixed and degassed under N_2 at 130 °C for 1 h. After complete dissolution of $PbBr_2$ salts, the temperature was raised to 160 °C and kept for another 10 min. Then, 1 mL of the Cs-precursor was swiftly injected into above hot mixture and the reaction was stopped with ice bath after 5 s. The nanocrystals were precipitated by adding excess acetone and washed with a solvent combination of toluene and acetone by centrifugation. The TEM and high-resolution STEM images of the as-prepared PQDs are shown in Figure 5.1.

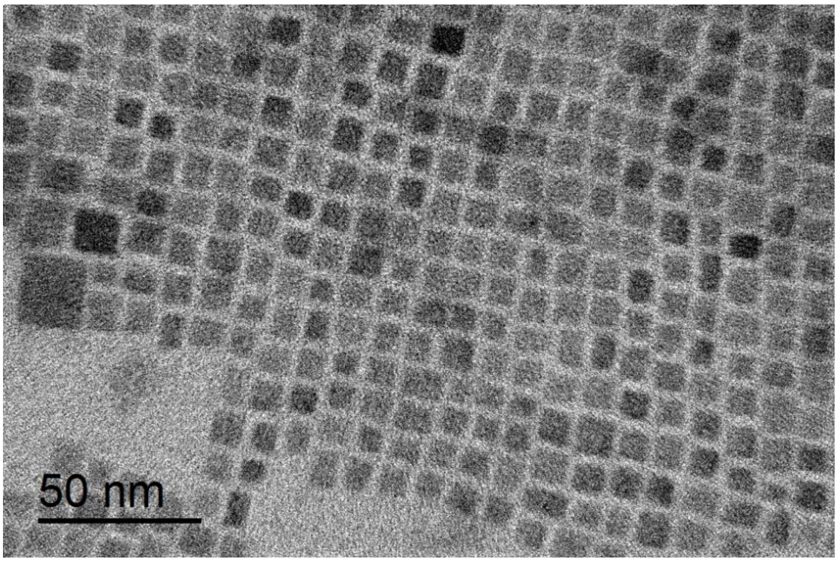

Figure 5.1 TEM image of $CsPbBr_3$ QDs. The scale bars in both images are 50 nm.

The PQDs are in cubic phase with a lattice constant of ~0.56 nm. The average edge length of the PQDs is determined to be 8.0±0.3 nm, as shown in Figure 5.2.

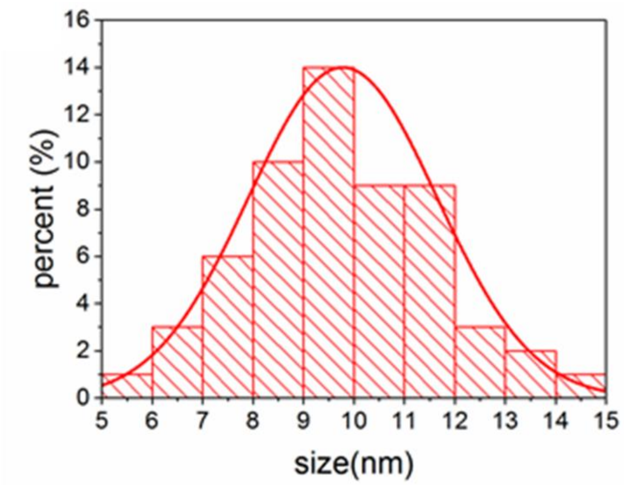

Figure 5.2 Size distribution of $CsPbBr_3$ quantum dots.

The XRD spectrum in Figure 5.3 further verifies that the PQDs crystallize in the cubic phase (a = 5.605 Å, space group Pm$\bar{3}$m, PDF75-0412).[159,160]

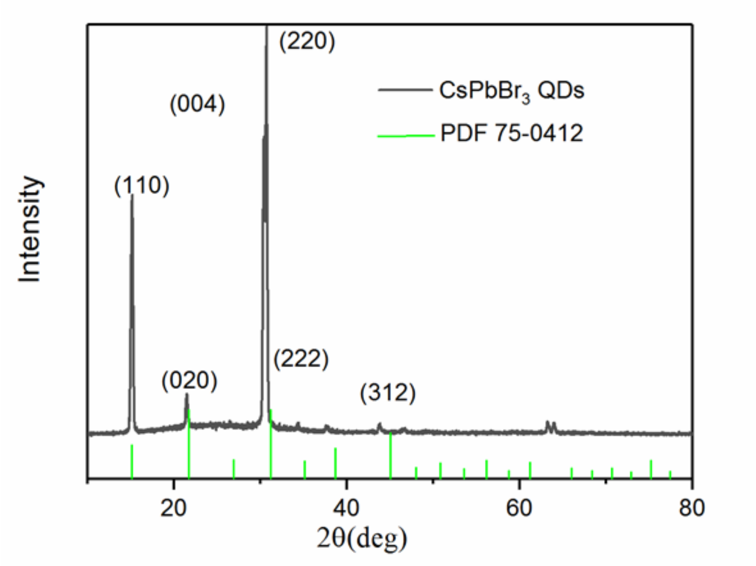

Figure 5.3 The XRD spectrum of $CsPbBr_3$ QDs, the green line is the reference PDF 75-0412.

5.2.4 Synthesis of GNRs

GNRs were synthesized using a seed-mediated methods.[161] The seed solution was prepared by mixing $HAuCl_4$ (0.01 M, 0.25 ml) with CTAB solution (0.1 M, 9.25ml), and then freshly ice-cooled $NaBH_4$ (0.01 M, 0.6 ml) were injected quickly. The brown yellow seed solution was kept at room temperature for 2-5 h for use. Next $HAuCl_4$ (0.01 M, 2 ml), $AgNO_3$ (0.01 M, 0.4 ml), AA (0.1M, 0.32 ml), HCl (1 M, 0.8 ml) were mixed in 42.5 ml CTAB (0.1 M) to form a growth solution. Finally, the growth was initiated by adding 96 μl seed solution in the growth solution, and the solution was left at room temperature overnight. The GNRs were centrifuged and dispersed in 50 ml DI water again. Figure 5.4 shows the TEM image of as-prepared GNRs. Their average length and width are ~18 and ~70 nm, respectively, as revealed from the statistics in Figure 5.5.

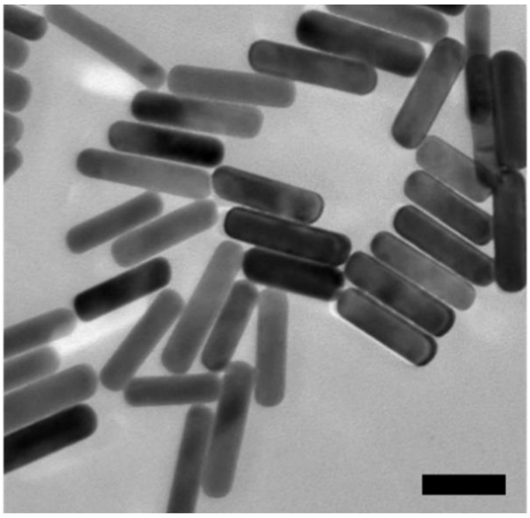

Figure 5.4 TEM image of the GNRs. The scale bars in both images are 50 nm.

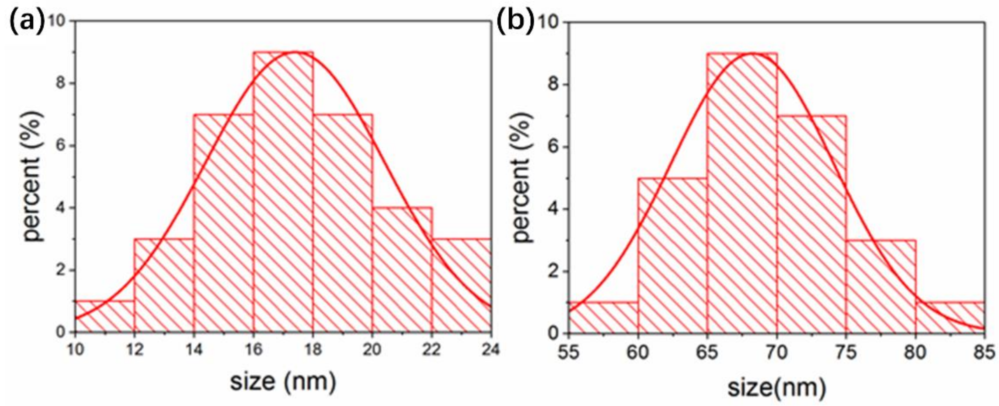

Figure 5.5 (a) Diameter and (b) length distribution of the GNRs.

5.2.5 Design strategy of a plasmonic perovskite hybrid system

The extinction spectrum of the as-prepared GNRs in Figure 5.6 shows two pronounced LSPR modes: a long-wavelength longitudinal mode and a short-wavelength transverse mode, as confirmed by the simulated electric near-field intensity distribution profiles in Figure 5.7. By precisely controlling the length-width ratio of the GNRs, the longitudinal and transverse LSPR bands can be tuned to closely match the two-photon absorption and emission wavelengths of the $CsPbBr_3$ QDs (~800 and ~522 nm, see Figure 5.6). Such spectral matching is expected to enable both plasmonic excitation and emission enhancements for the PQDs, because according to Fermi's Golden rule the transition rates for both absorption and emission are proportional to the local electric field intensity at the location of a quantum emitter at its respective absorption and emission wavelengths. The simulation results in Figure 5.7 illustrate that the maximum near-field intensity enhancement factor can reach four orders of magnitude at the two-photon excitation wavelength of 800 nm and 18 folds at the two-photon emission wavelength of 522 nm, indicating accelerated absorption and emission rates. In addition, there is a significant spatial overlapping between the electric near-field distribution profiles around the GNR tip regions at both excitation and emission wavelengths, which allows the PQDs located in these regions to benefit from both plasmonic absorption and emission enhancements. Finally, the GNRs have enhanced scattering cross-sections at the two LSPR wavelengths, which can drastically increase the scattering strength of the hybrid system and thus form potential RL cavities.

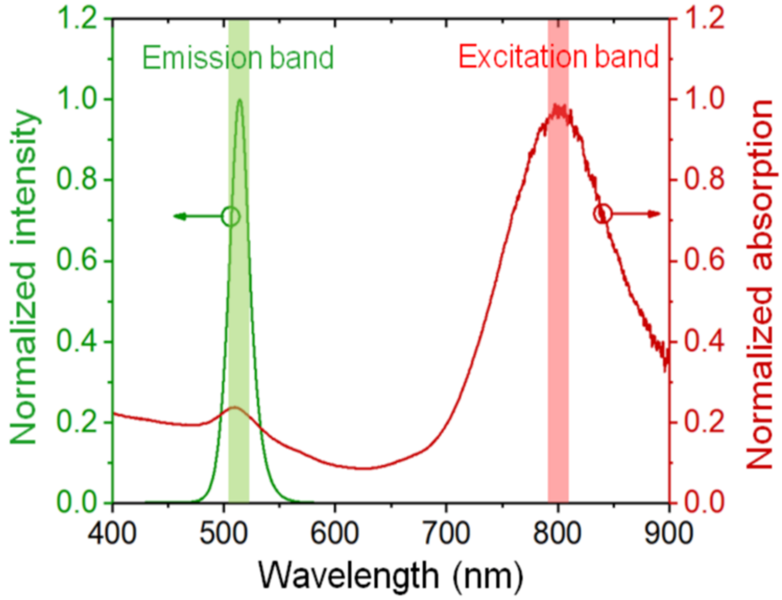

Figure 5.6 Normalized emission spectrum of the $CsPbBr_3$ QDs (green) and normalized extinction spectrum of the GNRs (red).

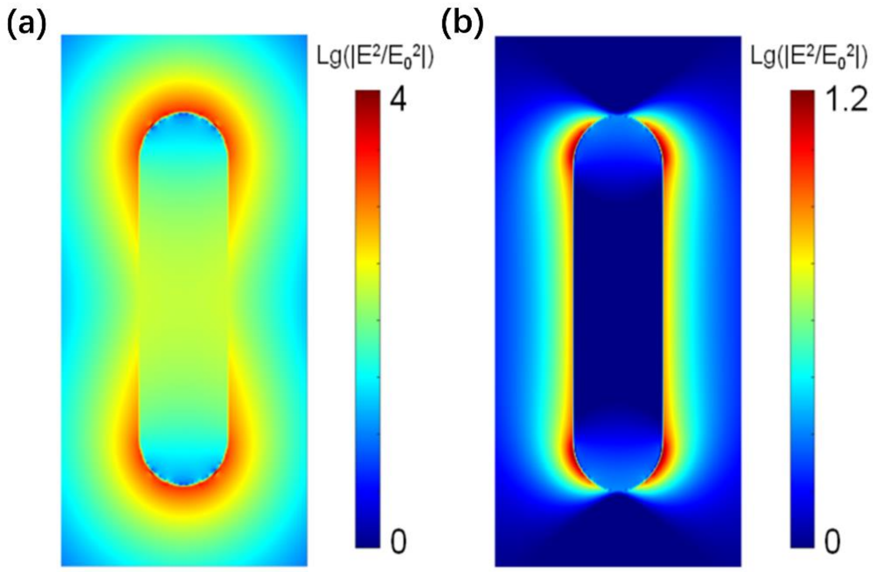

Figure 5.7 Simulated electric near-field field enhancement profiles of a GNR under excitation at (d) 800 nm and (e) 522 nm. The enhancement factors are logarithmically scaled.

5.2.6 Fabrication of plasmonic perovskite hybrid structure.

Figure 5.8 shows the fabrication procedures of the pure PQDs film (top row) and GNRs/PQDs hybrid film (bottom row), respectively. For the fabrication of GNRs/PQDs film, GNRs (with a concentration ranging from ~2 nM to 50 nM in different samples) was firstly deposited on a plasma cleaned glass substrate. By controlling the deposition time, ITO with different density of deposited GNRs are obtained. After drying, GNRs were uniformly distributed on the glass substrate and formed numerous cavities with different sizes (see SEM images in Figure 5.9). Here, five GNRs/PQDs flim samples (Sample 2-6 in Table 5.1) with GNRs density varies from 20 to 1800 particles/μm^2 were prepared to explore the plasmonic influences of GNRs on random lasing behavior. Then the pure $CsPbBr_3$ QDs in toluene solution was dropped on the top of GNRs, sealed with another glass immediately. Consequently, a GNRs/PQDs hybrid film was produced with a close-packed PQDs solid thin film on the top of GNRs. The pure PQDs film sample (Sample 1 in Table 5.1) was prepared in the similar way with no GNRs deposited before.

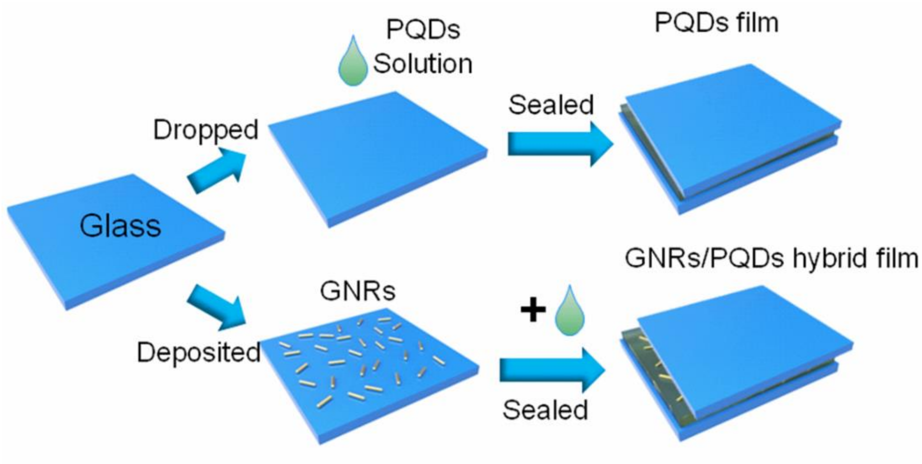

Figure 5.8 Schematic of the fabrication process of pure PQDs film (top row) and GNRs/PQDs hybrid film (bottom row)

Table 5.1 The porperties of the pure PQD film and the GNRs/PQDs hybrid film samples

	GNRs densitys (particles/μm^2)	Lifetime (ns)	Emission Behavior	Threshold (mj·cm^{-2})	Quality
Sample 1	0	8.45	ASE	1.79	153.9
Sample 2	20	7.14	ASE	1.45	162.3
Sample 3	80	7.08	incoherent RL	0.873	154.0
Sample 4	100	6.36	incoherent RL	0.818	114.3
Sample 5	170	5.52	coherent RL	0.68	1782.3
Sample 6	1800	5.48	ASE	0.622	144.4

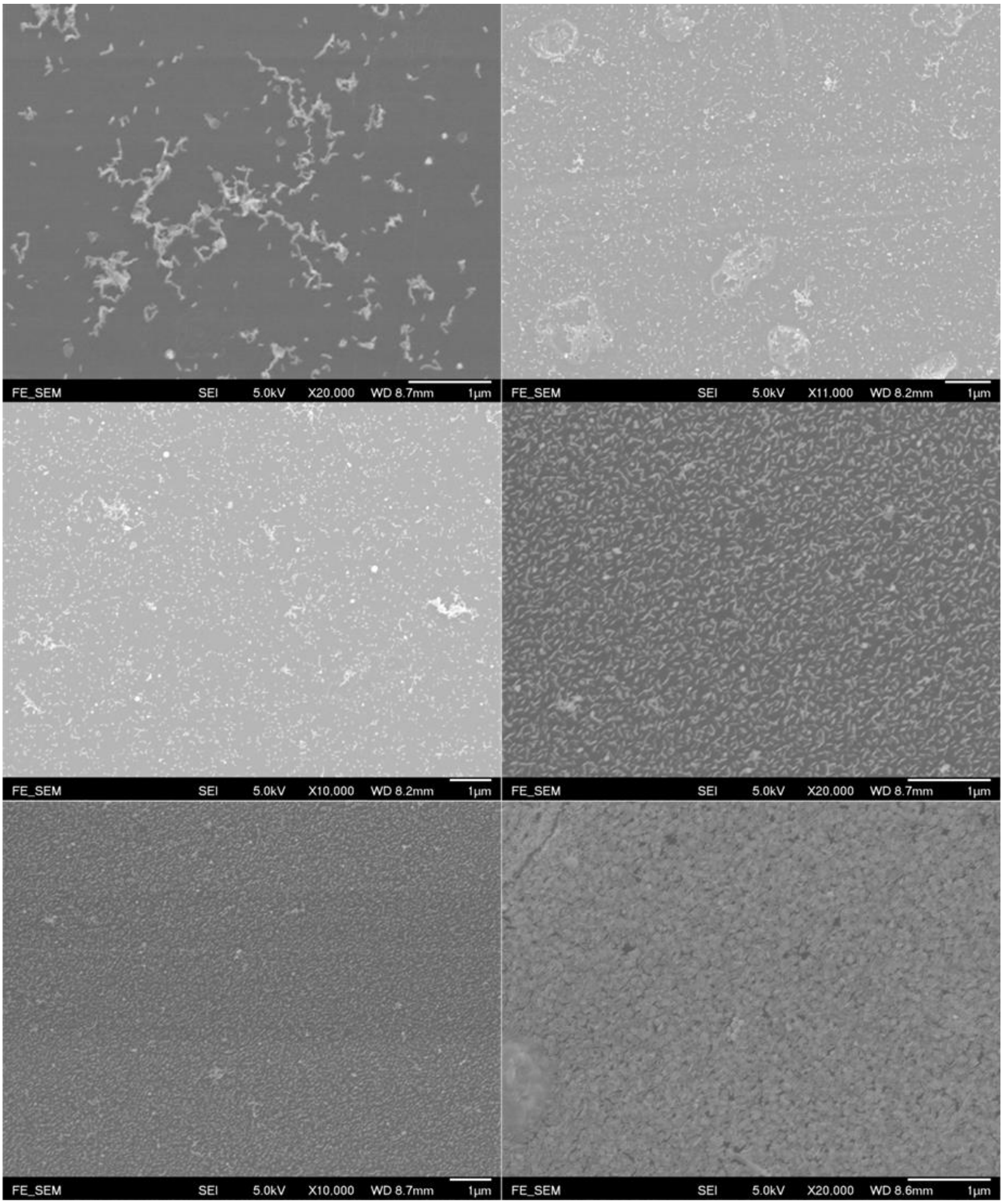

Figure 5.9 SEM images of random distributed GNRs with different density (sample 2-6).

5.3 Emission and random lasing measurement

5.3.1 Emission properties of the pure $CsPbBr_3$ QDs solution

The nonlinear absorption and emission properties of the pure $CsPbBr_3$ QDs solution was firstly investigated under the pumping of an 800 nm femtosecond pulse laser (Libra Coherent, 1 kHz, 50 fs). Figure 5.10 shows the PL spectra of $CsPbBr_3$ QDs solution at different pump power, which display a board spontaneous emission located at ~522 nm. Since the liner absorption is negligible from wavelength longer than~520 nm of $CsPbBr_3$ QDs, correspondingly to the bandgap 2.38 eV, as shown in Figure 5.11. The photon energy of 800 nm near-infrared light is far below the bandgap of perovskites, indicating a multiphoton absorption of $CsPbBr_3$ QDs. The dependence of the peak intensity and full width at half maximum (FWHM) on the pump power was extracted from the PL spectra and shown in Figure 5.10b. With the pump power increased, the PL intensity increased linearly. However, the FWHM always keeps at ~18 nm. A clearly quadratic dependence of peak intensity on the pump power was observed, which confirms the two-photon absorption at 800 nm.[153]

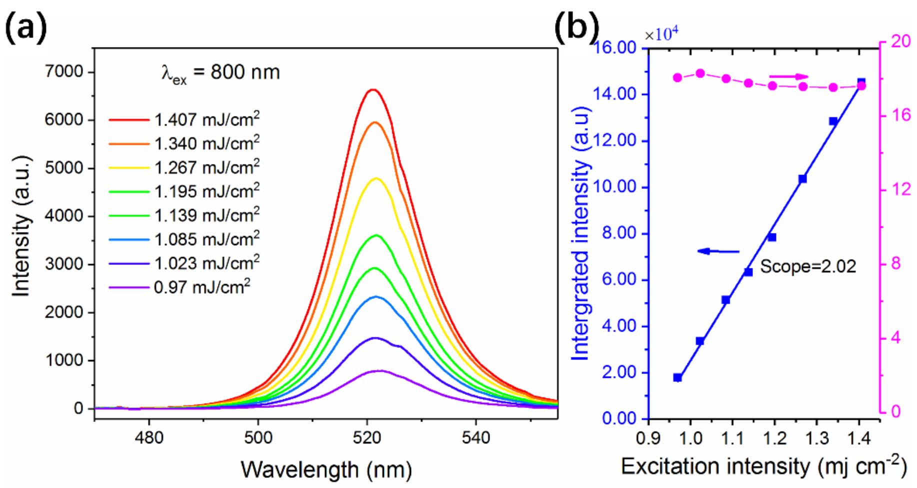

Figure 5.10 (a) The PL spectra of the PQDs solution excited by an 800 nm fs laser with different pump power. (b) The integral PL intensity (blue square) and FWHM (purple circle) of the main peak from the PQDs solution as a function of the pump power.

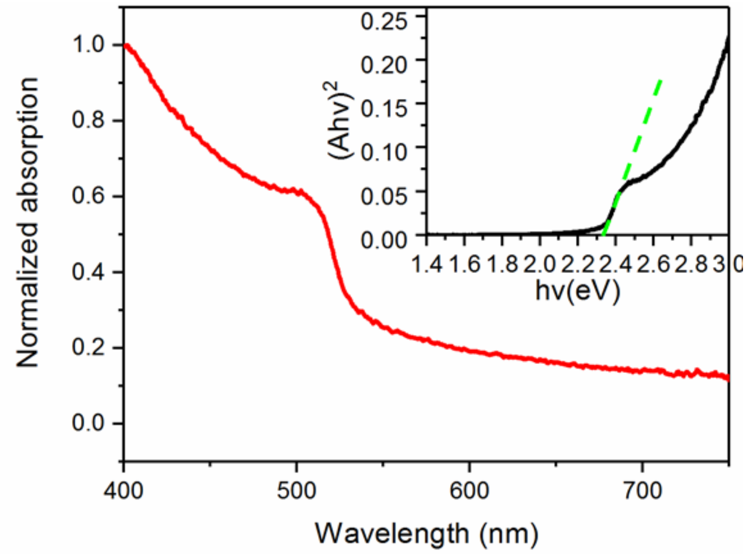

Figure 5.11 Absorption and bandgap of CsPbBr3 quantum dots in toluene solution.

5.3.2 Z-scan measurement

To further investigate the nonlinearly absorption coefficients of PQDs, the open aperture (OA) Z-Scan technique was used (Figure 5.12).[162] The normalized transmittance can be written as

$$T_{open}(z) = 1 - \frac{q_0}{\sqrt{8}\left[1 + \left(\frac{z}{z_0}\right)^2\right]} \tag{5.1}$$

Where $q_0 = \beta I_0 L_{eff}$ and $L_{eff} = (1 - e^{-\alpha L})/\alpha$. L is the thickness of the sample,α is the linear absorption coefficient, $Z_0 = {\pi\omega_0^2}/{\lambda}$, where ω_0 is the radius of the beam waist, and I_0 is the light intensity at the focal point. By fitting the OA data with the equation one can deduce the nonlinear absorption coefficient β, which is $4.8\times e^{-11}$ m W^{-1}.

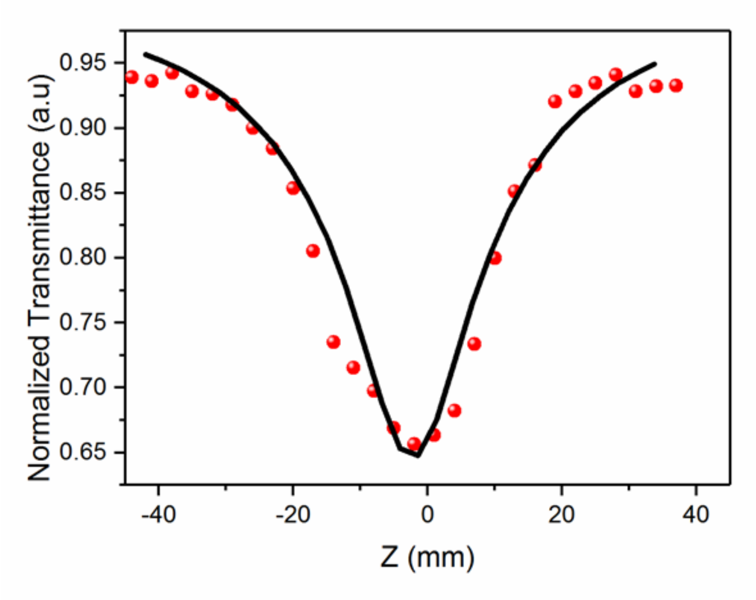

Figure 5.12 The open aperture z-scan curve measured on the $CsPbBr_3$ QDs film.

This absorption coefficients is 1–2 orders of magnitude larger than those of traditional QDs,[163,164] revealing that PQDs are excellent nonlinear optical materials. In the process of two-photon absorption, an electron simultaneously absorbs two photons to reach the excited state that corresponds to the sum of the energy of the two incident photons. Via a “virtual state”, the excited electron relaxes to the ground state and emit a frequency up-converted photon, as shown in the Jablonski diagram in Figure 5.13.

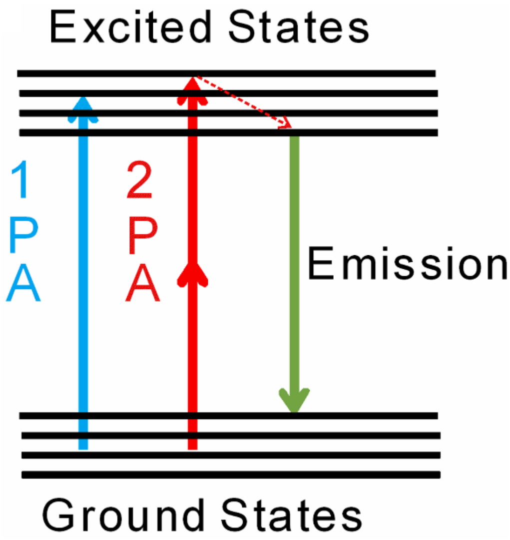

Figure 5.13 Jablonski diagram of light absorption and emission in PQDs.

5.3.3 Lifetime measurement

The evidence of plasmonic effect on the emission process of the PQDs can be verified by analyzing the lifetime of the PQDs. Figure 5.14 shows the PL decay curves of the pure PQDs film and GNRs/PQDs film. The decay curves can be well fitted by a two-exponential-decay function $I(t) = I_0 + A_1 \exp\left(-\frac{t}{\tau_1}\right) + A_2 \exp\left(-\frac{t}{\tau_2}\right)$, where τ_1 and τ_2 represent the lifetime of radiative recombination and non-radiative recombination, respectively, and the total lifetime is $\tau = (A_1\tau_1{}^2 + A_2\tau_2{}^2)/(A_1\tau_1 + A_2\tau_2)$. The lifetimes of the as-prepared samples with different GNRs density are listed in Table 5.1 and 5.2. The lifetime of pure PQDs film is calculated to be 8.45 ns. Whereas, with the density of GNRs increased, the lifetime of the GNRs/PQDs hybrid films decreased from 7.14 ns to 5.48 ns. The reduction of the PL lifetime is conceived as a strong evidence of the interaction between excitons of the $CsPbBr_3$ QDs and the LSPRs of the GNRs. Because the plasmonic effect will introduce new radiative and non-radiative decay channels to the nearby PQDs. Such plasmon-introduced rapid recombination channels will alleviate the impact of nonradiative centers on the stimulated emission actions, which is the main mechanism for reducing the lasing threshold.[165]

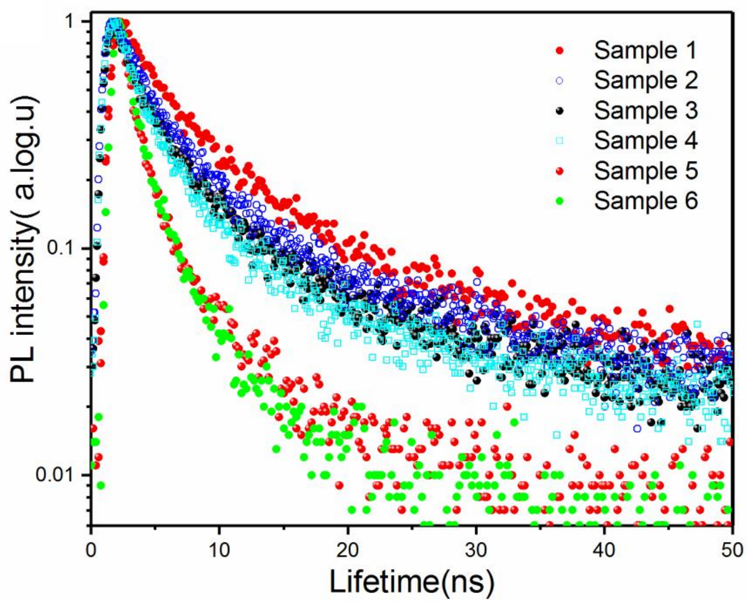

Figure 5.14 PL decay curves of the pure PQDs film (green triangle) and GNRs/PQDs hybrid film (blue triangle). The corresponding solid lines are the two-exponential fitting curves.

Table 5.2 Fitting data of the Lifetime

	A_1	τ_1	A_2	τ_2	τ
Sample1	0.34	11.33	0.66	3.24	8.45
Sample2	0.38	8.63	0.62	1.34	7.14
Sample3	0.33	9.44	0.67	2.30	7.08
Sample4	0.38	8.02	0.62	1.78	6.36
Sample5	0.44	6.63	0.56	1.43	5.52
Sample6	0.27	7.76	0.73	1.82	5.48

5.3.4 Measurement set-up for film samples

To investigate the emission properties of the film samples, a stripe pump configuration was carried out, as shown in Figure 5.15. The laser beam of the pump source was focused into a stripe spot (100 μm × 5 mm) by a cylindrical lens. The strip spot is slight titled on the film sample and close to the edge, so that the pumped region can form a waveguide structure guiding the light to emit out from edge of the samples. Then the emission spectra were collected by a multimode optical fiber and measured by a spectrometer (Princeton Spectra Pro 2750) equipped with a thermoelectrically cooled CCD (ProEM EM, resolution: 0.1 nm).

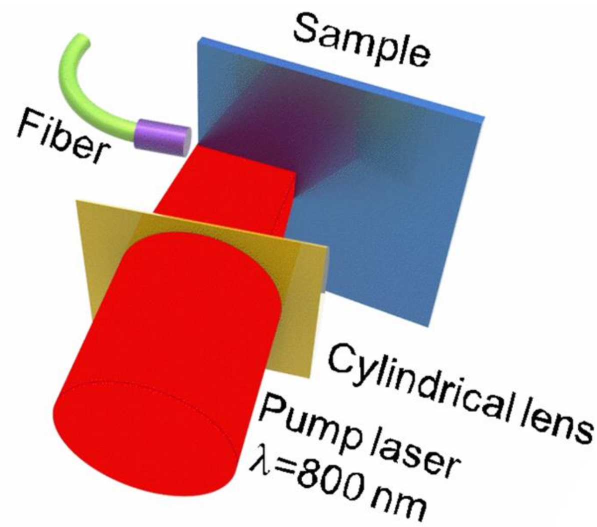

Figure 5.15 Schematic of pump and collection configuration.

5.3.5 Emission in pure PQDs film (Sample 1)

Figure 5.16 shows the emission spectra from the pure PQDs film at different pump power. Under low pump power ($<\sim$1.56 mJ·cm^{-2}), the emission spectra are dominated by the relatively broad spontaneous emission located at 528 nm (FWHM ≈ 18.5 nm). When the pump power exceeds ~1.79 mJ·cm^{-2}, a clear ASE with the evidence of a much narrower peak (FWHM≈5 nm) has emerged. The ASE peak is red-shifted by ~8 nm with respect to the center of PL, conforming to the positive bi-exciton gain stimulated emission of $CsPbBr_3$ QDs. Above the ASE threshold, the integral peak intensity of ASE increases linearly as the pump power increases. The PL results means that the lasing phenomena cannot be observed in the pure $CsPbBr_3$ QDs film.

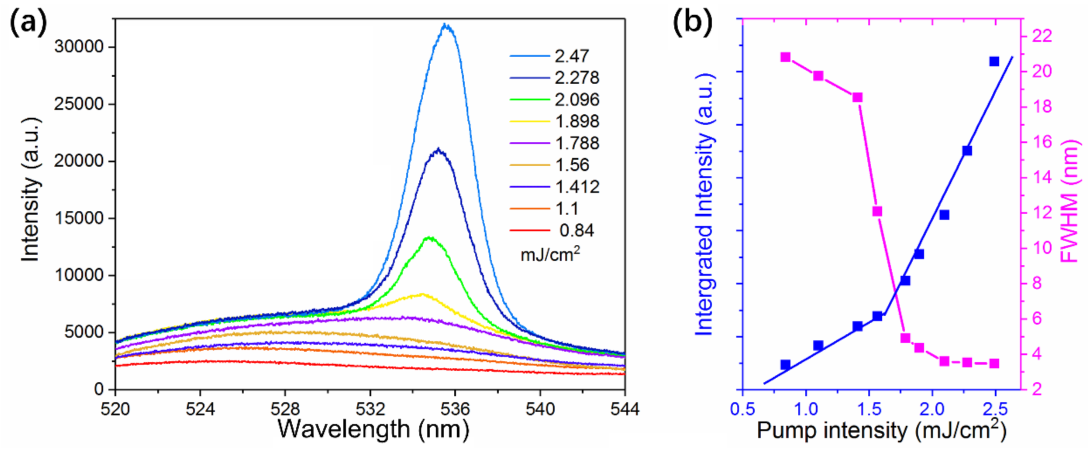

Figure 5.16 (a) PL intensity of the pure PQDs film, and integral PL intensity (blue square) and FWHM (purple circle) of the main peak from PQDs film as a function of the pump power.

5.3.6 Emission in GNRs/PQDs hybrid films (Sample 2-6)

We measured the emission spectra of the GNRs/PQDs hybrid films with different GNRs density (Sample details are in Table 5.1) to explore the plasmonic influence on the emission properties. Figure 5.17a-b shows the emission spectra of the sample 3 at different pump power. At low pump power, the emission spectra exhibits similar spectral profile with the pure PQDs film, only a board spontaneous emission dominates the spectra. When the pump power increased to be above a threshold value (~0.873 $mJ{\cdot}cm^{-2}$), a drastic spectral narrowing occurred and the linewith collapsed to ~3.5 nm. Simultaneously, the peak intensity shows a significant increasment. Different with the ASE oberved in pure PQDs film, there are some small protrusions on the top of the main emission peak but these are far less pronounced than a lasing generated by resonant cavities. This feature is the fundmental evidence of the incoherent radom lasing.[80,166] Conclusively, an incoherent plasmon-enhanced PQDs RL (PPQDRL) is realized based on the GNRs/PQDs hybrid film with low GNRs density. This RL exhibits incoherent feature because the density of the GNR is too low to form resoant laser cavities with closed light path loop and the RL system is operated in a so-called weakly scattering regime. Only non-resonant optical feedback can be provided in this RL.[167]

Next, the GNR density is increased to ~170 partilces/μm^2 and the corresponding GNRs/PQDshybrid film (Sample 5) are examined. Figure 5.17c shows the collected emission spectra from this sample at different pump power. When the pump power is low, again the emission spectra only display a broad PL peak. However, as the pump power exceeds 0.68 $mJ \cdot cm^{-2}$, a distinct interference feature (spikes) gradually emerged on the top of the emission spectra. The average FWHM of the spikes is ~0.5 nm, much narrower than the FWHM of ASE and incoherent RL. As the pump power increased further, unlike the ASE of pure PQDs film, the wavelengths and intensities of the spikes varied from spectrum to spectrum. Such spikes feature and stochastic spectra variation were the definite evidence of random lasing with the coherent optical feedback, which means the coherent RL has been demonstrated based on Sample 5. It is noteworthy that the threshold of this coherent PPQDRL is 0.68 $mJ \cdot cm^{-2}$ according to the integrated PL intensity and FWHM behavior versus pump power, which is significantly lower than the threshold values in the pure PQD film and incoherent RL. This value is also significantly lower than the threshold of $CsPbBr_3$ QDs WGM laser previously reported.[154]

Interestingly, when more GNRs were deposited and assembled on the glass (Sample 6), only ASE appeared although the threshold reduced further compared with the cases of random lasing (Figure 5.17e and f). Under such high GNRs density, the GNRs have assembled a monolayer on the glass, working as a gold film and suppling the surface plasma polaritons to enhance the absorption and emission of the PQDs film.[168,169] There is no internal space between GNRs to form random lasing cavities for the emission oscillation. Therefore, even though the threshold of the two-photon ASE has decreased dramatically due to the plasmonic effect, such plasmon-enhanced ASE cannot be devoted to random lasing with much narrower FWHM. Another two samples (sample 2 and sample 6) are also measured. The results are shown in Figure 5.18

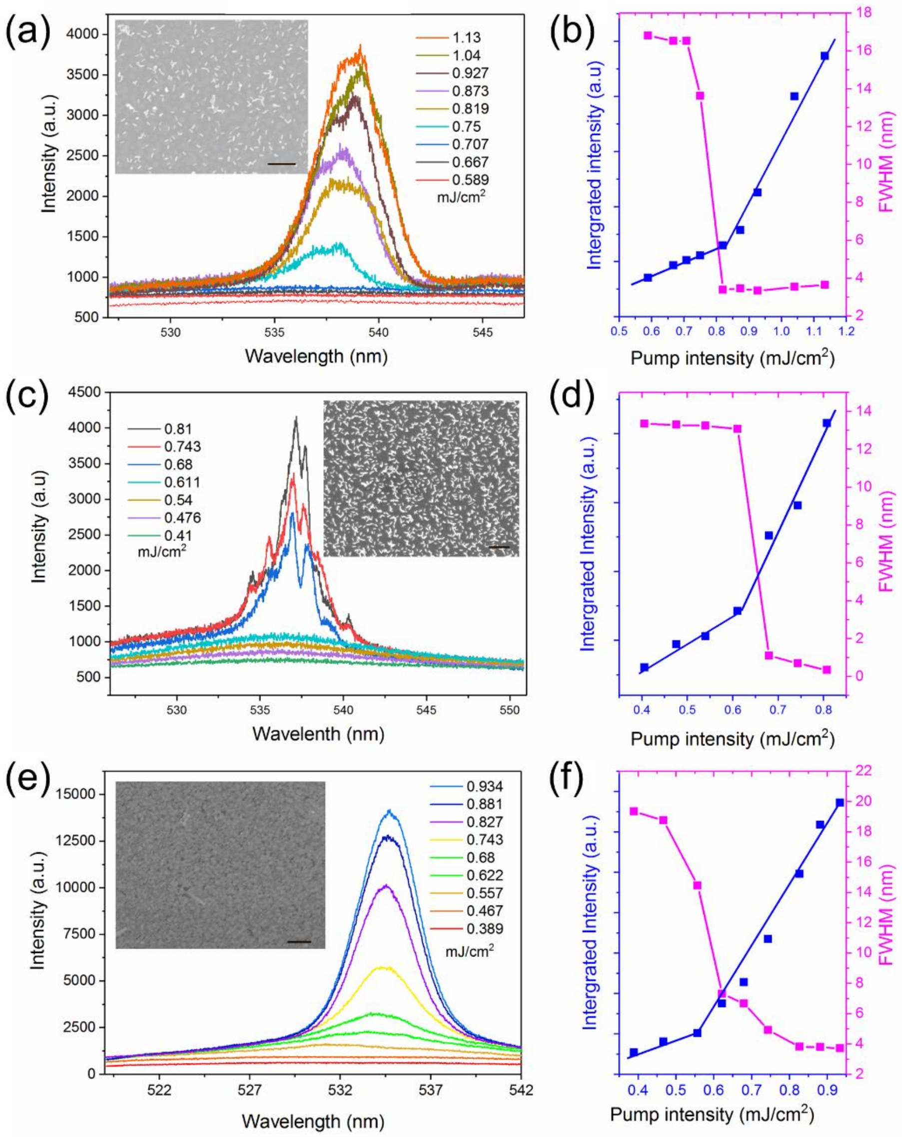

Figure 5.17 (a-b) Incoherent lasing spectra, integrated PL intensity and FWHM behavior of incoherent PPQDRL (Sample 3) with the pump power increased. (c-d) Coherent lasing spectra, integrated PL intensity and FWHM behavior of incoherent PPQDRL (Sample 5) with the pump power increased. (e-f) plasmon-enhanced ASE spectrabehavior, integrated PL intensity and FWHM behavior of GNRs/PQDs hybrid films (Sample 6) with the pump power increased.

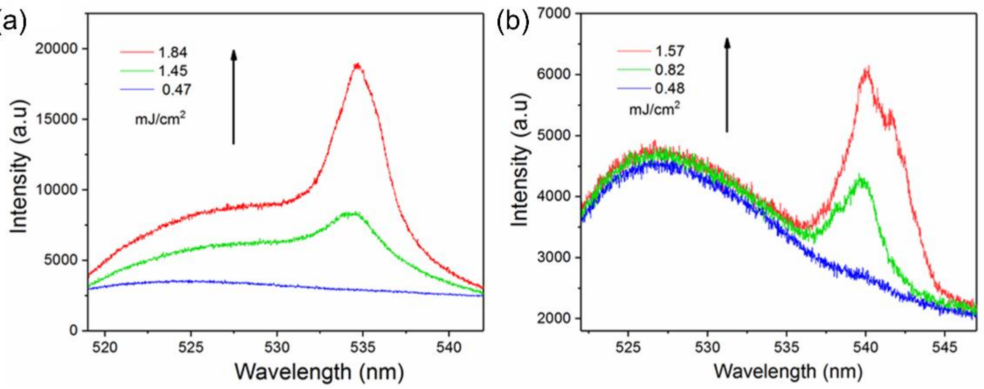

Figure 5.18 (a) ASE of samples 2 with gold nanorods density 20 particles/μm^2 (b) incoherent RL of sample 4 with gold nanorods density 100 particles/μm^2

5.4 Random lasing mechanism in the GNRs/PQDs hybrid system

To clarify the generation of the incoherent and coherent RL, the random lasing mechanism is concluded and illuminated in Figure 5.19. The PQDs under the strip shape pump region were firstly excited and generate spontaneous emission. Part of the emission light propagating in the unpumped region will dissipate quickly due to the absorption loss. The rest of the emission light inside the pump region will continuously experience the gain as the light propagation path increases. Meanwhile, the GNRs will promote the generation of random lasing in three ways. First, the GNRs can highly increase the local electrical field due to the longitudinal LSPR effect, which enhance the excitation rate of the nearby PQDs and boost the population inversion. Second, due to the coupling between the transverse LSPR of the GNRs and the emission of the PQDs, the radiative decay rate of the PQDs will be considerably increased, resulting in enhanced emission efficiency. Third, the GNRs work as scatter centers and form numerous laser cavities for the random lasing. But, when the GNRs density is low, the PPQDRL (Sample 3 and 4) is a weakly scattering system and does not contain strongly localized cavity (i.e. closed light path loop). Only non-resonat optical feedback could be achieved. Due to the loss of enough resonant feedback, the spectrum tends to be continous. With an increase of pumping intensity, the emission spectrum narrows continuously towards the centre of the amplification line. When the GNRs density increased (Sample 5), the amount of optical scattering increased, the closed optical cavities can be formed and provid resonant feedback. Consequently, coherent random lasing behavior occurs. The experimental results show that the PPQDRL with incoherent or coherent feedback has been successfully demonstrated with the assistant of the plasmonic effect of the GNRs.

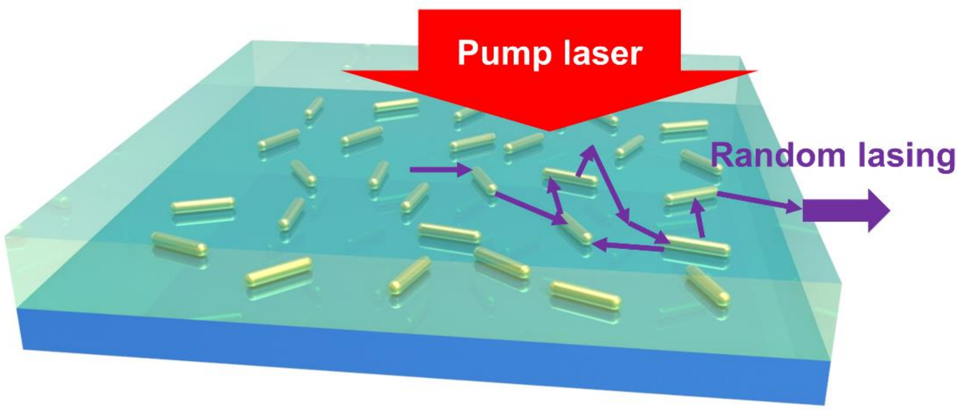

Figure 5.19 Schematic of the lasing mechanism of the PPQDRL.

5.5 Simulation

To further verify the lasing dynamic in the incoherent and coherent PPQDRL, COMSOL Multiphysics, a commercial software using Finite Element Method, was employed to calculate the lasing modes in PPQDRLs. The passive simulation model was performed (with random distributed GNRs in a two-dimensional surface) in the frequency domain and calculated the quasi-modes with a wavelength located in the emission spectrum of PQDs. The particle density of the GNRs is set to be around 80 and 170 particles/μm^2, respectively (corresponding to the cases of Sample 3 and Sample 5). The geometry configuration of the random distributed GNRs is generated in the MATLAB and introduced into the COMSOL. The simulation model is two-dimensional and square shape (8μm ×8μm) surrounding with four perfect matched layers, which is solved via the wave optical module. Figure 5.20a-b show the simulated lasing mode in the case of incoherent and coherent RL, respectively. It can be seen that the lasing mode in incoherent laser is not localized indicating a non-resonant feedback. While the lasing mode of coherent laser is strongly localized. This is because the large density of GNRs supports strong multiple light scattering and forms the localized lasing cavities. The size of the lasing mode of coherent RL presented in the simulation is determined to be around 15 μm. The simulation results are consistent with the experiment results.

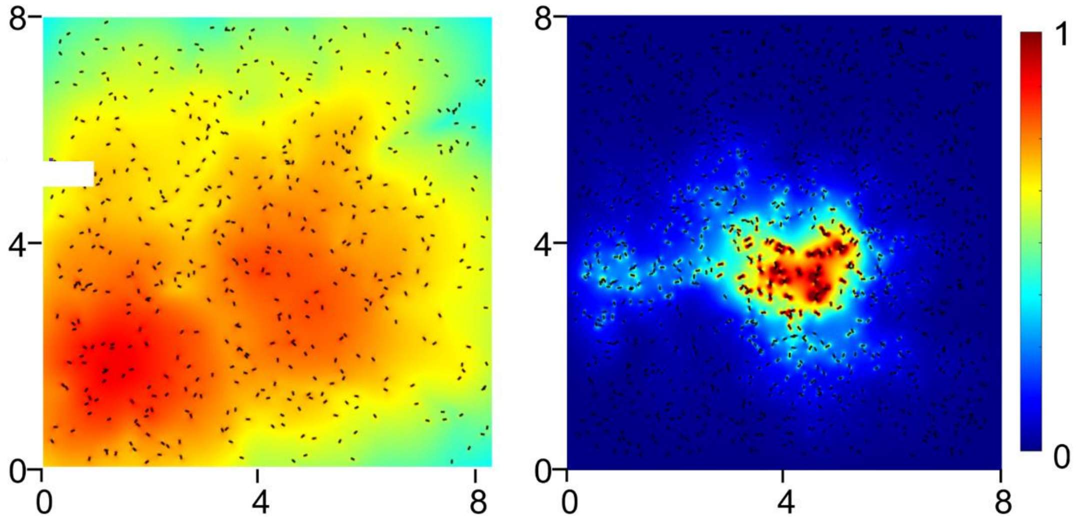

Figure 5.20 Calculated intensity distribution of lasing modes in a two-dimensional model containing random distributed GNRs with density set as (a) 80 and (b) 170 particles/μm^2, respectively.

5.6 Power Fourier transform analysis and laser cavity size in the PPQDRL

To quantify the existing cavity sizes in the PPQDRL (sample 5), the power Fourier transform (PFT) was performed to analyze random lasing spectra obtained from the coherent PPQDRL, results are shown in Figure 5.21.[165] A clear oscillation with well-separated peaks is observed from the PFT analysis result. The peaks in the PFT curve correspond to the Fourier components, d_m ,defined as $d_m = mL_c n/\pi$, where m is the order of the Fourier harmonics and n is the refraction index of the gain medium. Substituting $n = 2.3$ of $CsPbBr_3$ QDs film[170] into the above equation and the first sharp peak (fundamental Fourier component m=1) at $d_1 = 12.5\mu m$, the size of the lasing cavity inside the PPQDRL was calculated to be $L_c = 17.1\mu m$. Such cavity size is much large than the average distance between individual GNRs (Figure 5.9), indicating that the lasing cavity is formed by the scattering between several GNRs. The PFT result is in a good agreement with the numerical result for the case of coherent PPQDRL.

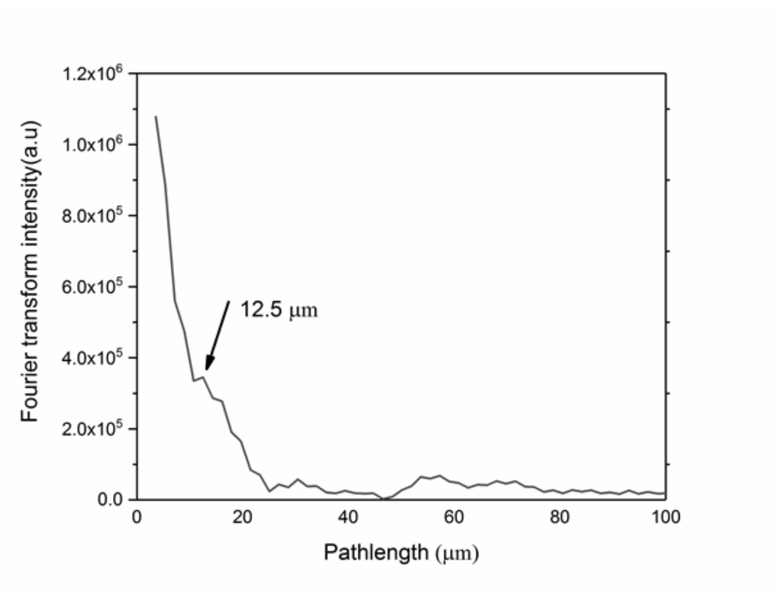

Figure 5.21 The power Fourier transform of lasing spectra from the coherent RL.

5.7 Speckle-free imaging

The most promising application for RLs is working as the light sources for the speckle-free imaging, because the RLs with low spatial coherence could prevent the formation of speckle pattern.[91] To verify the capability of the PPQDRLs for the full-field imaging, a set of optical imaging experiments were carried out. Figure 5.22 shows the experiment setup, the ASE/random lasing generated from the samples is focused by a lens onto a mask with the university logo of the Hong Kong Polytechnic University, which works as the imaging object. Then the resultant image is projected and recorded on a (CCD) camera device. A commercial 532 nm laser was also used as the light source to make a comparison.

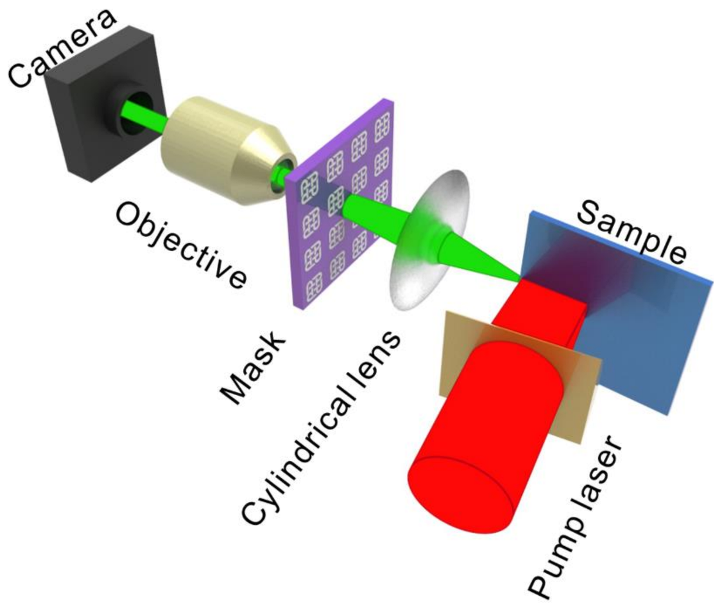

Figure 5.22 Schematic of the experimental set-up for speckle-free imaging using PPQDRL as the light sources.

The imaging results are presented in Figure 5.23. As expected, the commercial laser caused strong clear speckle pattern and blur the imaging (Figure 5.23a). This is consistent with the existing literature.[3,91] By contrast, the imaging results of the ASE (Figure 5.23b), incoherent (Figure 5.23c) and coherent random lasing (Figure 5.23d) show less interference effects and produce clean images of the objects. The imaging qualities can be quantified by the speckle contrast $C = \delta/< I >$, where δ is the ratio of the standard deviation of the intensity I and $< I >$ is the mean intensity of the speckle pattern.[3] The contrast of the incoherent RL ($C_{IncoherentRL}$=0.29) is much smaller than the that of the commercial laser (C_{Laser}0.51) and the ASE (C_{ASE}=0.344), and coherent RL has the smallest speckle contrast ($C_{CoherentRL}$=0.17). The key to achieving speckle-free imaging is to have many modes lasing simultaneously and independently to suppress the spatial coherence of total emission.[171] During the transition from ASE to incoherent RL and coherent RL, the GNRs density increased and thereby the lasing modes increased. The large amount random lasing modes enable the PPQDRL with low spatial coherence and achieving full-field speckle-free imaging.

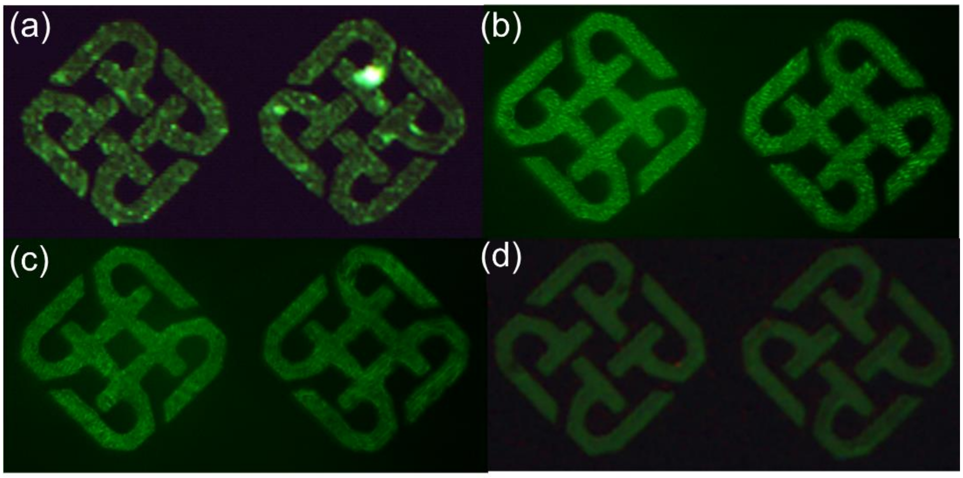

Figure 5.23 Optical images of the mask with university logo under the illumination of (a) 532 nm commercial laser and (b) ASE light source (c) incoherent RL (d) coherent RL.

5.8 Summary

In conclusion, a novel plasmon-enhanced two-photon PQDs RL by coupling the randomly distributed GNRs within PQDs film has been demonstrated. By carefully tuning the longitudinal and transverse LSPRs of the GNRs to respectively match the two-photon absorption and emission wavelength of $CsPbBr_3$ QDs, the excitation and emission efficiency of PQDs near the GNRs are enhanced. A transition from the incoherent RL to coherent RL form the GNRs/PQDs hybrid film has been observed with the density of embedded GNRs increased, rather than the ASE from pure PQDs film. But when the density of GNRs further increases until they cover the whole substrate compactly, only plasmon-enhanced ASE can be observed in this case. The RL with different spatial coherence can be easily realized at room temperature with a low threshold and exhibit better lasing performance than previous studies. Apart from detailed analyzing the laser properties of the the RL, I move forward to utilize this two-photon RL in the speckle-free imaging application as the light source. Since the wavelength of the two-photon pumping is located in the near infrared band, which feature several merits including good penetration depth and little damage to the targeted samples. We believe that the PPQDRL is a promising light source for a wide range of real time full-field imaging (e.g. bio-imaging). The plasmonic enhancement strategy proposed in this work to advance the PQDs nanolasers will benefit the development of PQDs-based photoelectric devices.

Chapter 6 Replica Symmetry Breaking in FRET-assisted Random Laser Based on Electrospun Polymer Fiber

6.1 Introduction

As mentioned in Chapter 2, wavelength-tunable RLs recently have attracted intense interest, because they show great promise for various fields, from spectroscopy to photochemistry and medicine.[172] Particularly, in the field of medicine and biology, long-wavelength (≥650 nm) lasers play an irreplaceable role due to their high penetrability and low sample photo-damage.[173] Generally, in dye laser systems, the standard pump source is the frequency-doubled Nd:YAG light with a emission wavelength of 532 nm. However, the commercial long-wavelength (≥650 nm) laser dyes show relatively low absorption cross sections at such pumping wavelength, which limits the lasing efficiency and hinders the development of long-wavelength lasers. One effective way to overcome this limitation is to construct a laser system with the assistant of Fòrster resonance energy transfer (FRET) between several different types of laser dyes (i.e. donor and acceptor). The FRET process occurs when the emission of a donor has a large spectral overlap with the absorption of a nearby acceptor. The donor at excited state will non-radiatively transfer its energy to the acceptor at ground state and promote the excitation of the acceptor.[40] As a result, a wavelength-tunable laser system can be achieved via choosing suitable laser dyes and controlling their doping ratio. A number of FRET-assisted RLs have been established in various systems such as biopolymeric matrix dye-doped latex scattering particles and plasmonic nanostructures.[110,174–177] However, these FRET systems are too complicated to achieve mass production with low cost. In 2010, Vohra and co-workers shows that a FRET system can be easily and effectively fabricated based on the polymeric nanofibers via electrospun technology.[178] This electrospun technology is particularly promising in the field of photonics, since it offers a flexible approach to select the optical refractive index, gain and absorption of the fibers. These electrospun polymer fibers and fiber networks also hold great promising in the applications of sensing [179,180] and tissue-growth.[181,182] Although electrospun polymer fiber have been demonstrated to be an ideal FRET systems, to the best of our knowledge, only energy transferred fluorescence emission has been observed in previously reports.[178,183,184]

In the RL systems, one important feature is the intrinsic spectral intensity fluctuation. This spectral intensity fluctuation behavior is rich in the physical mechanism reflecting the interaction between the nonlinearity and randomness in the RL systems, which have been lately exploited in several studies. In these studies, the replica symmetry breaking (RSB) phenomenon, an important concept in the spin-glass theory, has been observed among different RL systems. Spin-glass theory is one of the primary physics mechanism in many research fields, such as biological systems, ultracold atoms, and random photonics.[1,71,185,186] Based on the prediction of the spin-glass theory from the equilibrium perspective, the identical systems may reach different states under identical conditions. The transition to a glassy state is known as RSB, which is indicated by the variation of the statistical distribution of the Parisi overlap (i.e. order parameter). The first theoretical models that introduced the term of spin-glass into the photonic context was proposed by Angelani and co-workers. They demonstrated that the light propagation in nonlinear disordered media shows complex glassy behavior and they theoretically predicted that RSB can be tested in RL systems.[187,188] In 2015, the first experimental evidence of the RSB in RL was reported by Ghofraniha *et al.*,[189] in which the spectral intensity fluctuation overlap (IFO) is defined to as an analog to the Parisi overlap parameter. It was found that the statistical property of IFO exhibited the spin-glass phase behavior under high pump energy, whereas it became paramagnetic phase at low pump energy. The phase transition occurred at the laser threshold. In the same year, a comprehensive disordered mean-field model was presented by Antenucci F. *et al.*, describing the complete phase diagram from close cavity to open cavity in terms of disorder strength and nonlinearity within the replica analysis. They also theoretically predicted the RSB phase transition can be found in a RL system with quenched disorder.[190] Thereafter, many studies reported that the RSB phenomenon can be observed in different RL systems with different configuration such as Er-doped fiber laser with random grating, Rhodamine B laser dye soliton with ZnO scattering particles, and Rhodamine 6G laser dye soliton with specially designed TiO_2 scattering particles.[82,191,192] Thus, using spin-glass theory to analyze the statistical behavior of the RL system provides a new approach to understand the physical mechanism inside the RL. For example, it was found that the spin-glass phase also corresponds to the previously reported Levy distribution regime in RL systems. However, all the previous studies of RSB phenomenon in RLs were demonstrated in a single gain system. For the FRET-assisted RLs, two or more gain materials (donor and acceptor) co-exist in the system and form a multiple energy level configuration. The energy transfer between the doped dyes might modify the nonlinearity of the whole systems and further influence the statistical behavior of the RL system. However, the corresponding statistical study has not been conducted yet. The feasibility of using spin-glass theory to statistical investigate the multi-energy level photonic system like FRET-assisted RL remains a question.

In this chapter, an advanced electrospun technology is employed to prepare micro-scale polymer fiber, which serves as the framework of FRET system. The gain materials in this FRET system is consist of two laser dyes: pyrromethene 597 (PM597) as the donor and nile blue (NB) as the acceptor. Due to the multiple light scattering provided by the inhomogeneous internal structure of the electrospun polymer fiber, the random lasing behavior has been observed in the FRET system. The lasing wavelengths are located in two spectral bands, corresponding to the emission of the PM597 and NB dyes, respectively. When the PM597/NB ratio is 0.67/1, only the random lasing with wavelength centered at 685 nm appear in the lasing spectra, which indicates the occurrence of energy transfer from PM597 to NB. Furthermore, it is found that the mass ratio of PM597/NB has an obvious influence on the relative lasing intensity between two lasing wavelength bands, reflecting the variation of the energy transfer degree. In view of this, FRET-assisted RL is successfully demonstrated based on electrospun polymer fiber. To further analyze the statistical properties of RL, I calculated the statistical distribution function $P(q)$ of the IFO parameter q. A clear transition, that is the RSB, between a continuous wave paramagnetic regime and a spin-glass phase has been observed in the FRET-assisted RL. The statistical results prove that the spin-glass theory can be used to describe the multi-energy level photonic system. The relationship between the FRET-assisted RL and the single gain RL regarding to the statistical properties of the lasing intensity fluctuation has been discussed, which helps people to better understand the inner link between the spin-glass system and RL in the aspect of statistical physics.

6.2 Fabrication of electrospun polymer fiber doped with dyes

The advanced technology-electrospun is introduced to fabricate micro-scale polymer fiber. Firstly, four electrospun sample solutions with same amount of host materials and different PM597/NB mass ratio were prepared. The host materials were obtained via dissolving wt. % 33.4 poly(methyl methacrylate) (PMMA) in wt. % 0.3 PM597/NB-doped dichloromethane (CH_2Cl_2). The mass ratio of PM597/NB for the four samples was adjusted to be 0.67/1, 1/1, 1.5/1, and 3/1, respectively. Secondly, the as-prepared four sample solutions were used to fabricate four micro-scale polymer fibers samples by the electrospun method.[193] A metal needle attached with a 5 ml syringe containing the spinning solution worked as the positive electrode and a high voltage about 10 KV was applied on it. The inside diameter of the metal needle is about 0.9 mm. The grounded electrode was connected to a metal collector covered with metal wafer (20×40 cm). The distance between the needle tip and the collector was fixed at 20 cm. The feed rate of solutions was controlled at 0.8 mm/min by means of a single syringe pump. Figure 6.1 shows the optical images of two dye doped-electrospun polymer fibers with PM597/NB mass ratio of 0.67/1 and 1.5/1 under the pump of 532 nm pulse laser. The diameters of these two samples are about 218 μm and 248 μm, respectively. Moreover, it clearly shows the location of laser pumping and the fluorescent emission spot.

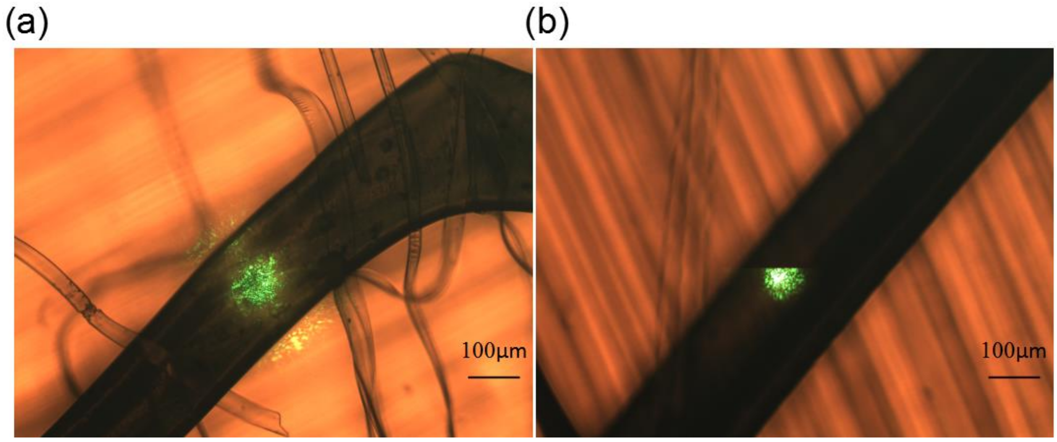

Figure 6.1 The optical images of two dye doped-electrospun fibers with the PM597/NB mass ratio of 0.67/1 (a) and 1.5/1 (b) under the pump of 532 nm pulse laser.

6.3 Emission and random lasing measurement

6.3.1 Measurement set-up

The emission spectra measurement setup was built based on the microscope system (Ideaoptics Co. Ltd) to obtain the detailed experimental data. As shown in Figure 6.2, a Q-switched Nd:YAG laser which outputs a Gaussian profile spot with a wavelength of 532 nm (pulse duration 10 ns, repetition rate 10 Hz, spot diameter 100 μm) is used to serve as pumping source. The pump pulse energy and polarization are controlled by a Glan Prism group. Two mirrors are employed to change the pumping laser path and guide the pumping laser into the microscope system. The pumping laser is totally reflected by a dichroic mirror and focused onto the samples via an objective. Samples are excited by 532 nm laser to generate fluorescence emission/random lasing. The emitted light is collected by the same objective and passes through dichroic mirror with total transmission. Then the collected light is focused onto a beam splitter via the concave lens, where 50% of the light is sent to a CCD camera to obtain the images of the samples. The remaining 50% of the light is directly collected with a fiber-coupled spectrometer (QE65PRO, Ocean Optics, Inc., resolution ~0.4 nm, integration time 100 ms).

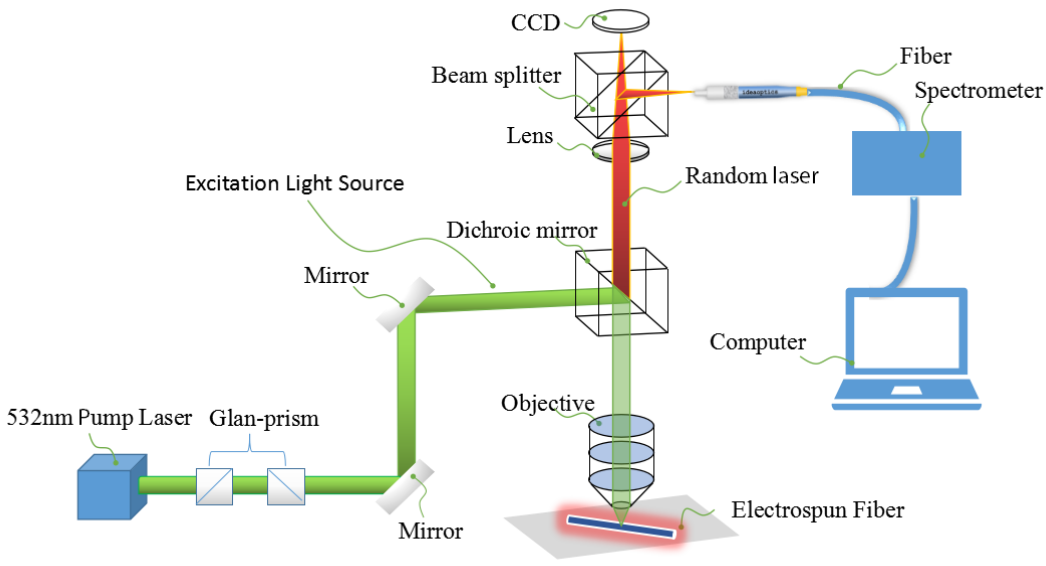

Figure 6.2 Microscope measurement setup. A Q-switched Nd:YAG laser which outputs a round-shape spot with a wavelength of 532 nm (pulse duration 10 ns, repetition rate 10 Hz, spot diameter 100 μm) is used to serve as pumping source. Fiber spectrometer (QE65PRO, ocean optics, resolution ~0.4 nm, integration time 100 ms) is be used to collect the emission spectra.

6.3.2 Characterization of dye solution

To characterize the basic optical properties of the selected laser dyes, we firstly measured the absorption and fluorescence spectra of the donor dye (PM597), the acceptor dye (NB), and the mixed dye (PM597/NB), respectively. As shown in Figure 6.3a, the mixture of PM597/NB exhibits two broad absorbance peaks with the wavelengths of 526.5 nm and 646 nm, which correspond to the absorbance peaks of the PM597 and NB dye, respectively. The basic requirement of constructing a FRET system is that the emission of the donor should has a good spectral overlap with the absorption of the acceptor. Figure 6.3b shows the comparison between the emission spectrum of the PM597 and the absorption spectrum of the NB. It clearly shows that the two spectra have a good overlap in the wavelength range between 550 nm and 650 nm, indicating that the donor PM597 at excited state can effectively populate the acceptor NB at ground state via energy transfer process. It should be noticed that the absorption spectrum of the NB is a little far away from the 532 nm pump wavelength and does not fully cover the emission spectrum of the PM597. This is to prevent the acceptor (NB) from being directly excited by the pump laser. To confirm this, we used the 532 nm laser to directly pump NB dyes. The results are shown in Figure 6.4.

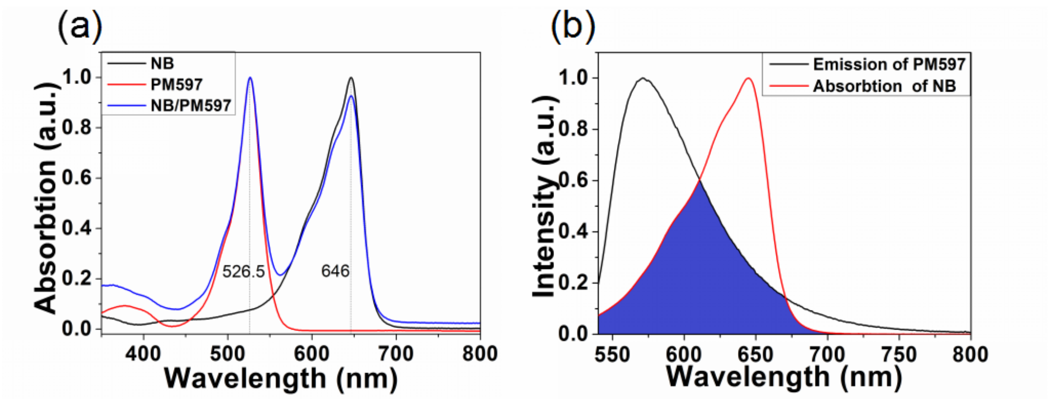

Figure 6.3 (a) The normalized absorption spectra of the donor dye PM597 (red), the acceptor dye NB (black), and the mixed dye of PM597/NB (blue), respectively. (b) The comparison between the normalized emission spectrum of the donor dye PM597 (black) and the normalized absorption spectrum of the acceptor dye NB (red), respectively. The blue shadow indicates the spectral overlap.

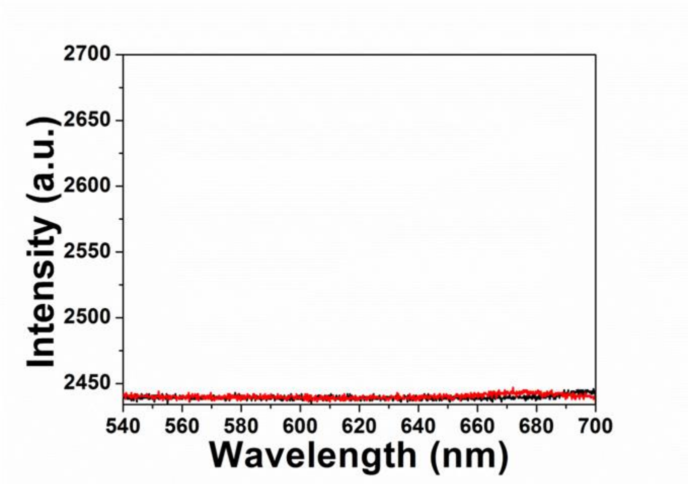

Figure 6.4 The emission spectra of NB under the 532 nm pump with the energy ~ 500 μJ (black curve) and 800 μJ (red curve).

To verify whether the PM597 and NB dyes are suitable donor and accepter for FRET process, the emission spectra of the PM597 dye, the NB dye, and the mixture of PM597/NB are measured, as shown in Figure 6.5a. It can be seen that the PM597/NB mixture only contains one emission peak located at 674.4 nm matching the emission of the NB dye. This is because the PM597 dyes (donor) transfer their energy to the nearby NB dyes (acceptor) instead of directly emitting the fluorescence. As a consequence, the fluorescence from the excited NB dyes will dominate the emission spectrum of PM597/NB. This energy transfer process is the so-called FRET. The results imply that the mixture of PM597/NB dyes is an ideal gain material for the construction of FRET system. In addition, the fluorescence lifetimes of PM597 mixed with and without NB were measured, as shown in Figure 6.5b. The value of fluorescence lifetime L_f can be formulated as $L_f = (T_{n=1,2} - T_0) / e$, where T_0, T_1 and T_2 are the time frames about 56.1 ns, 57.1 ns and 62.4 ns, respectively. As we can see, the presence of NB suppresses the lifetime of donor PM597, because the energy transfer between the donor and acceptor introduces additional non-radiative decay channel to the donor and result in a reduced lifetime. The lifetime results further confirmed that the FRET system has been successfully constructed based on the PM597 and NB dyes.

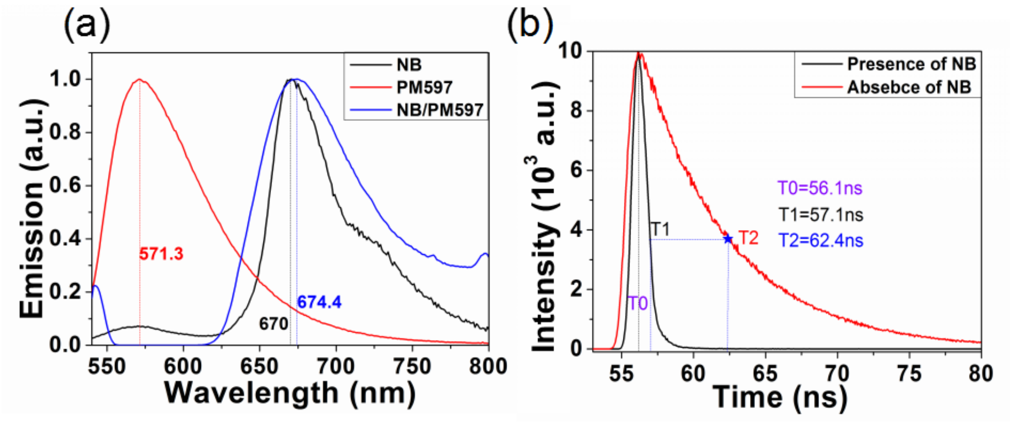

Figure 6.5 (a) The emission spectrum of the NB dye, the PM597 dye and the NB/PM597 mixture. (b) The luminescence decay curves of PM597 with (red curve) and without (black curve) NB.

6.3.3 Random lasing in electrospun polymer fiber

A comprehensive study was carried out regarding to the fluorescence emission and random lasing performance of the electrospun polymer fibers with different PM597/NB dye ratio. The optimal FRET-assisted random lasing action was observed from the sample with the PM597/NB ratio of 0.67/1, as shown in Figure 6.6. The random lasing peaks centered at 683.5 nm dominant the whole lasing spectrum. As the ratio of

PM597/NB increased, a new group of lasing peaks around 570 nm, corresponding to the emission of PM597, started to emerge in the emission spectrum, see in Figure 5b and c. When the ratio of PM597/NB increased up to 3/1, the original random lasing peaks located in the emission band of NB degenerated to a week fluorescence peak, whereas the random lasing peaks could be only found in the emission band of the PM597. This is because the FRET efficiency became weak as the proportion of the doped PM597 increased. The evaluation of the lasing spectra indicates that the variation of the donor-accepter ratio would influence the FRET efficiency and further switch the random lasing wavelengths. The random lasing phenomenon observed in the electrospun polymer fiber results from the light multiple scattering caused by the inhomogeneity of the internal structure of the electrospun polymer fiber. Moreover, a control sample with only NB was prepared. No random lasing can be observed in the control sample, because the absorption of NB is quite low at the standard pump wavelength (532 nm) and the NB dye cannot be excited without FRET process. In view of this, the FRET-assisted electrospun polymer fiber RLs has been successfully demonstrated and its laser properties can be tuned via controlling the donor/acceptor ratio.

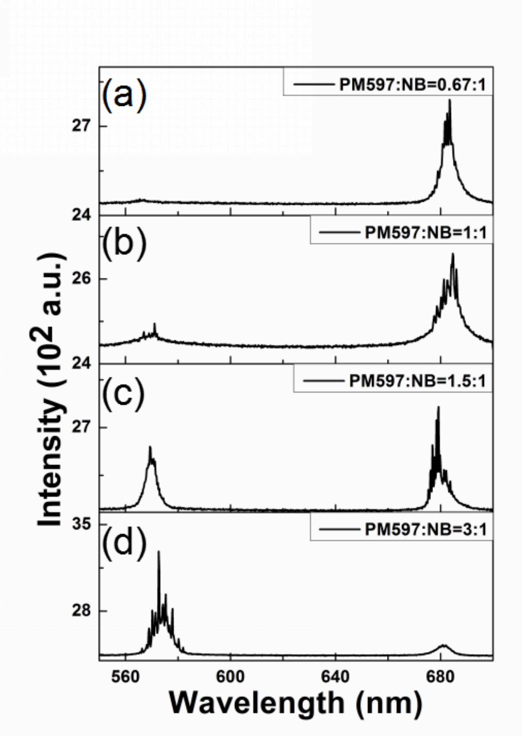

Figure 6.6 The energy transfer random lasing spectra from the samples with the PM597/NB ratio of 0.67/1 (a), 1/1 (b), 1.5/1 (c) and 3/1 (d).

To further study the optical properties of the FERT-assisted electrospun polymer fiber RLs, the emission spectra of the above-mentioned four samples at different pump energy are measured, see results in Figure 6.7. For all the four samples, a broad spontaneous emission was observed at a low pump energy. When the pump energy increased over threshold, the multi-mode spike peaks began to emerge with the main peaks at wavelengths of 683.56 nm, 684.57 nm, 679.26 nm, and 572.68 nm, respectively. The dependence of the integrated peak emission intensities on the pump energy were extracted from the corresponding emission spectra, as shown in Figure 6.7b, d, f and h. The integrating range are 672.83 nm-693.03 nm for the cases in Figure 6.7b, d and f and 584.93 nm-563.84 nm for the case in Figure 6.7h. Laser threshold behavior was observed in all four samples. Their laser threshold values were determined to be 132.5 μJ, 418.2 μJ, 315.5 μJ, and 40.93 μJ, respectively.

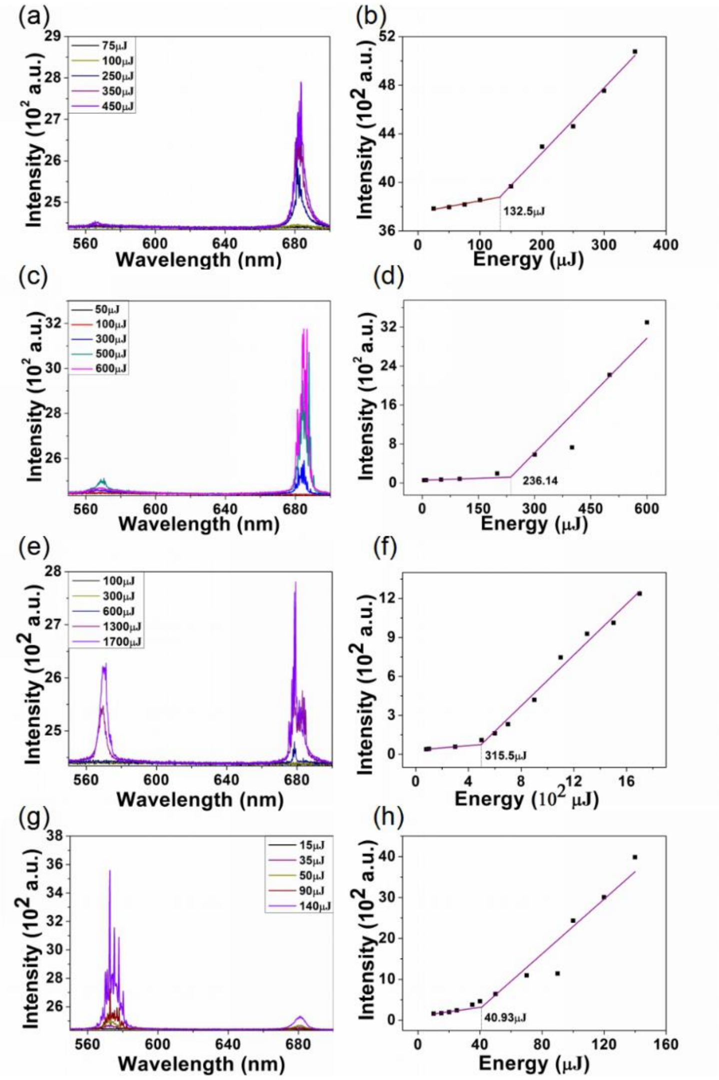

Figure 6.7 Spectral properties of the FRET-assisted RL. The emission spectra of the four samples with the PM597/NB ratio of 0.67/1 (a), 1/1 (c), 1.5/1 (e) and 3/1 (g) at different pump energy. The corresponding integrated emission intensities of the four samples with the PM597/NB ratio of 0.67/1 (b), 1/1 (d), 1.5/1 (f) and 3/1 (h) at different

pump energy

6.3.4 Waveguide effect

In the FRET-assisted electrospun polymer fiber RL, the electrospun polymer fiber can serve as an optical waveguide, allowing the propagation of the emission and lasing along the electrospun polymer fiber. Therefore, it is worthwhile to investigate the properties of the random lasing during the propagation inside the electrospun polymer fiber. To this end, the lasing spectra of the sample with the PM597/NB ratio of 0.67/1 were collected and the collection point is controlled to have a different distance from the pump region, see Figure 6.8. The corresponding collection configurations are shown in Figure 6.9. In Figure 6.8, we traced three main lasing peaks P_1-P_3 from the collected lasing spectra. It was found that the wavelengths of the lasing peaks are slight varied in different lasing spectra. For the lasing peak P_1, a ~0.3 nm blue-shift (from 682.2 nm to 681.9 nm) has been observed in the spectrum collected with a distance of 229 μm from the pump region. Meanwhile, the lasing peak P_2 has a ~0.21 nm red-shift (from 685.12 nm to 685.33 nm) in the case of 170 μm separation distance. For the lasing peak P_3, it was absence in lasing spectra collected with a distance of 170 μm and 193 μm from the pump region. Such spectral variation can be attributed to the inhomogeneity of the electrospun and emitting directions of the excited random lasing modes.[36] As a result, through different collection points, the collected lasing modes are different.

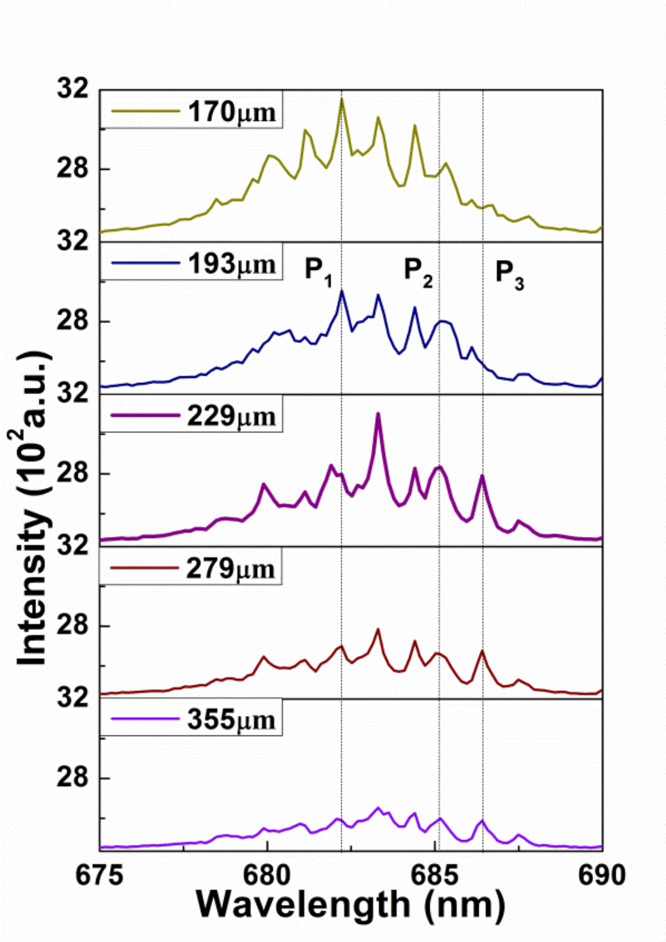

Figure 6.8 Characterization of the random lasing propagation in the FRET-assisted electrospun polymer fiber. The RL emission spectra for different reception location the electrospun polymer fiber with the PM597/NB ratio of 0.67/1.

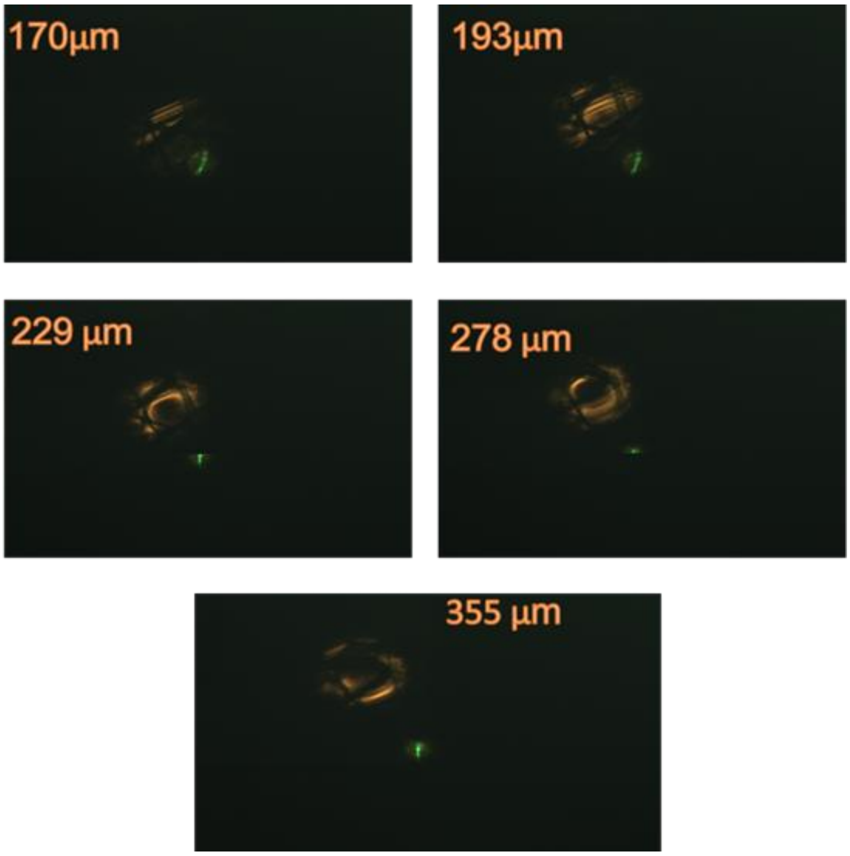

Figure 6.9 The images of the electrospun polymer fiber with the PM597/NB proportion of 0.67/1. The green spot indicates the laser pumping point. The yellow spot indicates the emission spectra detection point. The separation distances between the pumping and detection points are listed in yellow.

6.3.5 Spectral fluctuation of random lasing

The traditional RL systems with single gain materials has been demonstrated to exhibit an intrinsic feature of intensity fluctuation.[68] In the FRET-assisted electrospun polymer fiber RL, it contains two gain materials which form a multi-energy level system with the assistant of FRET process. To investigate whether such multi-energy level RL shows the similar feature, I measured the lasing properties for several times under the same experimental condition. Figure 6.10a shows the random lasing spectra from pulse to pulse pump for FRET-assisted electrospun polymer fiber RL with PM597/NB ratio of 0.67/1 at the same pump energy ~ 450 μJ. It can be seen that the random lasing wavelengths remain unchanged, but their lasing intensities vary from pulse to pulse. Moreover, I measured another sample with PM597/NB ratio of 1/1 and similar intensity fluctuation behavior was observed, as shown in Figure 6.10b. There results indicated that the FRET-assisted electrospun polymer fiber RL is consisted with the single gain RL system regarding to the intensity fluctuation. The physical mechanism of this intensity fluctuation behavior can be attribute to the strong competition and coupling between the numerous modes in the RL system.[129]

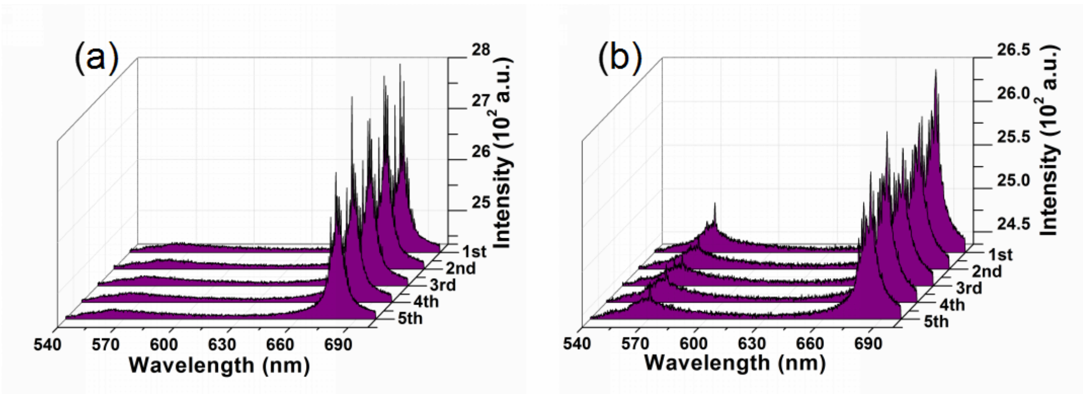

Figure 6.10 Demonstration of random lasing spectra fluctuation. The random lasing with different times pump with PM597/NB ratio of 0.67/1 (a) and 1/1(b).

6.4 Replica symmetry breaking

6.4.1 Theocratical background

Several recent studies have attempted to describe the dynamic of this intensity fluctuation phenomenon via the approach on the basis of spin glass theory.[188,194] The connection between spin-glass and RL is established on the account of the analogy between the continuous complex spin variables and the lasing modes. For a solid RL system, the scattering configuration is fixed and the disorder of the whole system does not change over time, termed quenched. According to the spin-glass theory, the intensity fluctuation (i.e. non-deterministic and irreproducible behavior of the laser modes) results from the frustration caused by the quenched disordered interaction, which corresponds to a glassy light behavior. During the transition to the glassy light regime, an important phenomenon, the so-called RSB has been observed in the single gain RL system, which reveals the non-trivial modes organization and correlation.[71,189] To analyze the glassy behavior and possible RSB transition in the multi-gain RL system, a statistical study was carried out based on the FRET-assisted electrospun polymer fiber RL using the replica method. The replica in spin-glass system stands for the identical system realizations under the same experimental condition. The RSB transition is characterized by the variation of the statistical distribution of Parisi overlap parameter which is associated with the system replica and reflects the interaction of the different states in a spin glass system. In the case of RL system, the theoretical replica is related with the amplitudes of the laser modes from the same RL system under the same pump energy in each shot. However, the phase information of the laser modes is not easy to be obtained in the experiments, which hinders the evaluation of the laser modes amplitudes. The only experimentally accessible information of the laser modes is the intensity magnitudes. Thus, the real replica in RL system is defined as the lasing spectrum containing the laser modes intensities $I_j \propto |a_j|^2$, where a_j is the amplitude of the longitudinal mode *j*. Under each pump energy, N_s system replicas were measured (i.e. laser spectra). The intensity fluctuation overlap parameter q, an analogy to the Parisi parameter, is introduced and calculated as

$$q_{\alpha\beta} = \frac{\sum_{K=1}^{N} \Delta_\alpha(k)\Delta_\beta(k)}{\sqrt{\sum_{K=1}^{N} \Delta_\alpha^2(k)}\sqrt{\sum_{K=1}^{N} \Delta_\beta^2(k)}} \tag{6.1}$$

where α, β=1, 2,…, N_s are the different replica indexes and $\Delta_i(k)$ is the intensity fluctuation of the i-th replica at the wavelength index *k*. $\Delta_i(k)$ is given by the equation $\Delta_i(k) = I_i(k) - \overline{I_i}(k)$. The total number of the overlap parameter q is $Ns(Ns\text{-}1)/2$. Then, the distribution $P(q)$ of the overlap parameters is analyzed to determine the system regime.

6.4.2 Experimental results analysis

We first investigate the RSB transition in the FRET-assisted electrospun polymer fiber RLs with PM597/NB ratio of 0.67/1. For each pump energy, 1100 emission spectra are collected. The wavelength index *k* is in the range between 664.92 nm and 690.11 nm with a spectral resolution of 0.4 nm. Figure 6.11 shows the distributions $P(q)$ of the overlap parameters calculated from emission spectra at different pump energy. It was found that the distribution $P(q)$ are centered around q=0 below the laser threshold, as shown in Figure 6.11a-b. This indicates that the modes are independent, corresponding to the RL system in an uncorrelated paramagnetic regime. As the pump energy increases, the distribution $P(q)$ broadens and finally reaches the boundary of q=±1 with two humps (Figure 6.11c-d). This suggests that the coupling between the laser modes becomes stronger and results in a non-trivial overlap distribution with the increasement of energy, which is referred as spin-glass phase. The variation from paramagnetic regime to spin-glass phase is a typical feature of the RSB transition.

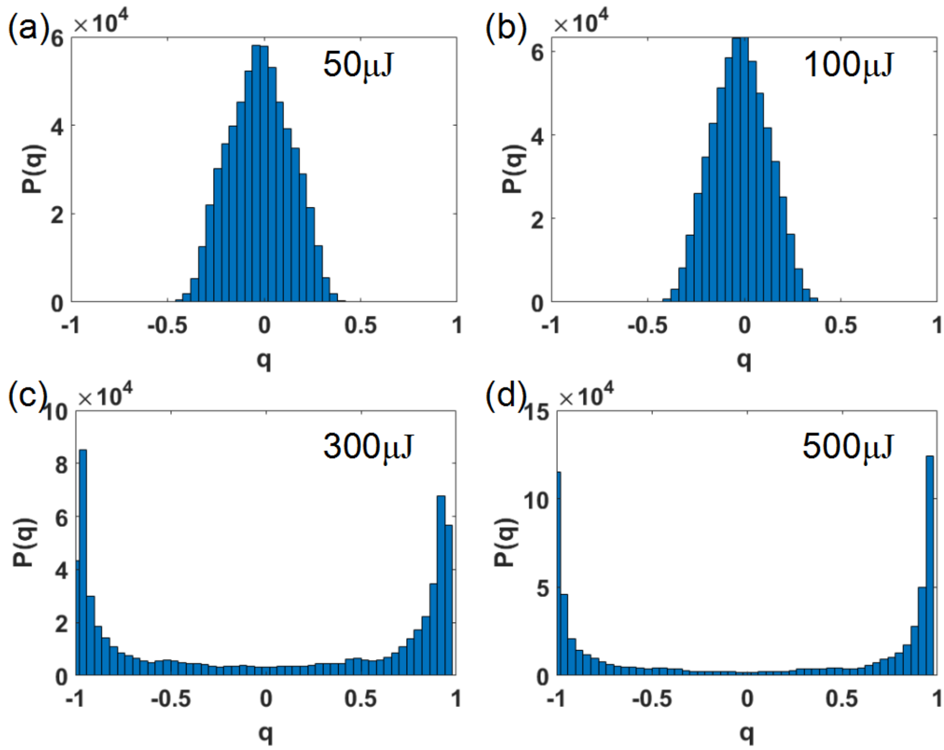

Figure 6.11 Distribution function of the overlap parameter q obtained from the FRET-assisted RL with PM597/NB ratio of 0.67/1 at the pump energy of 50 μJ (a), 100 μJ (b), 300 μJ (c), and 500 μJ (d).

To determine the relationship between RSB transition and the pump energy the dependency of the $|q|_{max}$, the q value of the maximum of $P(|q|)$, on the pump energy is calculated and plot in Figure 6.12. An abrupt increase of the $|q|_{max}$ occurs at the pump energy of 130 μJ, denoting the RSB transition from a continuous wave paramagnetic regime to a spin-glass regime. It is interesting to find that this pump energy is just the laser threshold determined in Figure 6.7. Moreover, the glassy behavior in another two FRET-assisted electrospun polymer fiber RLs with the PM597/NB ratio of 1/1 and 1.5/1 was also studied. The corresponding results are shown in Figure 6.13 and 6.14, respectively. The trend of the distribution $P(q)$ obtained from these two samples is qualitatively the same with the first case, which proves that RSB is always present in the FRET-assisted RLs. Based on analyzing the variation of the $|q|_{max}$ at different pump energy, it was found that the RSB transition also occurs at the laser threshold, as shown in Figure 6.12. This result is in consistent with the RSB transition in the single gain RL systems reported in previous studies. It seems that the existence of the two laser dyes and FRET process will not influence the glassy behavior and RSB transition in the RL system. This is because the duration time of the energy transfer is much smaller than the lifetime of the laser dyes and the total lifetime of the FRET system is similar as that of a single laser dye in the 10^{-8} s timescale.[195] Compare with the total experiments time (around half an hour in our case), The timescale of the FRET process is too small to influence the randomness and the nonlinearity of the whole system.[82] Thus, the glassy behavior in the FRET-assisted RL shows no difference with that in the single gain RL system. In addition, the glassy behavior in the sample with PM597/NB proportion of

3/1 (Figure 6.15) was conducted. As mentioned in above section, this sample only generates the random lasing in the emission band of the PM597 and can be regarded as a traditional single-gain RL. The emission spectra collected from the sample is selected in the spectral range between 550.8 nm and 575.14 nm. Similarly, the RSB transition from a continuous wave paramagnetic regime to a spin-glass phase is observed at the laser threshold (Figure 6.12d). In view of this, the RSB transition is robust in the RL system with and without FRET process, which can be regarded as an indicator of the laser threshold.

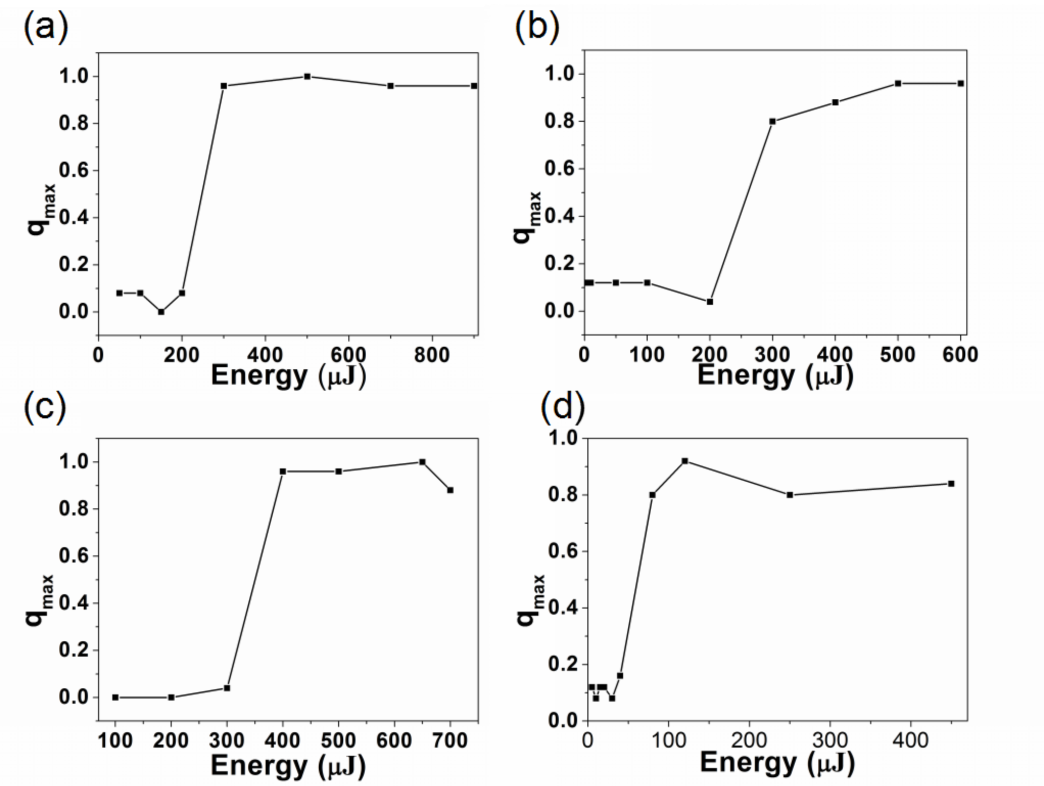

Figure 6.12 The parameter $|q| = q_{max}$ as a function of the pump energy for the samples with ratio of 0.67/1 (a), 1/1 (b), 1.5/1 (c) and 3/1 (d).

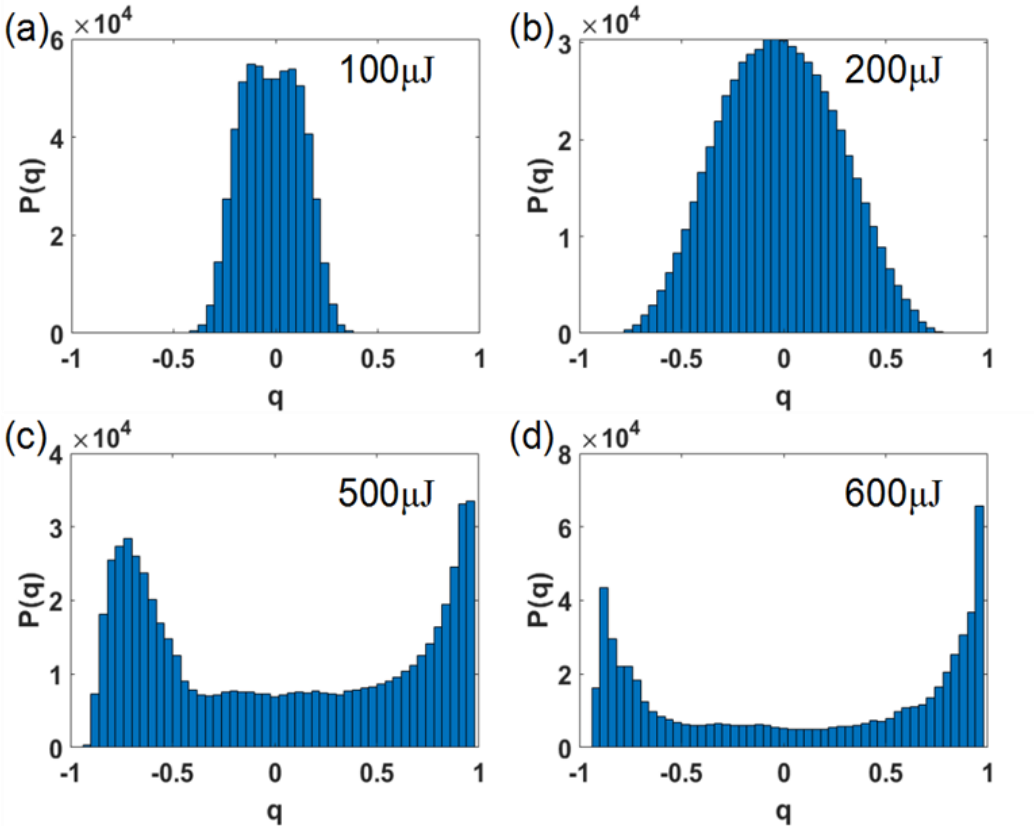

Figure 6.13 Distribution function of the overlap parameter q obtained from the FRET-assisted RL with PM597/NB ratio of 1/1 at the pump energy of 100 mJ (a), 200 mJ (b), 500 mJ (c), and 600 mJ (d).

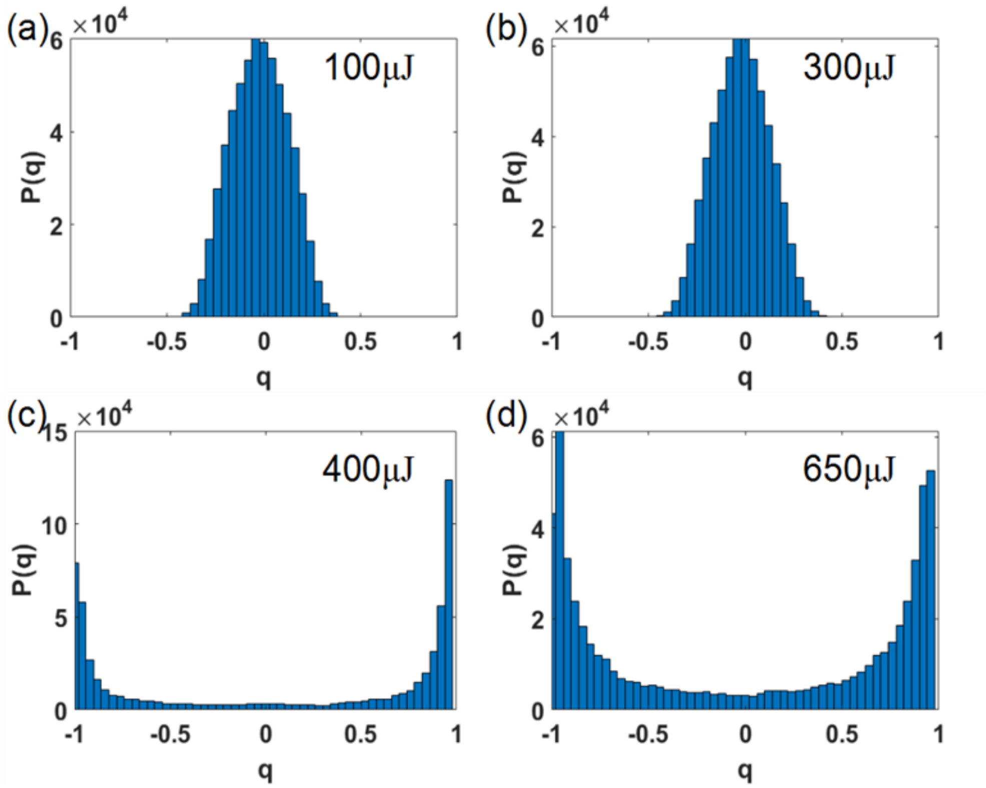

Figure 6.14 Distribution function of the overlap parameter q obtained from the FRET-assisted RL with PM597/NB ratio of 1.5/1 at the pump energy of 100 mJ (a), 300 mJ (b), 400 mJ (c), and 650 mJ (d).

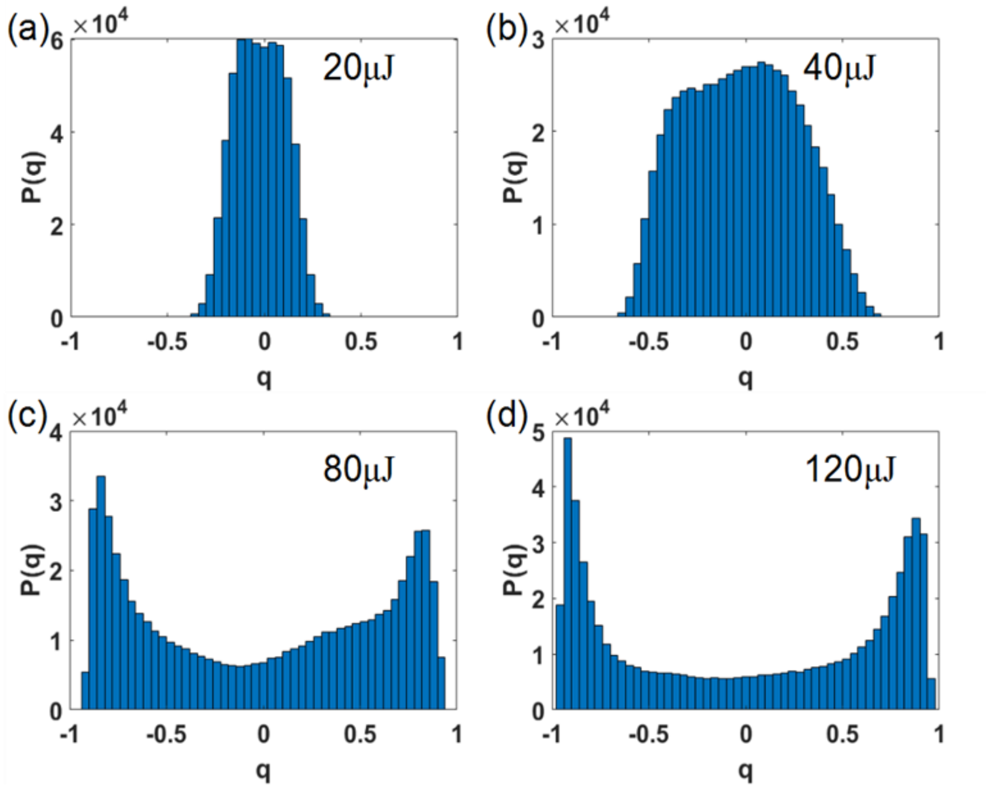

Figure 6.15 Distribution function of the overlap parameter q obtained from the FRET-assisted RL with PM597/NB ratio of 3/1 at the pump energy of 20 mJ (a), 40 mJ (b), 80 mJ (c), and 120 mJ (d).

6.5 Summary

To summary, an advanced technology – electrospun has been introduced to construct a FRET-assisted RL system, which achieves efficient long-wavelength (≥650 nm) random lasing at the standard pump wavelength (532 nm). The donor (pyrromethene 597) and acceptor (nile blue) laser dyes are introduced to the as-fabricated electrospun micro-scale polymer fiber to form a FRET system. Under the excitation of 532 nm pump laser, the energy transition from donor to acceptor is observed and it depends on the ratio between donor and acceptor. The optimal FRET random lasing is obtained from the electrospun polymer fiber RL with a PM597/NB ratio of 0.67/1. This work provides a new approach to realize mass production of RLs with FRET process, promoting the development of RL for real application. Furthermore, based on the statistical study of the lasing properties in FRET-assisted electrospun polymer fiber RL, the phase transition between a continuous wave paramagnetic regime (below threshold) and spin-glass regime (above threshold) was observed, representing RSB phenomenon. Our results prove that spin-glass theory can be used to describe the statistical properties of the FRET-assisted RL system, which open up new possibilities for the study of other glassy behaviors in the RL system with complex energy levels and energy cascaded process, for example, quantum cascade laser.

Chapter 7 Conclusion and Future Work

7.1 Conclusion

This thesis presents the research works I did during my PhD studies. Several novel types of RL have been demonstrated in different optical systems with disordered micro\nanostructures. These studies contain the details of the RLs in terms of the sample fabrications, experiment measurements, theory analyzation and numerical simulation. Both coherent and incoherent random lasing have been observed with the variation of system configuration and scattering strength. Some of the RLs are utilized for sensing and speckle-free imaging, showing the potential of RL in real application.

The initial work in this thesis is about the demonstration of RL in POF doped with fluorescence dye and scattering nanoparticle. The detailed fabrication process is presented. Due to the waveguide effect, multimode and coherent random lasing is achieved, although the doped scattering particles can only provide weakly scattering. This waveguide enhancement effect is further confirmed by the PFT analysis of the lasing cavity sizes. Then, a speckle free imaging application is present using the POFRLs as the illumination source due to the low spatial coherent. Besides the experiment investigation, a numerical model based on Monte Carlo method was proposed to reproduce the experiment observation, showing a good agreement regarding to the random lasing dynamic. This work built a primary connection between the numerical simulation and experiment demonstration of 1-dimentional random fiber laser.

In the second study, a label-free RL cytometer is reported. The sensing strategies is based on the feature that the random lasing properties (i.e. lasing threshold, wavelength, PFT results) is highly sensitive to the scattering strength and structure configuration. It shows that the lasing threshold is dominated by the whole-cell scattering of the biofluids. The subcellular structure of the cells will contribute the lasing wavelength shift. This has been further confirmed by the PFT analysis. Finally, a principle component analysis is performed to realize cell type classification, in which the first order principle component can work as a good indicator for detecting cancerous cells in cell mixtures. This work is the first random-laser-based cytometer, which opens a new way to integrate RL with novel optical systems for sensing application.

Instead of using traditional laser dye to provide optical gain, in the third work presented in this thesis, a novel material, perovskite $CsPbBr_3$ QDs, is utilized to construct RL system due to its excellent photoluminescence properties. Moreover, the scattering structures are formed by randomly distributed GNRs, which not only provide strong scattering but also enhance the emission efficiency of the PQDs due to the plasmonic effect. The morphology of the GNRs is precisely modified to exhibit two plasmonic resonance modes, which spectrally match the two-photon absorption and emission of $CsPbBr_3$ QDs to achieve dual-plasmonic enhancement. Taking the advantage of the strong plasmonic effect, coherent random lasing is easily achieved with low threshold in room temperature. By changing the GNRs density, four distinct emission states are observed, indicating the variation of plasmon-assistant random lasing cavities formation. Then, the spatial coherences of all the fabricated samples are measured, their capabilities for speckle free imaging are also tested. The plasmonic enhancement strategy proposed in this work will advance the RL systems with novel fluorescent materials and benefit the development of PQDs nano-laser.

In the last chapter, I mainly focus on the statistical investigation of the intrinsic randomness of a FRET-assisted RL system, which is demonstrated based on electrospun polymer optical fiber doped with donor (pyrromethene 597) and acceptor (nile blue) laser dyes. The random lasing properties in the electrospun polymer fiber RL with different PM597/NB ratio are investigated. When the ratio is 0.67/1, optimal FRET random lasing is achieved. Moreover, by the analogy of spin glass system, a phase transition between a continuous wave paramagnetic regime (below threshold) and spin-glass regime (above threshold) is observed in FRET-assisted electrospun polymer fiber RL. The transition shows a robust relationship with the random lasing threshold. This work explores the glassy behaviors in a RL system with complex energy levels, which might help the further investigation of the inner relationship between RL and other disordered physical systems.

To provide a better illustration of the random laser systems proposed in this thesis, I compared them with several different random lasers regarding to their properties, as shown in Table 7.1.

Table 7.1 Properties of the random lasers

Ref	Scatterer	Gain	Threshold	Host structure	Coherence	Remark
Chapt. 3	TiO_2	dye	9.2 mJ·cm^{-2}	POF	Coherent	Speckle-free imaging
Chapt. 4	Cell	dye	80.4 nJ·mm^{-2} -96.2 nJ·mm^{-2}	Microfluidic	Coherent	Cell sensing
Chapt. 5	GNR	PQD	0.62 mJ·cm^{-2} -1.79 mJ·cm^{-2}	Film	Coherent Incoherent	Dual-plasmon enhancement
Chapt. 6	Inhomogeneous	Two dyes	0.13 μJ·mm^{-2} -1.33 μJ·mm^{-2}	Electrospun polymer fiber	Coherent	FRET, Replica symmetry breaking
17	Inhomogeneous	InGaAsP	240 μW	Photonic crystal	Coherent	Anderson Localization
88	TiO_2	DOO-PVV	133 nJ	Film	Coherent	Laser cavities
11	ZnO	ZnO	763 kW·cm^{-2}	Powder	Coherent	Self-scattering
196	$BaSO_4$	$BaSO_4$	1.05 mJ	Powder	Incoherent	Raman random laser
197	ZnO	dye	44 μJ·mm^{-2} -220 μJ·mm^{-2}	Solution	Coherent	Levy distribution
18	POSS	PM597	0.41 mJ	Liquid core optical fiber	Coherent	Weak scattering
91	Tilted silver nanorods array	dye	0.4 μJ -0.8 μJ	Film	Coherent	Plasmon enhancement
73	Random grating	Er-doped fiber	16.30 mW	Optical fiber	NA	Optical turbulence
189	Inhomogeneous	T5OCx	0.25 mJ	Film	Coherent	Replica symmetry breaking
46	Inhomogeneous	dye	0.02 mW -0.14 mW	human breast tumor tissues	Coherent	Cancer diagnosis
43	Random pillars	dye	21 μJ·mm^{-2} -44 μJ·mm^{-2}	Microfluidic	Coherent	Wavelength control
40	Inhomogeneous	Two dyes	NA	Polymer nanoparticles	Incoherent	FRET

7.2 Future work

The research studies presented in this thesis can be further extended and have the possibility to show more interesting physical phenomena and attractive applications. Following are some suggested research objective that can be carried out in the future.

(1) Multi-color and white random laser

In the thesis, it shows that the FRET-assisted RLs can generated two emissions with different wavelength. Thus, when additional laser dyes were introduced in to the same RL system, the multi-color random lasing can be achieved. For white lasing, it should contain at least three different colors (red, green and blue, three primary colors) and the ratio between different colors need to be accurately controlled. However, due to the energy transfer between different laser dyes, it will be a challenge to demonstrated white random lasing in a system with mixture dyes. Another issue needs to be considered is that only using single laser as the pump source might not efficiently excite the laser dyes with long emission wavelength due to the low absorption cross section. To demonstrate white random lasing, a simple manner is fabricating polymer optical fibers with multi-core structure. The laser dyes will be separately doped in different cores to avoid undesired energy transfer. Meanwhile, one of the fiber cores can be made as a FRET system enabling high absorption efficiency. The lasing properties can be further modified via bending the polymer optical fibers and changing the pump configuration. The disorder medium used in this multi-color or white RL should have good scattering cross section in a broadband wavelength range, for example, gold nanostars.[37]

(2) Plasmonic random laser

One of the studies in this thesis has already described that the plasmonic effect will highly enhance the random lasing and result in low laser threshold. There are lots of plasmonic nanomaterials (e.g. Au, Ag) with different morphologies (e.g. sphere, rod, cube) showing different resonance wavelengths ranging from ultraviolet to near-infrared, which can be widely used to construct RL systems with different fluorescence materials. Another important feature of the plasmonic nanomaterials is that they can work as nanoantenna and force the emission to be directional.[198] Take the advantage of this, RL with controllable emission direction can be realized based on plasmonic structures, which is always desired in various applications.[99]

In addition, in some special designed plasmonic structures, large magnetic field enhancement can be achieved. This can be used to enhance the emissions which arise from magnetic dipole transitions in some fluorescence materials (e.g. Eu^{3+}) and construct RL systems.[199] Up to date, no RL has been demonstrated based on the emission generated from the magnetic dipole transitions. New phenomenon and lasing dynamic might be found in such RLs.

(3) Phase transition in random laser

The spin glass theory has been applied to analyze the statistical properties of RL which shows a phase transition at the laser threshold. According to the Antenucci's theoretical prediction, the phase diagram of the RL is more complex and can support several phase transitions.[200] However, only one phase transition has been observed in this thesis and previous studies. The vanish of other phase transitions is because the disorder degree of the RL is fixed during the experiment. Some studies show that, by modify the pump intensity via a spatial light modulator, the coupling strength between the random cavities (i.e. disorder degree) inside the RL system can be controlled. This technology might provide an approach for the investigation of the complex phase transitions in RL systems.

(4) Laminar and turbulence

Similar as the analogy between the spin glass system and RL, it was recently reported that the physical phenomena (laminar and turbulence) in fluids can also been found in the RL system based on the statistical analysis.[73] This work further clarify the universality of the statistical behavior between RLs and other complex physical systems. It is worthwhile to carry out more experiment to investigate such optical turbulence phenomenon in different RL system under different experiment conditions, which might help people to better understand and control the random lasing properties.

(5) Machine learning

Machine learning is a powerful algorithm to statistical investigate the mass data and build numerical models to detect patterns and predict results. Very recently, this technology has attracted great attention from optics research community and been introduced to deal with optical studies ranging from silicon photonic, imaging, laser pulse modification to fiber sensing and optical communication.[201–207] Since RL is a complex optical system with numerous random scatterings and nonlinearity lasing dynamic. The machine learning can be utilized to investigate the relationship between the pump condition (input) and lasing properties (output). For example, after intense training, the machine learning model can be used to predict the lasing wavelength and directions under a certain pump condition.[36,43] Vice versa, the properties of the pump, disorder and gain materials can also be determined based on the lasing spectra, enabling the RLs for sensing application.

References

(1) Wiersma, D. S. Disordered Photonics. *Nat. Photonics* **2013**, *7* (3), 188–196 https://doi.org/10.1038/NPHOTON.2013.29.

(2) Segev, M.; Silberberg, Y.; Christodoulides, D. N. Anderson Localization of Light. *Nat. Photonics* **2013**, *7* (February), 197–204 https://doi.org/10.1038/NPHOTON.2013.30.

(3) Redding, B.; Choma, M. a.; Cao, H. Speckle-Free Laser Imaging Using Random Laser Illumination. *Nat. Photonics* **2012**, *6* (June), 355–359 https://doi.org/10.1038/NPHOTON.2012.90.

(4) Wiersma, D. The Smallest Random Laser. *Nature* **2000**, *406* (6792), 133–135 https://doi.org/10.1038/35018184.

(5) Ambartsumyan, R.; Basov, N.; Kryukov, P.; Letokhov, V. A Laser with a Nonresonant Feedback. *IEEE J. Quantum Electron.* **1966**, *2* (9), 442–446 https://doi.org/10.1109/JQE.1966.1074123.

(6) V.S., L. Generation of Light by a Scattering Medium with Negative Resonance Absorption. *Sov. J. Exp. Theor. Phys.* **1968**, *26*, 835–840.

(7) Lawandy, N. M.; Balachandran, R. M.; Gomes, A. S. L.; Sauvain, E. Laser Action in Strongly Scattering Media. *Nature* **1994**, *368* (6470), 436–438 https://doi.org/10.1038/368436A0.

(8) Wiersma, D. S.; van Albada, M. P.; Lagendijk, A. Random Laser? *Nature*

1995, *373* (6511), 203–204 https://doi.org/10.1038/373203B0.

(9) Wiersma, D. S.; Lagendijk, A. Light Diffusion with Gain and Random Lasers. *Phys. Rev. E* **1996**, *54* (4), 4256–4265 https://doi.org/10.1103/PHYSREVE.54.4256.

(10) Cao, H.; Zhao, Y. G.; Ong, H. C.; Ho, S. T.; Dai, J. Y.; Wu, J. Y.; Chang, R. P. H. Ultraviolet Lasing in Resonators Formed by Scattering in Semiconductor Polycrystalline Films. *Appl. Phys. Lett.* **1998**, *73* (25), 3656–3658 https://doi.org/10.1063/1.122853.

(11) Cao, H.; Zhao, Y. G.; Ho, S. T.; Seelig, E. W.; Wang, Q. H.; Chang, R. P. H. Random Laser Action in Semiconductor Powder. *Phys. Rev. Lett.* **1999**, *82* (11), 2278–2281 https://doi.org/DOI 10.1103/PHYSREVLETT.82.2278.

(12) Polson, R. C.; Chipouline, A.; Vardeny, Z. V. Random Lasing in Pi-Conjugated Films and Infiltrated Opals. *Adv. Mater.* **2001**, *13* (10), 760–764.

(13) Frolov, S. V.; Vardeny, Z. V.; Yoshino, K.; Zakhidov, A.; Baughman, R. H. Stimulated Emission in High-Gain Organic Media. *Phys. Rev. B* **1999**, *59* (8), R5284–R5287 https://doi.org/10.1103/PHYSREVB.59.R5284.

(14) Yoshino, K.; Tatsuhara, S.; Kawagishi, Y.; Ozaki, M.; Zakhidov, A. A.; Vardeny, Z. V. Amplified Spontaneous Emission and Lasing in Conducting Polymers and Fluorescent Dyes in Opals as Photonic Crystals. *Appl. Phys. Lett.* **1999**, *74* (18), 2590–2592 https://doi.org/10.1063/1.123907.

(15) Fallert, J.; Dietz, R. J. B.; Sartor, J.; Schneider, D.; Klingshirn, C.; Kalt, H. Co-Existence of Strongly and Weakly Localized Random Laser Modes. *Nat.*

Photonics **2009**, *3* (April), 279–282 https://doi.org/10.1038/NPHOTON.2009.67.

(16) Abaie, B.; Mobini, E.; Karbasi, S.; Ballato, J.; Hawkins, T.; Ballato, J.; Mafi, A.; Ma, A. Random Lasing in an Anderson Localizing Optical Fiber. *Light Sci. Appl.* **2016**, *6* (8), e17041 https://doi.org/10.1038/LSA.2017.41.

(17) Liu, J.; Garcia, P. D.; Ek, S.; Gregersen, N.; Suhr, T.; Schubert, M.; Mørk, J.; Stobbe, S.; Lodahl, P. Random Nanolasing in the Anderson Localized Regime. *Nat. Nanotechnol.* **2014**, *9* (4), 285–289 https://doi.org/10.1038/NNANO.2014.34.

(18) Hu, Z.; Zhang, Q.; Miao, B.; Fu, Q.; Zou, G.; Chen, Y.; Luo, Y.; Zhang, D.; Wang, P.; Ming, H.; et al. Coherent Random Fiber Laser Based on Nanoparticles Scattering in the Extremely Weakly Scattering Regime. *Phys. Rev. Lett.* **2012**, *109* (25), 2–6 https://doi.org/10.1103/PHYSREVLETT.109.253901.

(19) Uppu, R.; Mujumdar, S. Exponentially Tempered Lévy Sums in Random Lasers. *Phys. Rev. Lett.* **2015**, *114* (18), 183903 https://doi.org/10.1103/PHYSREVLETT.114.183903.

(20) Apalkov, V. M.; Raikh, M. E.; Shapiro, B. Random Resonators and Prelocalized Modes in Disordered Dielectric Films. *Phys. Rev. Lett.* **2002**, *89* (1), 168021–168024 https://doi.org/10.1103/PHYSREVLETT.89.016802.

(21) Jiang, X. Y.; Soukoulis, C. M. Time Dependent Theory for Random Lasers. *Phys. Rev. Lett.* **2000**, *85* (1), 70–73 https://doi.org/DOI

10.1103/PHYSREVLETT.85.70.

(22) Ling, Y.; Cao, H.; Burin, A. L.; Ratner, M. A.; Liu, X.; Chang, R. P. H. Investigation of Random Lasers with Resonant Feedback. *Phys. Rev. A* **2001**, *64* (6), 063808 https://doi.org/10.1103/PHYSREVA.64.063808.

(23) Yamilov, a; Wu, X.; Cao, H.; Burin, a L. Absorption-Induced Confinement of Lasing Modes in Diffusive Random Media. *Opt. Lett.* **2005**, *30* (18), 2430–2432 https://doi.org/10.1364/OL.30.002430.

(24) Andreasen, J.; Cao, H. Spectral Behavior of Partially Pumped Weakly Scattering Random Lasers. *Opt. Express* **2011**, *19* (4), 3418–3433 https://doi.org/10.1364/OE.19.003418.

(25) Cao, H. Review on Latest Developments in Random Lasers with Coherent Feedback. *J. Phys. A. Math. Gen.* **2006**, *39* (2), 467–467 https://doi.org/10.1088/0305-4470/39/2/C01.

(26) Andreasen, J.; Asatryan, A. A.; Botten, L. C.; Byrne, M. A.; Cao, H.; Ge, L.; Labonté, L.; Sebbah, P.; Stone, A. D.; Türeci, H. E.; et al. Modes of Random Lasers. *Adv. Opt. Photonics* **2011**, *3* (1), 88 https://doi.org/10.1364/AOP.3.000088.

(27) Misirpashaev, T. S.; Beenakker, C. W. J. Lasing Threshold and Mode Competition in Chaotic Cavities. *Phys. Rev. A* **1998**, *57* (3), 2041–2045 https://doi.org/10.1103/PHYSREVA.57.2041.

(28) Hackenbroich, G.; Viviescas, C.; Elattari, B.; Haake, F. Photocount Statistics of Chaotic Lasers. *Phys. Rev. Lett.* **2001**, *86* (23), 5262–5265

https://doi.org/10.1103/PHYSREVLETT.86.5262.

(29) Herrmann, J.; Wilhelmi, B. Mirrorless Laser Action by Randomly Distributed Feedback in Amplifying Disordered Media with Scattering Centers. *Appl. Phys. B Lasers Opt.* **1998**, *66* (3), 305–312 https://doi.org/10.1007/S003400050393.

(30) Burin, A. L.; Ratner, M. A.; Cao, H.; Chang, S. H. Random Laser in One Dimension. *Phys. Rev. Lett.* **2002**, *88* (9), 093904 https://doi.org/10.1103/PHYSREVLETT.88.093904.

(31) Jiang, X.; Soukoulis, C. M. Localized Random Lasing Modes and a Path for Observing Localization. *Phys. Rev. E* **2002**, *65* (2), 025601 https://doi.org/10.1103/PHYSREVE.65.025601.

(32) Anderson, P. W. Absence of Diffusion in Certain Random Lattices. *Phys. Rev.* **1958**, *109* (5), 1492–1505 https://doi.org/10.1103/PHYSREV.109.1492.

(33) Zhai, T.; Zhang, X.; Pang, Z.; Su, X.; Liu, H.; Feng, S.; Wang, L. Random Laser Based on Waveguided Plasmonic Gain Channels. *Nano Lett.* **2011**, *11* (10), 4295–4298 https://doi.org/10.1021/NL2023096.

(34) Churkin, D. V.; Sugavanam, S.; Vatnik, I. D.; Wang, Z.; Podivilov, E. V.; Babin, S. A.; Rao, Y.; Turitsyn, S. K. Recent Advances in Fundamentals and Applications of Random Fiber Lasers. *Adv. Opt. Photonics* **2015**, *7* (3), 516 https://doi.org/10.1364/AOP.7.000516.

(35) Meng, X.; Fujita, K.; Zong, Y.; Murai, S.; Tanaka, K. Random Lasers with Coherent Feedback from Highly Transparent Polymer Films Embedded with

Silver Nanoparticles. *Appl. Phys. Lett.* **2008**, *92* (20), 2006–2009 https://doi.org/10.1063/1.2912527.

(36) Hisch, T.; Liertzer, M.; Pogany, D.; Mintert, F.; Rotter, S. Pump-Controlled Directional Light Emission from Random Lasers. *Phys. Rev. Lett.* **2013**, *111* (2), 023902 https://doi.org/10.1103/PHYSREVLETT.111.023902.

(37) Ziegler, J.; Wörister, C.; Vidal, C.; Hrelescu, C.; Klar, T. A.; W??rister, C.; Vidal, C.; Hrelescu, C.; Klar, T. A.; Wörister, C.; et al. Plasmonic Nanostars as Efficient Broadband Scatterers for Random Lasing. *ACS Photonics* **2016**, *3* (6), 919–923 https://doi.org/10.1021/ACSPHOTONICS.6B00111.

(38) Chang, Q.; Shi, X.; Liu, X.; Tong, J.; Liu, D.; Wang, Z. Broadband Plasmonic Silver Nanoflowers for High-Performance Random Lasing Covering Visible Region. *Nanophotonics* **2017**, *0* (0), 0–9 https://doi.org/10.1515/NANOPH-2017-0010.

(39) Hai, T. I. Z.; Hiyang, Z. X. U.; Ongtao, S. L. I.; Hang, X. I. Z.; Zhai, T.; Xu, Z.; Li, S.; Zhang, X. Red-Green-Blue Plasmonic Random Laser. *Opt. Express* **2017**, *25* (3), 2100 https://doi.org/10.1364/OE.25.002100.

(40) Cerdán, L.; Enciso, E.; Martín, V.; Bañuelos, J.; López-Arbeloa, I.; Costela, A.; García-Moreno, I. FRET-Assisted Laser Emission in Colloidal Suspensions of Dye-Doped Latex Nanoparticles. *Nat. Photonics* **2012**, *6* (9), 623–628 https://doi.org/10.1038/NPHOTON.2012.201.

(41) Lu, H.; Xing, J.; Wei, C.; Xia, J.; Sha, J.; Ding, Y.; Zhang, G.; Xie, K.; Qiu, L.; Hu, Z. Band-Gap-Tailored Random Laser. *Photonics Res.* **2018**, *6* (5), 390

https://doi.org/10.1364/PRJ.6.000390.

(42) Bachelard, N.; Andreasen, J.; Gigan, S.; Sebbah, P. Taming Random Lasers through Active Spatial Control of the Pump. *Phys. Rev. Lett.* **2012**, *109* (3), 1–5 https://doi.org/10.1103/PHYSREVLETT.109.033903.

(43) Bachelard, N.; Gigan, S.; Noblin, X.; Sebbah, P. Adaptive Pumping for Spectral Control of Random Lasers. *Nat. Phys.* **2014**, *10* (6), 426–431 https://doi.org/10.1038/NPHYS2939.

(44) Gao, S.; Zhang, L.; Xu, Y.; Chen, L.; Bao, X. High-Speed Random Bit Generation via Brillouin Random Fiber Laser with Non-Uniform Fibers. *IEEE Photonics Technol. Lett.* **2017**, *29* (16), 1352–1355 https://doi.org/10.1109/LPT.2017.2722381.

(45) Polson, R. C.; Vardeny, Z. V. Random Lasing in Human Tissues. *Appl. Phys. Lett.* **2004**, *85* (7), 1289–1291 https://doi.org/10.1063/1.1782259.

(46) Wang, Y.; Duan, Z.; Qiu, Z.; Zhang, P.; Wu, J.; Zhang, D.; Xiang, T. Random Lasing in Human Tissues Embedded with Organic Dyes for Cancer Diagnosis. *Sci. Rep.* **2017**, *7* (1), 8385 https://doi.org/10.1038/S41598-017-08625-3.

(47) Ma, R.; Rao, Y. J.; Zhang, W. L.; Hu, B. Multimode Random Fiber Laser for Speckle-Free Imaging. *IEEE J. Sel. Top. Quantum Electron.* **2019**, *25* (1) https://doi.org/10.1109/JSTQE.2018.2833472.

(48) Hokr, B. H.; Schmidt, M. S.; Bixler, J. N.; Dyer, P. N.; Noojin, G. D.; Redding, B.; Thomas, R. J.; Rockwell, B. A.; Cao, H.; Yakovlev, V. V.; et al. A Narrow-Band Speckle-Free Light Source via Random Raman Lasing. *J. Mod. Opt.*

2016, *63* (1), 46–49 https://doi.org/10.1080/09500340.2015.1078919.

(49) Barredo-Zuriarrain, M.; Iparraguirre, I.; Fernández, J.; Azkargorta, J.; Balda, R. Speckle-Free near-Infrared Imaging Using a Nd3+ Random Laser. *Laser Phys. Lett.* **2017**, *14* (10) https://doi.org/10.1088/1612-202X/AA7874.

(50) Mokan, V.; Ahmadi, P.; Cao, H.; Redding, B.; Seifert, M.; Choma, M. A. Low-Spatial-Coherence High-Radiance Broadband Fiber Source for Speckle Free Imaging. *Opt. Lett.* **2015**, *40* (20), 4607 https://doi.org/10.1364/OL.40.004607.

(51) Gaikwad, P.; Bachelard, N.; Sebbah, P.; Backov, R.; Vallée, R. A. L. Competition and Coexistence of Raman and Random Lasing in Silica-/Titania-Based Solid Foams. *Adv. Opt. Mater.* **2015**, *3* (11), 1640–1651 https://doi.org/10.1002/ADOM.201500247.

(52) Wiersma, D. S. The Physics and Applications of Random Lasers. *Nat. Phys.* **2008**, *4* (5), 359–367 https://doi.org/10.1038/NPHYS971.

(53) Ghofraniha, N.; Viola, I.; Maria, F. Di; Barbarella, G.; Gigli, G.; Conti, C. Random Laser from Engineered Nanostructures Obtained by Surface Tension Driven Lithography. *Laser Photon. Rev.* **2013**, *7* (3), 432–438 https://doi.org/10.1002/LPOR.201200105.

(54) Anderson, B. R.; Gunawidjaja, R.; Eilers, H. Random Lasing and Reversible Photodegradation in Disperse Orange 11 Dye-Doped PMMA with Dispersed ZrO 2 Nanoparticles Random Lasing and Reversible Photodegradation in Disperse Orange 11 Dye- Doped PMMA with Dispersed ZrO 2 Nanoparticles. *J. Opt.* **2015**, *18*, 015403.

(55) Anderson, B. R.; Gunawidjaja, R.; Eilers, H. Self-Healing Organic-Dye-Based Random Lasers. *Opt. Lett.* **2015**, *40* (4), 577–580 https://doi.org/10.1364/OL.40.000577.

(56) Sznitko, L.; Mysliwiec, J.; Miniewicz, A. The Role of Polymers in Random Lasing. *J. Polym. Sci. Part B Polym. Phys.* **2015**, *53* (14), 951–974 https://doi.org/10.1002/POLB.23731.

(57) Luan, F.; Gu, B.; Gomes, A. S. L.; Yong, K. T.; Wen, S.; Prasad, P. N. Lasing in Nanocomposite Random Media. *Nano Today* **2015**, *10* (2), 168–192 https://doi.org/10.1016/J.NANTOD.2015.02.006.

(58) de Matos, C. J. S.; de S. Menezes, L.; Brito-Silva, A. M.; Martinez Gámez, M. A.; Gomes, A. S. L.; de Araújo, C. B. Random Fiber Laser. *Phys. Rev. Lett.* **2007**, *99* (15), 153903 https://doi.org/10.1103/PHYSREVLETT.99.153903.

(59) Li, S.; Wang, L.; Zhai, T.; Chen, L.; Wang, M.; Wang, Y.; Tong, F.; Wang, Y.; Zhang, X. Plasmonic Random Lasing in Polymer Fiber. *Opt. Express* **2016**, *24* (12), 12748 https://doi.org/10.1364/OE.24.012748.

(60) Turitsyn, S. K.; Babin, S. A.; Churkin, D. V.; Vatnik, I. D.; Nikulin, M.; Podivilov, E. V. Random Distributed Feedback Fibre Lasers. *Phys. Rep.* **2014**, *542* (2), 133–193 https://doi.org/10.1016/J.PHYSREP.2014.02.011.

(61) Wu, H.; Wang, Z.; He, Q.; Fan, M.; Li, Y.; Sun, W.; Zhang, L.; Li, Y.; Rao, Y. Polarization-Modulated Random Fiber Laser. *Laser Phys. Lett.* **2016**, *13* (5), 055101 https://doi.org/10.1088/1612-2011/13/5/055101.

(62) Wang, Z.; Wu, H.; Fan, M.; Rao, Y.; Jia, X.; Zhang, W. Third-Order Random

Lasing via Raman Gain and Rayleigh Feedback within a Half-Open Cavity. *Opt. Express* **2013**, *21* (17), 20090 https://doi.org/10.1364/OE.21.020090.

(63) Wang, Z.; Fan, M.; Wu, H.; Li, Y.; Li, Y.; Zhang, L.; Rao, Y. Cascaded Random Distributed-Feedback Raman Fiber Laser Assisted by Fresnel Reflection. *Opt. Express* **2015**, *23* (21), 28076 https://doi.org/10.1364/OE.23.028076.

(64) Babin, S. A.; El-Taher, A. E.; Harper, P.; Podivilov, E. V.; Turitsyn, S. K. Tunable Random Fiber Laser. *Phys. Rev. A - At. Mol. Opt. Phys.* **2011**, *84* (2), 1–4 https://doi.org/10.1103/PHYSREVA.84.021805.

(65) Turitsyn, S. K.; Babin, S. A.; Churkin, D. V. D. V.; Vatnik, I. D.; Nikulin, M.; Podivilov, E. V.; El-Taher, A. E.; Harper, P.; Churkin, D. V. D. V.; Kablukov, S. I.; et al. Random Distributed Feedback Fibre Laser. *Nat. Photonics* **2010**, *542* (2), 133–193 https://doi.org/10.1038/NPHOTON.2010.4.

(66) El-Taher, A. E.; Alcon-Camas, M.; Babin, S. A.; Harper, P.; Ania-Castañón, J. D.; Turitsyn, S. K. Dual-Wavelength, Ultralong Raman Laser with Rayleigh-Scattering Feedback. *Opt. Lett.* **2010**, *35* (7), 1100 https://doi.org/10.1364/OL.35.001100.

(67) Churkin, D. V.; El-Taher, A. E.; Vatnik, I. D.; Ania-Castañón, J. D.; Harper, P.; Podivilov, E. V.; Babin, S. A.; Turitsyn, S. K. Experimental and Theoretical Study of Longitudinal Power Distribution in a Random DFB Fiber Laser. *Opt. Express* **2012**, *20* (10), 11178 https://doi.org/10.1364/OE.20.011178.

(68) Hu, Z.; Miao, B.; Wang, T.; Fu, Q.; Zhang, D.; Ming, H.; Zhang, Q. Disordered

Microstructure Polymer Optical Fiber for Stabilized Coherent Random Fiber Laser. *Opt. Lett.* **2013**, *38* (22), 4644–4647 https://doi.org/10.1364/OL.38.004644.

(69) Hu, Z.; Xia, J.; Liang, Y.; Wen, J.; Miao, E.; Chen, J.; Wu, S.; Qian, X.; Jiang, H.; Xie, K. Tunable Random Polymer Fiber Laser. *Opt. Express* **2017**, *25* (15), 18421 https://doi.org/10.1364/OE.25.018421.

(70) Hu, Z.; Liang, Y.; Qian, X.; Gao, P.; Xie, K.; Jiang, H.; Hijia, Z. H. U.; Iang, Y. U. L.; Ian, X. I. Q.; Ao, P. E. G.; et al. Polarized Random Laser Emission from an Oriented Disorder Polymer Optical Fiber. *Opt. Lett.* **2016**, *41* (11), 2584 https://doi.org/10.1364/OL.41.002584.

(71) Gomes, A. S. L.; Lima, B. C.; Pincheira, P. I. R.; Moura, A. L.; Gagné, M.; Raposo, E. P.; de Araújo, C. B.; Kashyap, R. Glassy Behavior in a One-Dimensional Continuous-Wave Erbium-Doped Random Fiber Laser. *Phys. Rev. A* **2016**, *94* (1), 011801 https://doi.org/10.1103/PHYSREVA.94.011801.

(72) Lima, B. C.; Gomes, A. S. L.; Pincheira, P. I. R.; Moura, A. L.; Gagné, M.; Raposo, E. P.; de Araújo, C. B.; Kashyap, R. Observation of Lévy Statistics in One-Dimensional Erbium-Based Random Fiber Laser. *J. Opt. Soc. Am. B* **2017**, *34* (2), 293 https://doi.org/10.1364/JOSAB.34.000293.

(73) Communications, N.; González, I. R. R.; Lima, B. C.; Pincheira, P. I. R.; Brum, A. A.; Macêdo, A. M. S.; Vasconcelos, G. L.; de S. Menezes, L.; Raposo, E. P.; Gomes, A. S. L.; et al. Turbulence Hierarchy in a Random Fibre Laser. *Nat. Commun.* **2017**, *8* (June), 15731 https://doi.org/10.1038/NCOMMS15731.

(74) Hu, Z.; Gao, P.; Xie, K.; Liang, Y.; Jiang, H. Wavelength Control of Random Polymer Fiber Laser Based on Adaptive Disorder. *Opt. Lett.* **2014**, *39* (24), 6911 https://doi.org/10.1364/OL.39.006911.

(75) Hu, Z.; Liang, Y.; Xie, K.; Gao, P.; Zhang, D.; Jiang, H.; Shi, F.; Yin, L.; Gao, J.; Ming, H.; et al. Gold Nanoparticle-Based Plasmonic Random Fiber Laser. *J. Opt.* **2015**, *17* (3), 35001 https://doi.org/10.1088/2040-8978/17/3/035001.

(76) Li, S.; Wang, L.; Zhai, T.; Xu, Z.; Wang, Y.; Wang, J.; Zhang, X. Plasmonic Random Laser on the Fiber Facet. *Opt. Express* **2015**, *23* (18), 23985 https://doi.org/10.1364/OE.23.023985.

(77) Hu, Z.; Liang, Y.; Gao, P.; Jiang, H.; Chen, J.; Jiang, S.; Xie, K. Random Lasing from Dye Doped Polymer Optical Fiber Containing Gold Nanoparticles. *J. Opt.* **2015**, *17* (12), 125403 https://doi.org/10.1088/2040-8978/17/12/125403.

(78) Zhou, G.; Pun, C.-F. J.; Tam, H.; Wong, A. C. L.; Lu, C.; Wai, P. K. A. Single-Mode Perfluorinated Polymer Optical Fibers With Refractive Index of 1.34 for Biomedical Applications. *IEEE Photonics Technol. Lett.* **2010**, *22* (2), 106–108 https://doi.org/10.1109/LPT.2009.2036377.

(79) Zhao, X.; Wu, Z.; Ning, S.; Liang, S.; Wang, D.; Hou, X. Random Lasing from Granular Surface of Waveguide with Blends of PS and PMMA. *Opt. Express* **2011**, *19* (17), 16126 https://doi.org/10.1364/OE.19.016126.

(80) Cao, H. Lasing in Random Media. *Waves in Random Media* **2003**, *13* (3), R1–R39 https://doi.org/10.1088/0959-7174/13/3/201.

(81) Uppu, R.; Tiwari, A. K.; Mujumdar, S. Identification of Statistical Regimes and Crossovers in Coherent Random Laser Emission. *Opt. Lett.* **2012**, *37* (4), 662–664 https://doi.org/10.1364/OL.37.000662.

(82) Tommasi, F.; Ignesti, E.; Lepri, S.; Cavalieri, S. Robustness of Replica Symmetry Breaking Phenomenology in Random Laser. *Sci. Rep.* **2016**, *6* (August), 37113 https://doi.org/10.1038/SREP37113.

(83) Redding, B.; Cerjan, A.; Huang, X.; Lee, M. L.; Stone, A. D.; Choma, M. A.; Cao, H. Low Spatial Coherence Electrically Pumped Semiconductor Laser for Speckle-Free Full-Field Imaging. *Proc. Natl. Acad. Sci. U. S. A.* **2015**, *112* (5), 1304–1309 https://doi.org/10.1073/PNAS.1419672112.

(84) Uppu, R.; Mujumdar, S. Statistical Fluctuations of Coherent and Incoherent Intensity in Random Lasers with Nonresonant Feedback. *Opt. Lett.* **2010**, *35* (17), 2831–2833 https://doi.org/10.1364/OL.35.002831.

(85) Cao, H.; Jiang, X.; Ling, Y.; Xu, J. Y.; Soukoulis, C. M. Mode Repulsion and Mode Coupling in Random Lasers. *Phys. Rev. B* **2003**, *67* (16), 161101 https://doi.org/10.1103/PHYSREVB.67.161101.

(86) van der Molen, K. L.; Mosk, A. P.; Lagendijk, A.; Systems, C. P. Intrinsic Intensity Fluctuations in Random Lasers. *Phys. Rev. A* **2006**, *74* (5), 053808 https://doi.org/10.1103/PHYSREVA.74.053808.

(87) Ignesti, E.; Tommasi, F.; Fini, L.; Lepri, S.; Radhalakshmi, V.; Wiersma, D.; Cavalieri, S. Experimental and Theoretical Investigation of Statistical Regimes in Random Laser Emission. *Phys. Rev. A* **2013**, *88* (3), 033820

https://doi.org/10.1103/PHYSREVA.88.033820.

(88) Tulek, A.; Polson, R. C.; Vardeny, Z. V. Naturally Occurring Resonators in Random Lasing of π-Conjugated Polymer Films. *Nat. Phys.* **2010**, *6* (4), 303–310 https://doi.org/10.1038/NPHYS1509.

(89) Polson, R. C.; Raikh, M. E.; Valy Vardeny, Z. Universality in Unintentional Laser Resonators in π-Conjugated Polymer Films. *Comptes Rendus Phys.* **2002**, *3* (4), 509–521 https://doi.org/10.1016/S1631-0705(02)01336-1.

(90) Chen, Y.; Herrnsdorf, J.; Guilhabert, B.; Zhang, Y.; Watson, I. M.; Gu, E.; Laurand, N.; Dawson, M. D. Colloidal Quantum Dot Random Laser. *Opt. Express* **2011**, *19* (4), 2996–3003 https://doi.org/10.1364/OE.19.002996.

(91) Wang, Z.; Meng, X.; Choi, S. H.; Knitter, S.; Kim, Y. L.; Cao, H.; Shalaev, V. M.; Boltasseva, A. Controlling Random Lasing with Three-Dimensional Plasmonic Nanorod Metamaterials. *Nano Lett.* **2016**, *16* (4), 2471–2477 https://doi.org/10.1021/ACS.NANOLETT.6B00034.

(92) Vanneste, C.; Sebbah, P. Complexity of Two-Dimensional Quasimodes at the Transition from Weak Scattering to Anderson Localization. *Phys. Rev. A* **2009**, *79* (4), 041802 https://doi.org/10.1103/PHYSREVA.79.041802.

(93) Cao, H.; Xu, J. Y.; Zhang, D. Z.; Chang, S.-H.; Ho, S. T.; Seelig, E. W.; Liu, X.; Chang, R. P. H. Spatial Confinement of Laser Light in Active Random Media. *Phys. Rev. Lett.* **2000**, *84* (24), 5584–5587 https://doi.org/10.1103/PHYSREVLETT.84.5584.

(94) Bachelard, N.; Gaikwad, P.; Backov, R.; Sebbah, P.; Vallée, R. A. L. Disorder

as a Playground for the Coexistence of Optical Nonlinear Effects: Competition between Random Lasing and Stimulated Raman Scattering in Complex Porous Materials. *ACS Photonics* **2014**, *1* (11), 1206–1211 https://doi.org/10.1021/PH500280M.

(95) Berger, G.; Kempe, M.; Genack, a. Dynamics of Stimulated Emission from Random Media. *Phys. Rev. E* **1997**, *56* (5), 6118–6122 https://doi.org/10.1103/PHYSREVE.56.6118.

(96) Lepri, S.; Cavalieri, S.; Oppo, G.; Wiersma, D. S. Statistical Regimes of Random Laser Fluctuations. *Phys. Rev. A* **2007**, *75* (6), 063820 https://doi.org/10.1103/PHYSREVA.75.063820.

(97) Mujumdar, S.; Türck, V.; Torre, R.; Wiersma, D. S. Chaotic Behavior of a Random Laser with Static Disorder. *Phys. Rev. A - At. Mol. Opt. Phys.* **2007**, *76* (3), 1–6 https://doi.org/10.1103/PHYSREVA.76.033807.

(98) Mujumdar, S.; Ricci, M.; Torre, R.; Wiersma, D. S. Amplified Extended Modes in Random Lasers. *Phys. Rev. Lett.* **2004**, *93* (5), 1–4 https://doi.org/10.1103/PHYSREVLETT.93.053903.

(99) Tommasi, F.; Ignesti, E.; Fini, L.; Cavalieri, S. Controlling Directionality and the Statistical Regime of the Random Laser Emission. *Phys. Rev. A - At. Mol. Opt. Phys.* **2015**, *91* (3), 1–7 https://doi.org/10.1103/PHYSREVA.91.033820.

(100) Wiersma, D. S. Laser Physics: Random Lasers Explained? *Nat. Photonics* **2009**, *3* (5), 246–248 https://doi.org/10.1038/NPHOTON.2009.53.

(101) Psaltis, D.; Quake, S. R.; Yang, C. Developing Optofluidic Technology

through the Fusion of Microfluidics and Optics. *Nature* **2006**, *442* (7101), 381–386 https://doi.org/10.1038/NATURE05060.

(102) Fan, X.; White, I. M. Optofluidic Microsystems for Chemical and Biological Analysis. *Nat. Photonics* **2011**, *5* (10), 591–597 https://doi.org/10.1038/NPHOTON.2011.206.

(103) Erickson, D.; Mandal, S.; Yang, A. H. J.; Cordovez, B. Nanobiosensors: Optofluidic, Electrical and Mechanical Approaches to Biomolecular Detection at the Nanoscale. *Microfluid. Nanofluidics* **2008**, *4* (1–2), 33–52 https://doi.org/10.1007/S10404-007-0198-8.

(104) Minzioni, P.; Osellame, R.; Sada, C.; Zhao, S.; Omenetto, F. G.; Gylfason, K. B.; Haraldsson, T.; Zhang, Y.; Ozcan, A.; Wax, A.; et al. Roadmap for Optofluidics. *J. Opt.* **2017**, *19* (9), 093003 https://doi.org/10.1088/2040-8986/AA783B.

(105) Reynolds, T.; Riesen, N.; Meldrum, A.; Fan, X.; Hall, J. M. M.; Monro, T. M.; François, A. Fluorescent and Lasing Whispering Gallery Mode Microresonators for Sensing Applications. *Laser Photon. Rev.* **2017**, *11* (2), 1600265 https://doi.org/10.1002/LPOR.201600265.

(106) Huang, N.-T.; Zhang, H.; Chung, M.-T.; Seo, J. H.; Kurabayashi, K. Recent Advancements in Optofluidics-Based Single-Cell Analysis: Optical on-Chip Cellular Manipulation, Treatment, and Property Detection. *Lab Chip* **2014**, *14* (7), 1230–1245 https://doi.org/10.1039/C3LC51211H.

(107) Fan, X.; Yun, S.-H. The Potential of Optofluidic Biolasers. *Nat. Methods* **2014**,

11 (2), 141–147 https://doi.org/10.1038/NMETH.2805.

(108) Chen, Y.-C.; Chen, Q.; Fan, X. Lasing in Blood. *Optica* **2016**, *3* (8), 809 https://doi.org/10.1364/OPTICA.3.000809.

(109) Chen, Y.-C.; Chen, Q.; Fan, X. Optofluidic Chlorophyll Lasers. *Lab Chip* **2016**, *16* (12), 2228–2235 https://doi.org/10.1039/C6LC00512H.

(110) Sun, Y.; Shopova, S. I.; Wu, C.-S.; Arnold, S.; Fan, X. Bioinspired Optofluidic FRET Lasers via DNA Scaffolds. *Proc. Natl. Acad. Sci.* **2010**, *107* (37), 16039–16042 https://doi.org/10.1073/PNAS.1003581107.

(111) Gather, M. C.; Yun, S. H. Single-Cell Biological Lasers. *Nat. Photonics* **2011**, *5* (7), 406–410 https://doi.org/10.1038/NPHOTON.2011.99.

(112) Yang, Y.; Liu, A. Q.; Lei, L.; Chin, L. K.; Ohl, C. D.; Wang, Q. J.; Yoon, H. S. A Tunable 3D Optofluidic Waveguide Dye Laser via Two Centrifugal Dean Flow Streams. *Lab Chip* **2011**, *11* (18), 3182 https://doi.org/10.1039/C1LC20435A.

(113) Balslev, S.; Kristensen, A. Microfluidic Single-Mode Laser Using High-Order Bragg Grating and Antiguiding Segments. *Opt. Express* **2005**, *13* (1), 344 https://doi.org/10.1364/OPEX.13.000344.

(114) Vannahme, C.; Smith, C. L. C.; Brøkner Christiansen, M.; Kristensen, A. Emission Wavelength of Multilayer Distributed Feedback Dye Lasers. *Appl. Phys. Lett.* **2012**, *101* (15), 151123 https://doi.org/10.1063/1.4759131.

(115) Shivakiran Bhaktha, B. N.; Bachelard, N.; Noblin, X.; Sebbah, P. Optofluidic Random Laser. *Appl. Phys. Lett.* **2012**, *101* (15), 1–5

https://doi.org/10.1063/1.4757872.

(116) Viola, I.; Ghofraniha, N.; Zacheo, A.; Arima, V.; Conti, C.; Gigli, G. Random Laser Emission from a Paper-Based Device. *J. Mater. Chem. C* **2013**, *1* (48), 8128 https://doi.org/10.1039/C3TC31860E.

(117) Polson, R. C.; Vardeny, Z. V. Organic Random Lasers in the Weak-Scattering Regime. *Phys. Rev. B - Condens. Matter Mater. Phys.* **2005**, *71* (4), 37–41 https://doi.org/10.1103/PHYSREVB.71.045205.

(118) Song, Q.; Xiao, S.; Xu, Z.; Liu, J.; Sun, X.; Drachev, V.; Shalaev, V. M.; Akkus, O.; Kim, Y. L. Random Lasing in Bone Tissue. *Opt. Lett.* **2010**, *35* (9), 1425–1427 https://doi.org/10.1364/OL.35.001425.

(119) Wang, C.-S.; Chang, T.-Y.; Lin, T.-Y.; Chen, Y.-F. Biologically Inspired Flexible Quasi-Single-Mode Random Laser: An Integration of Pieris Canidia Butterfly Wing and Semiconductors. *Sci. Rep.* **2014**, *4* (1), 6736 https://doi.org/10.1038/SREP06736.

(120) Dominguez, C. T.; Lacroute, Y.; Chaumont, D.; Sacilotti, M.; de Araújo, C. B.; Gomes, A. S. L. Microchip Random Laser Based on a Disordered TiO2-Nanomembranes Arrangement. *Opt. Express* **2012**, *20* (16), 17380–17385 https://doi.org/10.1364/OE.20.017380.

(121) Wang, Y.; Ta, V. D.; Gao, Y.; He, T. C.; Chen, R.; Mutlugun, E.; Demir, H. V.; Sun, H. D. Stimulated Emission and Lasing from CdSe/CdS/ZnS Core-Multi-Shell Quantum Dots by Simultaneous Three-Photon Absorption. *Adv. Mater.* **2014**, *26* (18), 2954–2961 https://doi.org/10.1002/ADMA.201305125.

(122) Li, X.; Wang, Y.; Sun, H.; Zeng, H. Amino-Mediated Anchoring Perovskite Quantum Dots for Stable and Low-Threshold Random Lasing. *Adv. Mater.* **2017**, *29* (36), 1701185 https://doi.org/10.1002/ADMA.201701185.

(123) Liang, X. J.; Liu, A. Q.; Lim, C. S.; Ayi, T. C.; Yap, P. H. Determining Refractive Index of Single Living Cell Using an Integrated Microchip. *Sensors Actuators A Phys.* **2007**, *133* (2), 349–354 https://doi.org/10.1016/J.SNA.2006.06.045.

(124) Meng, X.; Fujita, K.; Murai, S.; Konishi, J.; Mano, M.; Tanaka, K. Random Lasing in Ballistic and Diffusive Regimes for Macroporous Silica-Based Systems with Tunable Scattering Strength. *Opt. Express* **2010**, *18* (12), 12153 https://doi.org/10.1364/OE.18.012153.

(125) El-Dardiry, R. G. S.; Mooiweer, R.; Lagendijk, A. Experimental Phase Diagram for Random Laser Spectra. *New J. Phys.* **2012**, *14* (11), 113031 https://doi.org/10.1088/1367-2630/14/11/113031.

(126) Wu, X. H.; Yamilov, A.; Noh, H.; Cao, H.; Seelig, E. W.; Chang, R. P. H. Random Lasing in Closely Packed Resonant Scatterers. *J. Opt. Soc. Am. B* **2004**, *21* (1), 159 https://doi.org/10.1364/JOSAB.21.000159.

(127) Hsiung, F.; McCollum, T.; Hefner, E.; Rubio, T. Comparison of Count Reproducibility, Accuracy, and Time to Results between a Hemocytometer and TC20™ Automated Cell Counter. *Bio-Rad Tech Note Bull.* **2013**, *6003*.

(128) Watanabe, E.; Hoshiba, T.; Javidi, B. High-Precision Microscopic Phase Imaging without Phase Unwrapping for Cancer Cell Identification. *Opt. Lett.*

2013, *38* (8), 1319 https://doi.org/10.1364/OL.38.001319.

(129) Merrill, J. W.; Cao, H.; Dufresne, E. R. Fluctuations and Correlations of Emission from Random Lasers. *Phys. Rev. A - At. Mol. Opt. Phys.* **2016**, *93* (2), 1–5 https://doi.org/10.1103/PHYSREVA.93.021801.

(130) Wu, X.; Fang, W.; Yamilov, A.; Chabanov, A. A.; Asatryan, A. A.; Botten, L. C.; Cao, H. Random Lasing in Weakly Scattering Systems. *Phys. Rev. A - At. Mol. Opt. Phys.* **2006**, *74* (5), 1–11 https://doi.org/10.1103/PHYSREVA.74.053812.

(131) Dice, G. D.; Mujumdar, S.; Elezzabi, A. Y. Plasmonically Enhanced Diffusive and Subdiffusive Metal Nanoparticle-Dye Random Laser. *Appl. Phys. Lett.* **2005**, *86* (13), 1–3 https://doi.org/10.1063/1.1894590.

(132) Meng, X.; Fujita, K.; Murai, S.; Matoba, T.; Tanaka, K. Plasmonically Controlled Lasing Resonance with Metallic−Dielectric Core−Shell Nanoparticles. *Nano Lett.* **2011**, *11* (3), 1374–1378 https://doi.org/10.1021/NL200030H.

(133) Veltri, A.; Infusino, M.; Ferjani, S.; De Luca, A.; Strangi, G. Blue-Shifted Random-Laser-Mode Selection in Gain-Assisted Anisotropic Complex Fluids. *Phys. Rev. E - Stat. Nonlinear, Soft Matter Phys.* **2011**, *83* (4), 1–6 https://doi.org/10.1103/PHYSREVE.83.041711.

(134) Wu, Y.; Ren, Y.; Chen, A.; Chen, Z.; Liang, Y.; Li, J. J.; Lou, G.; Zhu, H.; Gui, X.; Wang, S.; et al. One-Dimension Random Laser Based on Artificial High-Index Contrast Scatterers. *Nanoscale* **2017**, *9* (21), 6959–6964

https://doi.org/10.1039/C7NR00261K.

(135) Mani, S. A.; Guo, W.; Liao, M.-J.; Eaton, E. N.; Ayyanan, A.; Zhou, A. Y.; Brooks, M.; Reinhard, F.; Zhang, C. C.; Shipitsin, M.; et al. The Epithelial-Mesenchymal Transition Generates Cells with Properties of Stem Cells. *Cell* **2008**, *133* (4), 704–715 https://doi.org/10.1016/J.CELL.2008.03.027.

(136) Consoli, A.; López, C. Lasing Optical Cavities Based on Macroscopic Scattering Elements. *Sci. Rep.* **2017**, *7* (1), 40141 https://doi.org/10.1038/SREP40141.

(137) Consoli, A.; Mariano da Silva, D.; Wetter, N. U.; López, C. Large Area Resonant Feedback Random Lasers Based on Dye-Doped Biopolymer Films. *Opt. Express* **2015**, *23* (23), 29954 https://doi.org/10.1364/OE.23.029954.

(138) Sharma, D.; Ramachandran, H.; Kumar, N. Lévy Statistics of Emission from a Novel Random Amplifying Medium: An Optical Realization of the Arrhenius Cascade. *Opt. Lett.* **2006**, *31* (12), 1806–1808 https://doi.org/10.1364/OL.31.001806.

(139) Lin, X.; Wan, N.; Weng, L.; Zhou, Y. Light Scattering from Normal and Cervical Cancer Cells. *Appl. Opt.* **2017**, *56* (12), 3608 https://doi.org/10.1364/AO.56.003608.

(140) Bereiter-Hahn, J.; Fox, C. H.; Thorell, B. Quantitative Reflection Contrast Microscopy of Living Cells. *J. Cell Biol.* **1979**, *82* (3), 767–779 https://doi.org/10.1083/JCB.82.3.767.

(141) He, J.; Chan, W.-K.; Cheng, X.; Tse, M.-L.; Lu, C.; Wai, P.-K.; Savovic, S.;

Tam, H.-Y. Experimental and Theoretical Investigation of the Polymer Optical Fiber Random Laser with Resonant Feedback. *Adv. Opt. Mater.* **2018**, 1701187 https://doi.org/10.1002/ADOM.201701187.

(142) Cristofanilli, M.; Budd, G. T.; Ellis, M. J.; Stopeck, A.; Matera, J.; Miller, M. C.; Reuben, J. M.; Doyle, G. V.; Allard, W. J.; Terstappen, L. W. M. M.; et al. Circulating Tumor Cells, Disease Progression, and Survival in Metastatic Breast Cancer. *N. Engl. J. Med.* **2004**, *351* (8), 781–791 https://doi.org/10.1056/NEJMOA040766.

(143) Stott, S. L.; Hsu, C.-H.; Tsukrov, D. I.; Yu, M.; Miyamoto, D. T.; Waltman, B. A.; Rothenberg, S. M.; Shah, A. M.; Smas, M. E.; Korir, G. K.; et al. Isolation of Circulating Tumor Cells Using a Microvortex-Generating Herringbone-Chip. *Proc. Natl. Acad. Sci.* **2010**, *107* (43), 18392–18397 https://doi.org/10.1073/PNAS.1012539107.

(144) Liu, P. Y.; Chin, L. K.; Ser, W.; Chen, H. F.; Hsieh, C.-M.; Lee, C.-H.; Sung, K.-B.; Ayi, T. C.; Yap, P. H.; Liedberg, B. Cell Refractive Index for Cell Biology and Disease Diagnosis: Past, Present and Future. *Lab Chip* **2016**, *16* (4), 634–644.

(145) Ketene, A. N.; Schmelz, E. M.; Roberts, P. C.; Agah, M. The Effects of Cancer Progression on the Viscoelasticity of Ovarian Cell Cytoskeleton Structures. *Nanomedicine Nanotechnology, Biol. Med.* **2012**, *8* (1), 93–102.

(146) Abdi, H.; Williams, L. J. Principal Component Analysis. *Wiley Interdiscip. Rev. Comput. Stat.* **2010**, *2* (4), 433–459 https://doi.org/10.1002/WICS.101.

(147) Chelnokov, E. V.; Bityurin, N.; Ozerov, I.; Marine, W. Two-Photon Pumped Random Laser in Nanocrystalline ZnO. *Appl. Phys. Lett.* **2006**, *89* (17), 171119 https://doi.org/10.1063/1.2370879.

(148) Zhang, F.; Zhong, H.; Chen, C.; Wu, X.; Hu, X.; Huang, H.; Han, J.; Zou, B.; Dong, Y. Brightly Luminescent and Color-Tunable Colloidal CH 3 NH 3 PbX 3 (X = Br, I, Cl) Quantum Dots: Potential Alternatives for Display Technology. *ACS Nano* **2015**, *9* (4), 4533–4542 https://doi.org/10.1021/ACSNANO.5B01154.

(149) Yang, D.; Xie, C.; Sun, J.; Zhu, H.; Xu, X.; You, P.; Lau, S. P.; Yan, F.; Yu, S. F. Amplified Spontaneous Emission from Organic-Inorganic Hybrid Lead Iodide Perovskite Single Crystals under Direct Multiphoton Excitation. *Adv. Opt. Mater.* **2016**, *4* (7), 1053–1059 https://doi.org/10.1002/ADOM.201600047.

(150) Wang, Y.; Li, X.; Song, J.; Xiao, L.; Zeng, H.; Sun, H. All-Inorganic Colloidal Perovskite Quantum Dots: A New Class of Lasing Materials with Favorable Characteristics. *Adv. Mater.* **2015**, *27* (44), 7101–7108 https://doi.org/10.1002/ADMA.201503573.

(151) Gu, Z.; Wang, K.; Sun, W.; Li, J.; Liu, S.; Song, Q.; Xiao, S. Two-Photon Pumped CH 3 NH 3 PbBr 3 Perovskite Microwire Lasers. *Adv. Opt. Mater.* **2016**, *4* (3), 472–479 https://doi.org/10.1002/ADOM.201500597.

(152) Shamsi, J.; Urban, A. S.; Imran, M.; De Trizio, L.; Manna, L. Metal Halide Perovskite Nanocrystals: Synthesis, Post-Synthesis Modifications, and Their

Optical Properties. *Chem. Rev.* **2019**, *119* (5), 3296–3348 https://doi.org/10.1021/ACS.CHEMREV.8B00644.

(153) Wang, Y.; Li, X.; Zhao, X.; Xiao, L.; Zeng, H.; Sun, H. Nonlinear Absorption and Low-Threshold Multiphoton Pumped Stimulated Emission from All-Inorganic Perovskite Nanocrystals. *Nano Lett.* **2016**, *16* (1), 448–453 https://doi.org/10.1021/ACS.NANOLETT.5B04110.

(154) Xu, Y.; Chen, Q.; Zhang, C.; Wang, R.; Wu, H.; Zhang, X.; Xing, G.; Yu, W. W.; Wang, X.; Zhang, Y.; et al. Two-Photon-Pumped Perovskite Semiconductor Nanocrystal Lasers. *J. Am. Chem. Soc.* **2016**, *138* (11), 3761–3768 https://doi.org/10.1021/JACS.5B12662.

(155) Dhanker, R.; Brigeman, A. N.; Larsen, A. V.; Stewart, R. J.; Asbury, J. B.; Giebink, N. C. Random Lasing in Organo-Lead Halide Perovskite Microcrystal Networks. *Appl. Phys. Lett.* **2014**, *105* (15), 10–15 https://doi.org/10.1063/1.4898703.

(156) Yuan, S.; Chen, D.; Li, X.; Zhong, J.; Xu, X. In Situ Crystallization Synthesis of CsPbBr3 Perovskite Quantum Dot-Embedded Glasses with Improved Stability for Solid-State Lighting and Random Upconverted Lasing. *ACS Appl. Mater. Interfaces* **2018**, *10* (22), 18918–18926 https://doi.org/10.1021/ACSAMI.8B05155.

(157) Popov, O.; Zilbershtein, A.; Davidov, D. Random Lasing from Dye-Gold Nanoparticles in Polymer Films: Enhanced Gain at the Surface-Plasmon-Resonance Wavelength. *Appl. Phys. Lett.* **2006**, *89* (19), 2004–2007

https://doi.org/10.1063/1.2364857.

(158) Kang, F.; He, J.; Sun, T.; Bao, Z. Y.; Wang, F.; Lei, D. Y. Plasmonic Dual-Enhancement and Precise Color Tuning of Gold Nanorod@SiO 2 Coupled Core-Shell-Shell Upconversion Nanocrystals. *Adv. Funct. Mater.* **2017**, *27* (36), 1701842 https://doi.org/10.1002/ADFM.201701842.

(159) Koolyk, M.; Amgar, D.; Aharon, S.; Etgar, L. Kinetics of Cesium Lead Halide Perovskite Nanoparticle Growth; Focusing and de-Focusing of Size Distribution. *Nanoscale* **2016**, *8* (12), 6403–6409 https://doi.org/10.1039/C5NR09127F.

(160) Akkerman, Q. A.; D'Innocenzo, V.; Accornero, S.; Scarpellini, A.; Petrozza, A.; Prato, M.; Manna, L. Tuning the Optical Properties of Cesium Lead Halide Perovskite Nanocrystals by Anion Exchange Reactions. *J. Am. Chem. Soc.* **2015**, *137* (32), 10276–10281 https://doi.org/10.1021/JACS.5B05602.

(161) Ming, T.; Zhao, L.; Yang, Z.; Chen, H.; Sun, L.; Wang, J.; Yan, C. Strong Polarization Dependence of Plasmon-Enhanced Fluorescence on Single Gold Nanorods. *Nano Lett.* **2009**, *9* (11), 3896–3903 https://doi.org/10.1021/NL902095Q.

(162) Lu, W.-G.; Chen, C.; Han, D.; Yao, L.; Han, J.; Zhong, H.; Wang, Y. Nonlinear Optical Properties of Colloidal CH 3 NH 3 PbBr 3 and CsPbBr 3 Quantum Dots: A Comparison Study Using Z-Scan Technique. *Adv. Opt. Mater.* **2016**, *4* (11), 1732–1737 https://doi.org/10.1002/ADOM.201600322.

(163) Wang, Y.; Yang, X.; He, T. C.; Gao, Y.; Demir, H. V.; Sun, X. W.; Sun, H. D.

Near Resonant and Nonresonant Third-Order Optical Nonlinearities of Colloidal InP/ZnS Quantum Dots. *Appl. Phys. Lett.* **2013**, *102* (2), 021917 https://doi.org/10.1063/1.4776702.

(164) Jin, Q.; Wu, W.; Zheng, Z.; Yan, Y.; Liu, W.; Li, A.; Yang, Y.; Su, W. The Third-Order Optical Nonlinearity and Upconversion Luminescence of CdTe Quantum Dots under Femtosecond Laser Excitation. *J. Nanoparticle Res.* **2009**, *11* (3), 665–670 https://doi.org/10.1007/S11051-008-9416-X.

(165) Yao, Y.-C.; Yang, Z.-P.; Hwang, J.-M.; Su, H.-C.; Haung, J.-Y.; Lin, T.-N.; Shen, J.-L.; Lee, M.-H.; Tsai, M.-T.; Lee, Y.-J. Coherent and Polarized Random Laser Emissions from Colloidal CdSe/ZnS Quantum Dots Plasmonically Coupled to Ellipsoidal Ag Nanoparticles. *Adv. Opt. Mater.* **2016**, *5* (3), 1600746 https://doi.org/10.1002/ADOM.201600746.

(166) Morris, S. M.; Ford, A. D.; Pivnenko, M. N.; Coles, H. J. Electronic Control of Nonresonant Random Lasing from a Dye-Doped Smectic A* Liquid Crystal Scattering Device. *Appl. Phys. Lett.* **2005**, *86* (14), 141103 https://doi.org/10.1063/1.1885169.

(167) Bruhn, B.; Valenta, J.; Sangghaleh, F.; Linnros, J. Blinking Statistics of Silicon Quantum Dots. *Nano Lett.* **2011**, *11* (12), 5574–5580 https://doi.org/10.1021/NL203618H.

(168) Yu, H.; Ren, K.; Wu, Q.; Wang, J.; Lin, J.; Wang, Z.; Xu, J.; Oulton, R. F.; Qu, S.; Jin, P. Organic–Inorganic Perovskite Plasmonic Nanowire Lasers with a Low Threshold and a Good Thermal Stability. *Nanoscale* **2016**, *8* (47), 19536–

19540 https://doi.org/10.1039/C6NR06891J.

(169) Oulton, R. F.; Sorger, V. J.; Zentgraf, T.; Ma, R.-M.; Gladden, C.; Dai, L.; Bartal, G.; Zhang, X. Plasmon Lasers at Deep Subwavelength Scale. *Nature* **2009**, *461* (7264), 629–632 https://doi.org/10.1038/NATURE08364.

(170) Eaton, S. W.; Lai, M.; Gibson, N. A.; Wong, A. B.; Dou, L.; Ma, J.; Wang, L.-W.; Leone, S. R.; Yang, P. Lasing in Robust Cesium Lead Halide Perovskite Nanowires. *Proc. Natl. Acad. Sci.* **2016**, *113* (8), 1993–1998 https://doi.org/10.1073/PNAS.1600789113.

(171) Schwefel, H. G. L.; Tureci, H. E. A Chaotic Approach Clears up Imaging. *Science (80-.).* **2015**, *348* (6231), 189–190 https://doi.org/10.1126/SCIENCE.AAA7409.

(172) Mooradian, A.; Jaeger, T.; Stokseth, P. *Tunable Lasers and Applications*; Mooradian, A., Jaeger, T., Stokseth, P., Eds.; Springer Series in Optical Sciences; Springer Berlin Heidelberg: Berlin, Heidelberg, 1976; Vol. 3 https://doi.org/10.1007/978-3-540-37996-6.

(173) HE, J.; Zheng, W.; Chen, X.; Lei, D. Plasmon-Modulated Polarized Upconversion Emissions from Single Gold Nanorod-Nanophosphors Hybrid Nanostructures. In *International Photonics and OptoElectronics*; OSA: Washington, D.C., 2015; p JW3A.40 https://doi.org/10.1364/OEDI.2015.JW3A.40.

(174) Chen, Q.; Liu, H.; Lee, W.; Sun, Y.; Zhu, D.; Pei, H.; Fan, C.; Fan, X. Self-Assembled DNA Tetrahedral Optofluidic Lasers with Precise and Tunable

Gain Control. *Lab Chip* **2013**, *13* (17), 3351 https://doi.org/10.1039/C3LC50629K.

(175) Wang, M.; Bangalore Rajeeva, B.; Scarabelli, L.; Perillo, E. P.; Dunn, A. K.; Liz-Marzán, L. M.; Zheng, Y. Molecular-Fluorescence Enhancement via Blue-Shifted Plasmon-Induced Resonance Energy Transfer. *J. Phys. Chem. C* **2016**, *120* (27), 14820–14827 https://doi.org/10.1021/ACS.JPCC.6B04205.

(176) Galisteo-López, J. F.; Ibisate, M.; López, C. FRET-Tuned Resonant Random Lasing. *J. Phys. Chem. C* **2014**, *118* (18), 9665–9669 https://doi.org/10.1021/JP501101A.

(177) Chen, Q.; Zhang, X.; Sun, Y.; Ritt, M.; Sivaramakrishnan, S.; Fan, X. Highly Sensitive Fluorescent Protein FRET Detection Using Optofluidic Lasers. *Lab Chip* **2013**, *13* (14), 2679 https://doi.org/10.1039/C3LC50207D.

(178) Vohra, V.; Devaux, A.; Dieu, L.-Q.; Scavia, G.; Catellani, M.; Calzaferri, G.; Botta, C. Energy Transfer in Fluorescent Nanofibers Embedding Dye-Loaded Zeolite L Crystals. *Adv. Mater.* **2009**, *21* (10–11), 1146–1150 https://doi.org/10.1002/ADMA.200801693.

(179) Kuo, C.-C.; Wang, C.-T.; Chen, W.-C. Highly-Aligned Electrospun Luminescent Nanofibers Prepared from Polyfluorene/PMMA Blends: Fabrication, Morphology, Photophysical Properties and Sensory Applications. *Macromol. Mater. Eng.* **2008**, *293* (12), 999–1008 https://doi.org/10.1002/MAME.200800224.

(180) Wang, X.; Drew, C.; Lee, S.-H.; Senecal, K. J.; Kumar, J.; Samuelson, L. A.

Electrospun Nanofibrous Membranes for Highly Sensitive Optical Sensors. *Nano Lett.* **2002**, *2* (11), 1273–1275 https://doi.org/10.1021/NL020216U.

(181) Jun, Y.; Kang, E.; Chae, S.; Lee, S.-H. Microfluidic Spinning of Micro- and Nano-Scale Fibers for Tissue Engineering. *Lab Chip* **2014**, *14* (13), 2145–2160 https://doi.org/10.1039/C3LC51414E.

(182) Agarwal, S.; Wendorff, J. H.; Greiner, A. Progress in the Field of Electrospinning for Tissue Engineering Applications. *Adv. Mater.* **2009**, *21* (32–33), 3343–3351 https://doi.org/10.1002/ADMA.200803092.

(183) Sznitko, L.; Romano, L.; Wawrzynczyk, D.; Cyprych, K.; Mysliwiec, J.; Pisignano, D. Stacked Electrospun Polymer Nanofiber Heterostructures with Tailored Stimulated Emission. *RSC Adv.* **2018**, *8* (43), 24175–24181 https://doi.org/10.1039/C8RA03640C.

(184) Vohra, V.; Calzaferri, G.; Destri, S.; Pasini, M.; Porzio, W.; Botta, C. Toward White Light Emission through Efficient Two-Step Energy Transfer in Hybrid Nanofibers. *ACS Nano* **2010**, *4* (3), 1409–1416 https://doi.org/10.1021/NN9017922.

(185) van Hemmen, J. L. Spin-Glass Models of a Neural Network. *Phys. Rev. A* **1986**, *34* (4), 3435–3445 https://doi.org/10.1103/PHYSREVA.34.3435.

(186) Duan, L.-M.; Demler, E.; Lukin, M. D. Controlling Spin Exchange Interactions of Ultracold Atoms in Optical Lattices. *Phys. Rev. Lett.* **2003**, *91* (9), 090402 https://doi.org/10.1103/PHYSREVLETT.91.090402.

(187) Angelani, L.; Conti, C.; Ruocco, G.; Zamponi, F. Glassy Behavior of Light.

Phys. Rev. Lett. **2006**, *96* (6), 065702 https://doi.org/10.1103/PHYSREVLETT.96.065702.

(188) Angelani, L.; Conti, C.; Ruocco, G.; Zamponi, F. Glassy Behavior of Light in Random Lasers. *Phys. Rev. B - Condens. Matter Mater. Phys.* **2006**, *74* (10), 1–16 https://doi.org/10.1103/PHYSREVB.74.104207.

(189) Ghofraniha, N.; Viola, I.; Di Maria, F.; Barbarella, G.; Gigli, G.; Leuzzi, L.; Conti, C. Experimental Evidence of Replica Symmetry Breaking in Random Lasers. *Nat. Commun.* **2015**, *6* (February), 6058 https://doi.org/10.1038/NCOMMS7058.

(190) Antenucci, F.; Crisanti, A.; Leuzzi, L. Complex Spherical 2+4 Spin Glass: A Model for Nonlinear Optics in Random Media. *Phys. Rev. A - At. Mol. Opt. Phys.* **2015**, *91* (5), 1–24 https://doi.org/10.1103/PHYSREVA.91.053816.

(191) Lima, B. C.; Gomes, A. S. L.; Pincheira, P. I. R.; Moura, A. L.; Gagné, M.; Raposo, E. P.; de Araújo, C. B.; Kashyap, R.; Ima, B. I. C. L.; Omes, A. N. S. L. G.; et al. Observation of Lévy Statistics in One-Dimensional Erbium-Based Random Fiber Laser. *J. Opt. Soc. Am. B* **2017**, *34* (2), 293 https://doi.org/10.1364/JOSAB.34.000293.

(192) Pincheira, P. I. R.; Silva, A. F.; Fewo, S. I.; Carreño, S. J. M.; Moura, A. L.; Raposo, E. P.; Gomes, A. S. L.; de Araújo, C. B. Observation of Photonic Paramagnetic to Spin-Glass Transition in a Specially Designed TiO_2 Particle-Based Dye-Colloidal Random Laser. *Opt. Lett.* **2016**, *41* (15), 3459 https://doi.org/10.1364/OL.41.003459.

(193) Krämmer, S.; Vannahme, C.; Smith, C. L. C.; Grossmann, T.; Jenne, M.; Schierle, S.; Jørgensen, L.; Chronakis, I. S.; Kristensen, A.; Kalt, H. Random-Cavity Lasing from Electrospun Polymer Fiber Networks. *Adv. Mater.* **2014**, *26* (48), 8096–8100 https://doi.org/10.1002/ADMA.201402995.

(194) Antenucci, F.; Conti, C.; Crisanti, A.; Leuzzi, L. General Phase Diagram of Multimodal Ordered and Disordered Lasers in Closed and Open Cavities. *Phys. Rev. Lett.* **2015**, *114* (4), 043901 https://doi.org/10.1103/PHYSREVLETT.114.043901.

(195) *Principles of Fluorescence Spectroscopy*; Lakowicz, J. R., Ed.; Springer US: Boston, MA, 2006 https://doi.org/10.1007/978-0-387-46312-4.

(196) Hokr, B. H.; Bixler, J. N.; Cone, M. T.; Mason, J. D.; Beier, H. T.; Noojin, G. D.; Petrov, G. I.; Golovan, L. a; Thomas, R. J.; Rockwell, B. a; et al. Bright Emission from a Random Raman Laser. *Nat. Commun.* **2014**, *5*, 4356 https://doi.org/10.1038/NCOMMS5356.

(197) Uppu, R.; Mujumdar, S. Dependence of the Gaussian-Lévy Transition on the Disorder Strength in Random Lasers. *Phys. Rev. A* **2013**, *87* (1), 013822 https://doi.org/10.1103/PHYSREVA.87.013822.

(198) He, J.; Zheng, W.; Ligmajer, F.; Chan, C.-F. F.; Bao, Z.; Wong, K.-L. L.; Chen, X.; Hao, J.; Dai, J.; Yu, S.-F. F.; et al. Plasmonic Enhancement and Polarization Dependence of Nonlinear Upconversion Emissions from Single Gold Nanorod@SiO2@CaF2:Yb3+, Er3+hybrid Core-Shell-Satellite Nanostructures. *Light Sci. Appl.* **2017**, *6* (5), e16217-11

https://doi.org/10.1038/LSA.2016.217.

(199) Li, D.; Jiang, M.; Cueff, S.; Dodson, C. M.; Karaveli, S.; Zia, R. Quantifying and Controlling the Magnetic Dipole Contribution to 1.5 Mm Light Emission in Erbium-Doped Yttrium Oxide. *Phys. Rev. B* **2014**, *89* (16), 161409 https://doi.org/10.1103/PHYSREVB.89.161409.

(200) Antenucci, F.; Crisanti, A.; Leuzzi, L. The Glassy Random Laser: Replica Symmetry Breaking in the Intensity Fluctuations of Emission Spectra. *Sci. Rep.* **2015**, *5*, 1–11 https://doi.org/10.1038/SREP16792.

(201) Wang, B.; Wang, L.; Guo, N.; Zhao, Z.; Yu, C.; Lu, C. Deep Neural Networks Assisted BOTDA for Simultaneous Temperature and Strain Measurement with Enhanced Accuracy. *Opt. Express* **2019**, *27* (3), 2530 https://doi.org/10.1364/OE.27.002530.

(202) Woodward, R. I.; Kelleher, E. J. R. Towards “Smart Lasers”: Self-Optimisation of an Ultrafast Pulse Source Using a Genetic Algorithm. *Sci. Rep.* **2016**, *6* (July), 1–9 https://doi.org/10.1038/SREP37616.

(203) Yao, K.; Unni, R.; Zheng, Y. Intelligent Nanophotonics: Merging Photonics and Artificial Intelligence at the Nanoscale. *Nanophotonics* **2019**, *8* (3), 339–366 https://doi.org/10.1515/NANOPH-2018-0183.

(204) Närhi, M.; Salmela, L.; Toivonen, J.; Billet, C.; Dudley, J. M.; Genty, G. Machine Learning Analysis of Extreme Events in Optical Fibre Modulation Instability. *Nat. Commun.* **2018**, *9* (1), 1–11 https://doi.org/10.1038/S41467-018-07355-Y.

(205) Zahavy, T.; Dikopoltsev, A.; Moss, D.; Haham, G. I.; Cohen, O.; Mannor, S.; Segev, M. Deep Learning Reconstruction of Ultrashort Pulses. *Optica* **2018**, *5* (5), 666 https://doi.org/10.1364/OPTICA.5.000666.

(206) Shen, Y.; Harris, N. C.; Skirlo, S.; Prabhu, M.; Baehr-Jones, T.; Hochberg, M.; Sun, X.; Zhao, S.; Larochelle, H.; Englund, D.; et al. Deep Learning with Coherent Nanophotonic Circuits. *Nat. Photonics* **2017**, *11* (7), 441–446 https://doi.org/10.1038/NPHOTON.2017.93.

(207) Lin, X.; Rivenson, Y.; Yardimci, N. T.; Veli, M.; Luo, Y.; Jarrahi, M.; Ozcan, A. All-Optical Machine Learning Using Diffractive Deep Neural Networks. *Science (80-.).* **2018**, *361* (6406), 1004–1008 https://doi.org/10.1126/SCIENCE.AAT8084.